IN VIVO IMAGING AND MODELING OF ARTERY BLOOD PRESSURE WAVE AND INTERACTION WITH LIGHT IN TIME DOMAIN

By

Jiahong Jin

December, 2021

Director of Dissertation: Dr. Xin-Hua Hu

Major Department: Physics

ABSTRACT

Artery blood flow driven by pressure wave is essential for human life. The long-term research goal is to establish a foundation for future translation of the imaging photoplethysmography (iPPG) method into applications such as extraction of vital health biomarkers. For this dissertation research, we focus on development of a robust framework of hardware and data processing tools for rapid acquisition and analysis of *in vivo* iPPG data.

Through this project, we have developed a multispectral imaging system for acquisition of time-sequenced iPPG data *in vivo* from hands of two volunteers with 12 wavelength bands ranging from 445 to 940 nm at a frame rate up to 250 Hz. A fluid dynamic model of blood flow and pressure wave was employed to quantify the effects of the artery wall deformation with different Young's modulus, artery radius and other boundary conditions on flow rate and pressure. A voxel-based Monte Carlo (MC) simulation model has been established for quantitative analysis of the iPPG data based on the radiative transfer theory. The measured waveforms of iPPG signals at multiple locations in palmar artery have been compared to the waveforms of blood pressure waves calculated with the coupled model of MC and the fluid dynamic simulations. We have identified the optimal wavelength bands for iPPG illumination to detect palm artery tree and shown that the spatial and temporal distributions of the iPPG signals have strong potentials to monitor heartbeat rate and conditions of artery. The results of this dissertation study provide convincing evidences that iPPG data contain rich information on blood flow and propagation of pressure wave in artery. Consequently, future development of the iPPG method can yield a powerful and non-contact tool to rapidly acquire vital sign data and quantitatively assess cardiovascular conditions.

IN VIVO IMAGING AND MODELING OF ARTERY BLOOD PRESSURE WAVE AND INTERACTION WITH LIGHT IN TIME DOMAIN

A Dissertation

Presented To the Faculty of the Department of Physics

East Carolina University

In Partial Fulfillment of the Requirements for the Degree

Doctor of Philosophy in Biomedical Physics

by

Jiahong Jin

December, 2021

In vivo imaging and modeling of artery blood pressure wave and interaction with light in time domain

By

Jiahong Jin

APPROVED BY:

Director of Dissertation	Xin-Hua Hu, PhD
Committee Member	Johanna L. Hannan, PhD
Committee Member	Nathan E. Hudson, PhD
Committee Member	Jun Q. Lu, PhD
Committee Member	Jason Yao, PhD
Chair of the Department of Physics	Jefferson Shinpaugh, PhD
Dean of the Graduate School	Paul J. Gemperline, PhD

ACKNOWLEDGEMENTS

I would like to thank my advisor, Dr. Xin-Hua Hu for his tireless guidance and help during my research time in ECU. His rigorous attitude and dedicated spirit on the science lead my way forever.

I express my thanks to Dr. Johanna L. Hannan, Dr. Nathan E. Hudson, Dr. Jun Q. Lu, and Dr. Jason Yao as my committee members for their time and providing feedbacks for improvement of my dissertation.

I am very thankful for Physics department for the technical support in imaging system construction. I thank Dr. Kenneth Jacobs, Mr. William Holland, and Mr. Gene Oakley for helps in the development of the iPPG imaging system.

I thank Dr. Cheng Chen for his helps on development of voxel Monte Carlo code and multispectral imaging.

Thank you to my friends in Greenville for bringing happiness to my life.

I would like to thank my family members for their love, support, and encouragement every day. And most gratefully I want to thank my lovely wife and daughter for their company in my toughest time.

TABLE OF CONTENTS

LIST OF TABLES

LIST OF FIGURES

LIST OF SYMBOLS

C	the compliance of distal arteries
$d\omega$	differential solid angle
E	Young's modulus
$\mathbf{f}$	friction force
g	anisotropy factor
h	wall thickness
$\mathbf{I_n}$	input PPG signal
$\mathbf{J}$	voxel index
L	radiance
l_a	total free pathlength
l_c	accumulated free pathlength
l_m	pathlength in a voxel during a scattering
l_s	scattering free pathlength
n	refractive index
$\mathbf{n}$	surface normal
p	fliud pressure
P	probability density function
$\mathbf{P}$	momentum
P_s	systolic pressure at the systolic peak
P_d	diastolic pressure at the first foot

$p(\mathbf{s}\cdot\mathbf{s}')$	scattering phase function
p_{HG}	Henyey-Greenstein function
Q	flow rate
$\mathbf{r}$	position vector
R	the characteristic impedance of each peripheral artery
S	cross-section area
$\mathbf{s}$	unit vector of the light propagation direction
$\mathbf{S}_k$	source vector
t	time
$\mathbf{U}$	fluid velocity, it can also be written as (U_x, U_y, U_z)
V	fluid volume
$\mathbf{w}$	velocity of tube surface
w_n	component of **w** along the surface normal of side wall
x	tube length coordinate
α	momentum-flux correction coefficient
$\boldsymbol{\gamma}_i$	eigenvector
$[\boldsymbol{\varepsilon}]$	strain tensor
ε_e	the external light sources radiance density
$[\boldsymbol{\sigma}]$	stress tensor
μ	viscosity
μ_a	absorption coefficient

μ_s	scattering coefficient
ν	kinetic viscosity
ν_P	Poisson's ratio
θ	polar angle
ϕ	Given's rotation angle
φ	azimuthal angle
ξ	a random number
ρ	mass density
$[\boldsymbol{\tau}]$	shear stress tensor
$\odot$	Hadamard product

LIST OF ABBREVIATIONS

0D	Zero-dimensional
1D	One-dimensional
2D	Two-dimensional
3D	Three-dimensional
AHA	American Heart Association
BC	Boundary condition
BSS	Blind source separation
CUDA	Compute Unified Device Architecture
CV	Control volume
CVD	Cardiovascular disease
CS	Enclosing surface of CV
ECG	Electrocardiogram
EOM	Equation of momentum
FFT	Fast Fourier transform
FNP	First nearest-neighbor pixel
fNP	Fifth nearest-neighbor pixel
FOV	Feild of view
GPU	Graphics of processing unit
HG	Henyey-Greenstein
HR	Heartbeat rate

ICA	Independent component analysis
ICs	independent components
iMC	Individual photon tracking Monte Carlo
iPPG	Imaging PPG
JADE	Joint approximate diagonalization of eigenmatrices
LED	Light-emitting diode
LHS	Left-hand side
MC	Monte Carlo
MFC	Microsoft Foundation Classes
NIR	Near-infrared
OOP	out-of-phase
PCA	Principal component analysis
pICA	Pixelated ICA
POI	Pixel of interest
PPG	Photoplethysmography
PPW	Pressure pulse wave
PTT	Pulse transit time
PWI	Pulse wave index
PWV	Pulse wave velocity
RA	Reference pixel area
RBC	Red blood cell

RHS	Right-hand side
RND	Random number
ROI	Region of interest
RR	Respiration rate
RT	Radiative transfer
SM	Streaming multiprocessors
SNP	Second nearest-neighbor pixel
sNP	Sixth nearest-neighbor pixel
SNR	Signal-to-noise-ratio
SPO_2	Blood oxygen saturation
SVR	Support vector regression
viMC	voxelized iMC

CHAPTER 1 INTRODUCTION

The method of photoplethysmography (PPG) was first explored by Hertzman et al. in the 1930s as a non-invasive technique to acquire the signals of light scattering from skin tissues, which was interpretated as the result of volumetric changes in the vasculature embedded in tissues at detected locations during a cardiac cycle [1]. Over past few decades, the PPG method has attracted strong research attention that led to widely used medical devices for measuring blood oxygen saturation (SPO$_2$), estimation of blood pressure, detecting cardiac output and diagnosis of peripheral vascular diseases [2-6]. However, all PPG devices collect relevant information of one or very limited number of tissue locations and needs to be in contact with the sensed tissues for sufficient signal-to-noise-ratios (SNRs). These methods thus cannot provide spatial distribution of biomarkers extracted from measured data with high resolution. The contact nature of measurement also presents risk of infection. In contrast, an imaging PPG (iPPG) technology provides a non-contact method for acquisition of blood related signals and has the potentials for determination of spatial and temporal distributions in tissue bed for extraction of vital sign data.

There are two basic modes of PPG detection to measure scattered light from tissues: transmission and reflection. For iPPG by a camera sensor without tissue contact, reflection mode is usually applied for data acquisition from highly turbid tissues such as human skin. Due to the complexity of light-tissue interaction, extraction of physiological parameters from iPPG data of low SNRs presents a very challenging task, which requires development of effective imaging system and data processing algorithm by accurate modeling of light transport in tissues containing blood vessels. Any significant modeling effort must account for blood pulsation driven by cardiac activities and light-tissue interaction that modulates the distributions of light intensity reaching the image sensor. Further, numerous causes of light intensity distribution in iPPG data must be carefully considered that include blood volume variation, vessel wall motion and variation of the light absorption and scattering light transport in skin tissues [7-9]. Accurate modeling thus requires development of a set of tools for different aspects of blood flow and light-matter interaction and combine them into an effective one.

This dissertation research project focuses on the *in vivo* acquisition and analysis of iPPG data with a long-term research goal to establish a foundation for extracting vital biomarkers that can be used to improve health monitoring and care of populations at risk. To achieve the goal, we have developed a multispectral imaging system for acquisition of *in vivo* data of time-sequenced image stacks. An 1D model of blood flow and pressure wave was employed to simulate blood flow and pressure under different initial and boundary conditions. A voxel-based Monte Carlo (MC) modeling software was built to determine reflection images from phantoms of palm artery and their temporal variations within the framework of radiative transfer (RT) theory. Important features such as heartbeat rate (HR), temporal and spatial distributions of the heartbeat signals and waveforms were extracted *in vivo* from two volunteers. The results of this dissertation research provide powerful tools and clear evidences for non-contact measurement and extraction of vital health biomarkers beyond the existing pulse oximetry devices and existing iPPG methods.

The innovations of this dissertation study can be summarized below. An experimental iPPG system has been designed and built for imaging light reflected from a hand of volunteer with multiple light-emitting diode (LED) arrays. With this system, we acquired multispectral iPPG image stacks at 12 wavelength bands and imaging frame rates up to 250 Hz and compare the effect of wavelength on extraction of blood pressure wave related parameters. We have also investigated different implementations of the independent component analysis (ICA) algorithm to advance an effective and rapid method for extraction of heartbeat related signals by performing pixel based blind source separation (BSS). The new implementation of the ICA algorithm is termed as pixelated ICA (pICA) algorithm which enabled us to derive a pulse wave index (PWI) map per wavelength band with the same spatial resolution as the raw image data. Finally, a voxel-based MC code is coupled with a fluid dynamic model of blood flow for simulation iPPG process and comparison with the measured data to extract parameters related to cardiac signals and propagation of blood pressure waves.

This dissertation is organized into the following chapters. Chapter 2 provides the background information of measurement of PPG and iPPG signals and light-tissue interaction underly PPG and iPPG. Chapter 3 presents a theoretical framework for fluid dynamic modeling of blood flow and optical modeling of light scattering in tissues with embedded artery tree by RT theory by an individual photon tracking Monte Carlo (iMC) method and pICA method. In Chapter 4 the results of numerical simulation of blood flow dynamic modeling and iMC modeling are provided. Chapter 5 describes the experimental system, iPPG data acquisition and analysis of acquired iPPG image stack data. We discuss in Chapter 6 the significance of this dissertation study and directions for future research.

CHAPTER 2 BACKGROUND

This chapter provides the background information on the physiology of blood flow for this dissertation research and existing methods of data acquisition and analysis related to PPG and iPPG. It consists of three parts including medical implications of iPPG method, the background of PPG and iPPG.

2.1 Medical implications of iPPG method

Cardiovascular diseases (CVDs) including coronary heart disease, heart failure, stroke and hypertension present a great threat to human health and life. The American Heart Association (AHA) reported that the US population prevalence of CVDs in adults of 20 years of age or older was at 48.0% or 121.5 million people in 2016 [10]. Moreover, AHA estimated that 45.1% of the US population would have some form of CVDs by 2035. For the year of 2014, the estimated cost of healthcare related to CVDs was $351.2 billion, and by this tendency, the total costs are expected to reach $1.1 trillion in 2035. As the population ages, the prevalence of CVDs is expected to increase in both males and females. Therefore, research and development of accurate and cost-effective devices on assessing cardiovascular conditions and improved diagnosis of CVDs become a hot field of clinical research today.

Generally, cardiovascular risk factors include bad health behaviors such as smoking, lack of physical activity, poor diet, overweight and negative health indicators such as high level of cholesterol, hypertension, and high blood glucose level. Reports of cardiovascular research suggest that CVDs including coronary artery disease and hypertension, are multifactorial genetic diseases. In 1997, Carter et al. reported that risk factors influencing the development of atherosclerosis associated with the genes encoding fibrinogen and platelet glycoprotein IIB/IIIa receptors [11]. Later, 4 regions of the human genome had been identified that influence systolic blood pressure variation [12, 13]. It becomes clear from the additional research reports that new strategies for monitoring cardiovascular conditions and CVD diagnostic need to be developed.

Existing methods of noninvasive vascular imaging in diagnosis of peripheral arterial disease include computed tomography angiography [14-16], magnetic resonance angiography [17, 18] and conventional angiography [19]. Other modalities have also been developed to evaluate micro perfusion in the lower extremity by taking advantages of light from the ultraviolet to near-infrared spectral regions such as continuous wave doppler [20, 21], ultrasound of flow-mediated dilation [22], endothelial vasodilator function with the endo-PAT [23], and duplex ultrasound imaging [24, 25]. Multispectral and hyperspectral imaging based on different models of tissue optics utilizes spectral data of scattering light signals to obtain spatial maps of blood oxygenation detect different levels of oxygen supply in the lower extremities of patients with and without peripheral arterial diseases [26]. In 2021, Lai et al. evaluated the iPPG system for the assessment of peripheral artery disease and reported that iPPG can detect reduced perfusion levels which correlates well with other measurement systems [27].

A large body of clinical studies has found that in patients with chronic hypertension of higher mean circulatory pressure, cardiac output remains within normal ranges and total intravascular blood volume is normal or low. [28-30]. Research suggests that for these patients arterial stiffness is a major risk factor which is especially severe for large arteries [31, 32]. Arterial stiffness could be measured from pulse wave velocity (PWV) [33]. Modeling of vascular pathophysiology by fluid dynamics of blood flow yield clear evidences that that pulse waves travel faster in stiffer arteries [31, 34]. There is a database of normal values for PWV in human artery based on a large European population of almost 17,000 individuals in different age groups which is shown in Figure 2-1 [35]. Boxes contain 50% of the reported data, bars contain the remainder of “in range” data, and the circles indicate outlies.

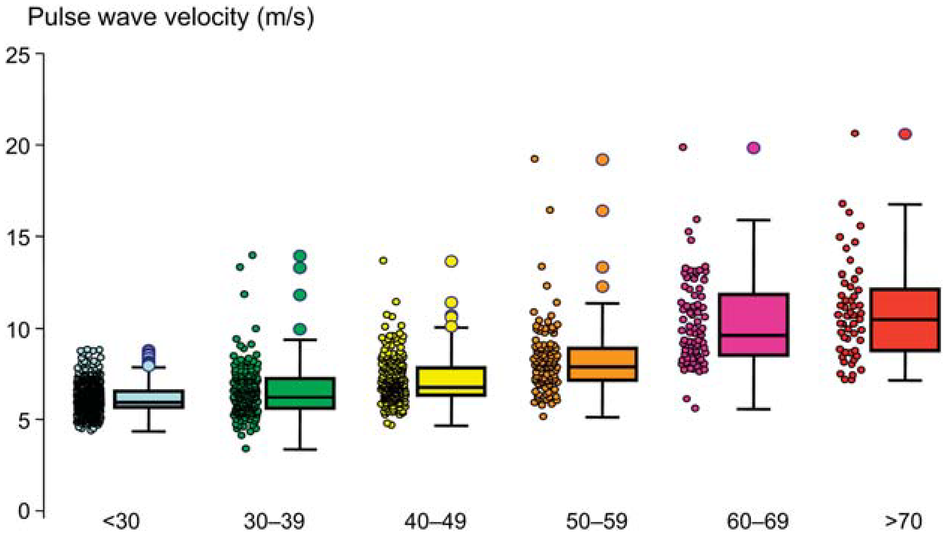

Figure 2-1 Distribution of pulse wave velocity values measured from 1455 normal subjects grouped according to age [35].

2.2 PPG: signal measurement and data processing

2.2.1 PPG signal measurements

PPG technique was reported by Hertzman et al. in the 1930s as a non-invasive optical technique to detect the volumetric changes in the dermal vasculature at selected locations by the time dependence of scattered light intensity during cardiac cycles [1, 36]. In the early stage of PPG research, the time dependence or waveform of the light scattering signals was divided into a pulsatile or AC component and a slowly varying or DC component by separate electronic filters before amplifications for monitoring of vasomotor activity and other blood pulsatile activities. The AC component was usually interpretated as a result of variation of light absorption by the change in the blood volume related to HR. The DC component consists of stationary light background by tissue and the average blood volume in addition to lower frequency components due to respiration, sympathetic nervous system activity and thermoregulation [37]. For contact PPG devices with reflection mode of light detection, the acquired light signals also depend on the stability of light source, wavelength of light source and tightness of contact between the probe and skin. It is generally accepted that the PPG waveform components could provide valuable information about the cardiovascular system as data of vital signs [8]. Over the past few decades, PPG technology has attracted strong research attention that led to medical devices for measuring oxygen saturation, blood pressure, cardiac output and detecting peripheral vascular diseases [2-6]. With the development of photoelectric and semiconductor technology, such as LED, photodiodes and phototransistors, as well as the in-depth research of PPG technique, PPG devices exhibit advantages such as compactness, high reliability, cost effectiveness, and simple-to-use ability. To facilitate daily healthcare monitoring, wearable PPG devices present a significant opportunity as healthcare products for population of all ages. Combining PPG device with, for example, an accelerometer has been used to further reduce motion related noises in acquired PPG signals that allows measurement of HR and SPO_2 during daily activities [38, 39].

Shi et al., introduced a noncontact PPG prototype and demonstrated its feasibility for physiological monitoring in 2009 [40]. It is a reflection setup with one channel infrared LED as illumination light source and a high-speed silicon PIN photodiode which is positioned 5 cm from the tissue surface. Later, a development of the noncontact PPG technology was reported [41]. Usually, non-contact detectors are more sensitive to motion artifacts than traditional contact detectors. Therefore, a remote sensing technology is needed to overcome this barrier. In fact, a resurgence of interest in PPG appears in recent years due to the development of remote sensing and imaging instruments [42-46].

2.2.2 PPG Model and Optical principles

The pulmonary circulation of the cardiovascular system transports the blood from the right ventricle through pulmonary arteries to the lungs to absorb oxygen O_2 molecules and release carbon dioxide molecules CO_2 which then pushes the oxygenated blood back to the left atrium through pulmonary vein. The O_2 and CO_2 molecules are exchanged between the inhaled air and the blood in the alveoli which is the main function unit of the respiratory systems [47]. The contraction of the cardiac muscle produces quasi-periodic blood pressure waves propagating along the artery vascular walls at speeds ranging from 4 m/s to 15 m/s, causing variations in scattered light distribution in the tissue around the arteries [48]. Due to the pressure change and blood flow, the superficial arteries make pulsatile oscillations in their sizes of cross sections which can be observed visually in specific locations such as ulnar and radial artery on wrist. The pulsatile pressure wave propagating in artery causes volume changes which influence the light absorption and scattering and then vary the light scattering signals, which can be measured from the light emerging from the illuminated tissues.

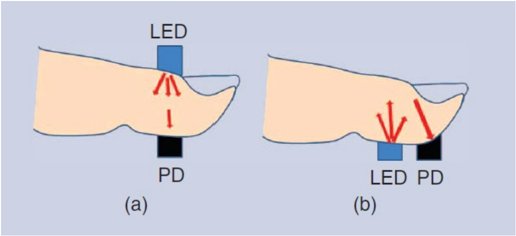

Figure 2-2 Position of LED and photodetector in different PPG modes: (a) transmission mode and (b) reflectance mode [49].

A PPG sensor usually consists of two parts, a light source by LEDs and a light photodetector by photodiodes or other light sensors. There are usually two PPG sensing models, transmission mode and reflectance mode presented in Figure 2-2 which is taken from [49]. The LED illuminates the tissue, and the photodetector senses the reflected or transmitted light intensity which is modulated by volumetric changes in the dermal vasculature. The interaction of light with biological tissue is complex including scattering and absorption, and it depends on the light wavelength and tissue composition. The absorption coefficient μ_a, scattering coefficient μ_s, anisotropy factor g, and refractive index n for skin dermis have been determined by Ma et al. in 2005 [50] and for whole blood by Bosschaart et al. [51]. Since variations in light signal are mainly caused by changes in blood volume and optical properties of the microvascular tissue bed, the ideal wavelengths of PPG detection should be those at which the differences in absorption and scattering parameters between blood and other tissue components. Generally, melanin absorbs more light at short wavelengths near and in the ultraviolet, while water absorbs more at long wavelengths in the region of near-infrared (NIR) and other infrared regions beyond 1300 nm. So, the light source chosen for conventional PPG systems are usually in spectral regions of red or NIR. Comparing the absorption spectra for oxyhemoglobin and deoxyhemoglobin molecules in red blood cells, we can find that green LED has much greater absorptivity for both oxy- and deoxyhemoglobins [52]. Several studies reported that green light illuminators allow higher accuracy in determination of HR than those in traditional NIR region [53, 54].

Light passing though human tissue can be absorbed by skin, bone, venous blood, and arterial blood as shown in Figure 2-3 which is adopted from [39]. The DC component of the PPG signal waveform are usually attributed to light interaction with tissue component not related to heartbeat such as venous blood, bloodless tissues and a part of artery blood. In comparison, the AC component is mainly due to the pulsatile component of artery blood flow that occurs during a cardiac cycle with maximum blood volume occurring in the systolic phase and a minimum blood volume at the diastolic phase. The PPG waveform is thus resulted from the pulsatile artery related to changes in the elastic properties of the blood vessel walls and tissues' optical properties. The pulsation amplitude of a measured PPG signal during each cardiac cycle is suggested to closely relate to the blood flow rate which indicates the state of vasoconstriction [8].

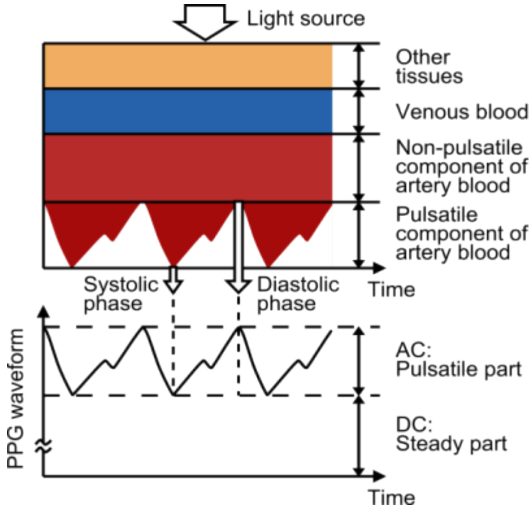

Figure 2-3 Components of the PPG signal waveform compared to variations in light absorption in blood and tissues [39].

Another mechanism which has been studied in its influence on PPG signals is red blood cell (RBC) aggregation [55]. Shvartsman et al. reported that the nature of pulsatile changes of blood transparency could be explained by pulsations of RBC aggregate size using a PPG device. The RBC aggregation effect is limited to relatively thin blood layer which has the thickness comparable with $[\mu_s(1-g)]^{-1}$ as microvasculature of the upper dermis.

2.3 Imaging PPG

iPPG is a camera-based passive contactless method to extract different physiological signals from different parts of the human body. The study of iPPG was first reported in 1996 by Blazek et al. [56]. Afterwards, Wu et al. presented a CCD-based iPPG system in 2000 for investigation of blood perfusion in skin [57]. Since then, the research related to iPPG techniques grows rapidly. The basic concept of iPPG is to illuminate a target with a light source and then measure the reflected light using an imaging sensor. Compared to point sensors, imaging sensors have additional capabilities of reducing motion artifact and selection of multiple regions of interest (ROIs). These advantages make iPPG methods robust and versatile devices for contactless acquisition of PPG signals. By imaging of artery blood with high spatiotemporal resolutions, the iPPG methods have the potential to provide an alternative functional imaging solution for clinical scenarios.

2.3.1 iPPG system instrumentation

Generally, in an iPPG system, the variation of reflected light signal acquired by an image sensor is very weak for the component related to heartbeat. For instance, observations of measured intensity in conventional contact PPG sensors indicate that the AC component accounts for only a small proportion of the total intensity at approximately 1% of the DC component [58]. Obviously, the signal of heartbeat is much weaker in iPPG data. Therefore, the PPG sensors or imaging sensors should have high sensitivity over the spectral range of illuminated light and the readout speeds and data transmission speed need to be coupled appropriately for different applications. For multi-wavelength light sources, it is better to individually control the exposure time for different channels of a camera sensing light of different wavelengths. There are three common combinations of camera and light-source, depending on the application scenarios. First, for pulse oximetry monitoring, a camera sensor needs to detect light reflected from the relatively deep microvascular tissue bed. Two light bands with different peak wavelengths around 660 nm (red) and 940 nm (NIR) are selected with a high-definition camera to build an iPPG system. If one only needs to monitor HR or respiration rate

(RR), a single red or NIR light source is enough. Second, several attempts have been made to obtain iPPG signals using simple commercial digital cameras with normal ambient light as the light source. This type of systems usually was built to analyze the acquired data by the relation between images in the three-color channels of red, green, and blue. Verkruysse et at. found that the strongest signal related to heartbeat was in the green channel for larger values of μ_a for oxyhemoglobin in the green channel than the red one. With the development of smart cellphone technology, the third kind of iPPG system has been designed with cellphone image sensors and usually uses a white LED as the light source [59].

2.3.2 Tissue color-based method

The iPPG principle relies on the intensity variations of light reflected from skin as a result of cardiorespiratory activity. Vital signs are extracted from iPPG data or image pixel values of brightness by exploiting variations in the optical properties of skin tissue and artery from a video or image stack. Figure 2-4 (adapted from [60]) illustrate a typical iPPG system and tissue phantom consists of an illumination source, a target as human skin and a video camera. The light source can be a special light source or ambient light as describe in the previous section. When light illuminates skin, a small part of light is reflected specular on the surface, and other part enters the skin. Once in tissue, the light propagates in different directions after sequence of scattering events and ends up either being absorbed or scattered out of tissue as diffuse reflection or transmission. For iPPG, the diffusely reflected light reaching an image sensor carries information on the interactions of light with different tissue components. The information carried by the signals depends on the wavelength of the light and the structure of tissue. Since fluctuation of illumination light intensity and motion of imaged subject, among others, present strong noise background, powerful algorithm must be developed to separate the changes in the reflected light intensity related to the blood volume changes in in artery during cardiac cycle and the tissue deformation with the blood vessel from the strong noise background.

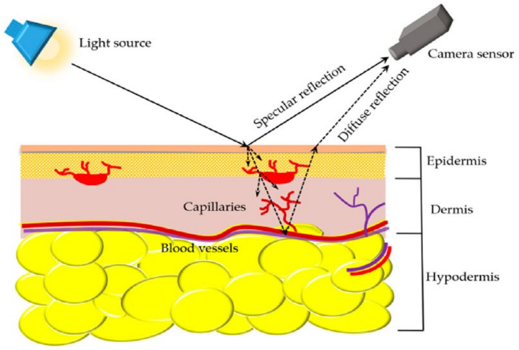

Figure 2-4 Schematic of iPPG configuration for imaging skin tissues with blood vessels in the dermal and hypodermal layers [60].

2.3.3 Data processing

After acquisition of the raw iPPG data, a series of image processing and signal processing techniques are required to extract HR related parameters from the image stack. The existing framework of iPPG data processing usually includes ROI detection, raw signal extraction, denoising, and vita signal extraction. The ROI such as the face, forehead, chest, and palm within the frames are detected either manually or automatically. Once the image data are recorded, one can manually select the ROI, which usually has a fixed frame size for the whole image sequence. In this scenario, subjects are required to keep motionless during the recording. To overcome the limitations of the previous technique, Pho et al. used an automatic OpenCV face detection algorithm based on the Viola and Jones (VJ) method [61]. It is a novel method to measure HR using a webcam for three subjects at a time. To improve the accuracy of auto tracking, Feng et al. introduced an ROI selection method integrating the VJ method and a speeded-up robust features method [62]. In 2015, Wang et al. used “tracking-by-detection” with kernels method to detect face on light, intermediate, and dark skin types [63]. They further introduced a classification method about skin/nonskin pixel which is based upon one-class support vector machine technique. They used this method to concatenate the same class of skin pixels from whole image as a ROI, then extracted perfusion signals from the ROI.

Once the ROI and channel have been selected, a spatial ROI averaging approach is usually introduced to improve the signal-to-noise-ratio (SNR) of vital signs, although it compromises the spatial resolution the same time. Generally, a color camera has three channels (RGB). The imaging sensor is sensitive, and the light-tissue interaction varies across the wavelength spectrum. The iPPG signals have different relative strengths in the RBG channels, and the green channel has strongest pulse amplitude. There are several methods about the color channel selection which could be summarized as using green channel only, three channel combined with ICA technique [64] and defining three independent linear combinations of the RGB channels using principal component analysis (PCA) method [65]. ICA and PCA are both BSS techniques. Lewandoska et al. reported that PCA is faster than ICA in terms of computation time and it can be a good alternative if only HR is extracted [65].

The raw signal may contain unwanted noise due to factors such as skin tone, illumination changes, subject or camera movement. To remove the noise, various signal processing techniques may be applied including moving average filter, low/bandpass pass filtering, adaptive bandpass filtering, signal decomposition, and wavelet denoising. Essentially, the heart rate of a healthy subject falls within the frequency range of [0.65, 4.00Hz].

Finally, vital signs are extracted by using frequency analysis or peak detection. For frequency analysis, the fast Fourier transform (FFT), Discrete cosine transform, and short-time Fourier transform are usually applied to calculate the corresponding frequency of vital signs. Hsu et al.

introduced a support vector regression (SVR) technique for learning-based framework for HR monitoring by leveraging the mid-level iPPG based features [66]. The frequency-domain features included the spectrum amplitude for the spatially averaged R, G, B channels, the spectrum amplitude for the ICA processed independent components, and the spectrum amplitude for the chrominance-based pulse signals. When using a peak detection algorithm, the number of peaks is calculated during the processing period. McDuff et al. introduced a time-domain peak detection method which based upon local maximum detection in a moving window and found that the distance between the diastolic peak and the systolic peak decreases with age [67].

2.3.4 Progress of iPPG application

As the traditional PPG technique, iPPG could be used to measure HR, RR, and SPO_2. Thanks to the fast-advancing imaging technology, iPPG holds a significant advantage in offering a tool of high spatial resolution to measure light distributions from multiple regions of interest (ROIs) simultaneously. Thus, it allows the derivation and mapping of parameters of clinical relevance such as blood perfusion [68-70]. In 2011, Anchan et al. reported some preliminary results of pulse wave velocity (PWV) determination based on comparison of blood pressure waveform acquired with a cell phone camera against waveforms measured with a portable Doppler ultrasound probe [71]. Shao et al. later presented a method of pulse transit time (PTT) estimation through measuring the time delay between the pulse signals from the mouth area and the palm area [72]. Also in 2014 Huang et al. developed a blood pressure transport model to monitor systolic and diastolic blood pressures (P_s and P_d) extracted from acquired iPPG data [73]. In addition, iPPG has some other importance and interesting applications. Several groups of researchers proposed the use of iPPG method to assess conditions of skin tissues [74-76]. Other researchers used iPPG systems to monitor and characterize wound healing and burn excision

[77]. It should be noted that increase of spatial or temporal resolutions of the characteristic features extracted from iPPG data can significantly improve the robustness of iPPG devices for applications including detecting health and alertness of automobile drivers [78, 79], enhancement of neonatal care [80] and anesthesia procedures [81, 82], stress detection [83], and monitoring of patients during magnetic resonance imaging [84].

CHAPTER 3 THEORETICAL FRAMEWORK

In this chapter we present a theoretical foundation for modeling fluid dynamics of blood and light scattering that give rise to iPPG data, which includes a one-dimension (1D) fluid dynamic model, a MC model based on the radiative transfer theory, and iPPG data processing based on ICA algorithm. This allows us to extract parameters related to the propagation of pressure wave in blood vessels from the light scattering signals embedded in the measured image data. Furthermore, the modeling results enable investigation of blood flow rate and pressure variations during a cardiac cycle and associated morphologic changes in human tissues.

3.1 Fluid dynamic modeling of blood

Blood pressure wave is generated by the ventricular contraction and propagates downstream from the aorta to peripheral artery [85, 86]. The blood pressure wave exhibits complex waveforms consisting of cardiac cycles according to the heartbeat rate. The contour of blood pressure waveforms can be divided into a systolic phase, a diastolic phase and a dicrotic notch as show in Figure 3-1 adapted from [87]. The profile of different components depends on the physical properties of the individual cardiovascular system such as the contraction of ventricle, the shape of artery tree, elasticity of artery wall and the microcirculation at the end of vessel system. Shavartsman et al. interpretated their experimental data showing that PPG signals could be described as light scattering caused by time-variant aggregation of red blood cells (RBCs) [55]. But the large body of later research results demonstrated that the RBC aggregation is dominant only in small arteries such as arterioles and capillaries [88]. For large vessels like radial or ulnar arteries in the hand region concerned in this study, the blood fluid can be approximated as a homogenous Newtonian fluid for fluid dynamic modeling [89-92]. In this section we present the theoretical framework of fluid dynamics for modeling of blood flow in deformable arteries. The basic parameters of a compliant tube discussed here can be described in the form of tubular structure with an axial coordinate *x*, and cross-section area S presented in Figure 3-2 taken from [91], where ρ is the blood density, μ blood viscosity, φ wall viscosity, E wall Young's modulus, h wall thickness, S luminal area, U the cross section average velocity, Q the blood flow rate, p the blood pressure.

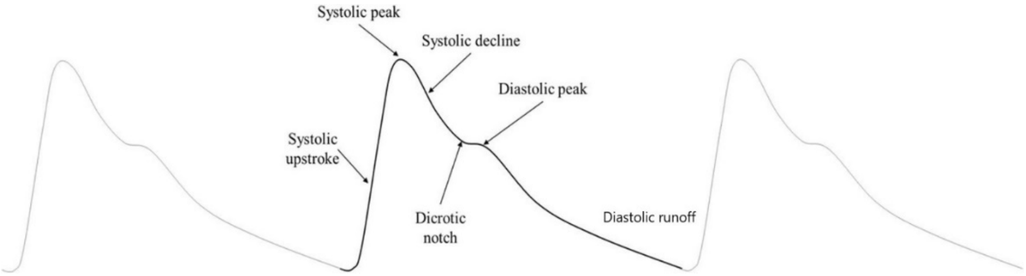

87].

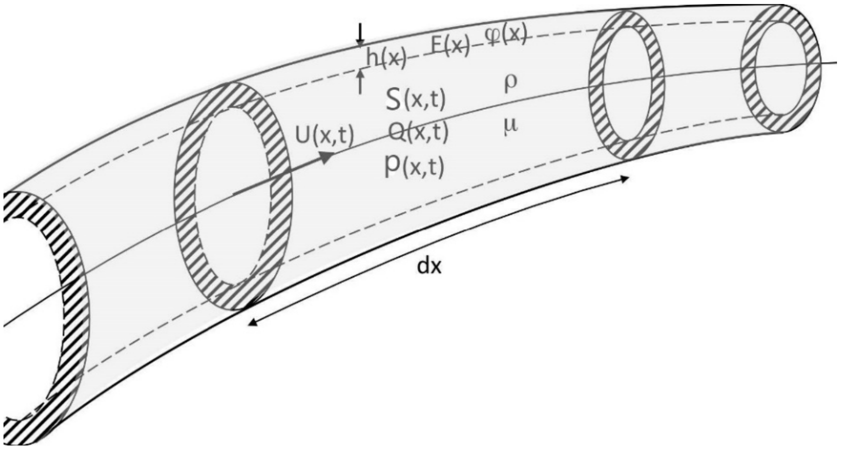

91].

3.1.1 Reynold transport equation

Fluid dynamics is in the category of classical physics which assumes the "space" as an inertial reference frame at rest to describe a position of interest by $\mathbf{r}= (x\mathbf{x}, y\mathbf{y}, z\mathbf{z})$. The Reynold transport equation provides a general framework for deriving various equations of balance for concerned variables. Let’s denote B as a property of the concerned fluid such as mass, energy, momentum, angular momentum etc. and β=dB/dm as the intensive variable of B or amount of B per unit of fluid mass. For example, we can write dB = βdm = βρdV with V as the volume of interest of fluid. One must note that B and β vanish outside V.

We first define control volume (CV) as the concerned fluid volume at time t or CV=V(t). As time t advances to t+Δt, the present fluid volume V(t+Δt) gains an amount of fluid relative to V(t) in the direction of fluid velocity **U**=Δ**r**/Δt as an outflow relative to V(t) and loses an amount of fluid against **U** as an inflow or “left behind” flow relative to V(t). So does B(t+Δt) relative to B(t) and we can quantify these changes by respective surface flux integrals. Sum of these terms in the limit of Δt→ 0 yields the total rate of changes of B for a moving fluid

$$\frac{dB}{dt} = \frac{d}{dt}\int_{CV} \beta\rho dV + \int_{S_{out}} \beta\rho\mathbf{U}\cdot\mathbf{n}dS_{out} - \int_{S_{in}} \beta\rho\mathbf{U}\cdot\mathbf{n}'dS_{in} = \frac{d}{dt}\int_{CV} \beta\rho dV + \oint_{CS} \beta\rho\mathbf{U}\cdot\mathbf{n}dS, \qquad (3\text{-}1)$$

where CS is the enclosing surface of CV, S_{out} and S_{in} is the area of CS with outflow or inflow, **n** and **n**’ is outward and inward surface normal of the CS, ρ is the mass density of fluid. Eq. (*3-1*) yields the integral form of Reynolds transport theorem, which can be turned into following differential form by taking CV as a stationary volume using the Eulerian description

$$\frac{dB}{dt} = \frac{\partial\beta\rho}{\partial t} + \nabla\cdot\beta\rho\mathbf{U}, \qquad (3\text{-}2)$$

based on the divergence theorem and the argument of arbitrary choices of CV.

To properly express terms in the transport equation by cross-sectional averaged quantities for 1D modeling, we replace B by volume integral of β and taken ρ out of the equation by assuming it as a constant [90] to derive the following equation

$$\frac{d}{dt}\int_{CV}\beta dV=\int_{CV}(\frac{\partial\beta}{\partial t})dV+\oint_{CS}\beta\mathbf{W}\cdot\mathbf{n}dS\,. \tag{3-3}$$

For the left-hand side (LHS) of Eq. (*3-3*), one may separate volume integral into cross-sectional and axial integrals to

$$\frac{d}{dt}\int_{CV}\beta dV=\frac{d}{dt}\int_{0}^{x_1}dx\int_{S(x,t)}\beta(\mathbf{r},t)dS=\int_{0}^{x_1}\frac{\partial}{\partial t}\{\langle\beta(x,t)\rangle S(x,t)\}dx\,, \tag{3-4}$$

where x_1 is the tube length, S(x, t) is the luminal area and the cross-sectional average value of β is given by

$$\langle\beta(x,t)\rangle=\frac{1}{S(x,t)}\int_{S(x,t)}\beta(\mathbf{r},t)dS\,. \tag{3-5}$$

For the second term on the right-hand side (RHS) of Eq. (*3-3*), one may define **w** as the velocity of tube surface (or vessel side wall) relative to fluid velocity **U** so that **w** = **W**−**U** and replace **W** by **w** to find

$$\begin{aligned}\oint_{CS}\beta\mathbf{W}\cdot\mathbf{n}dS&=\oint_{CS}\beta\mathbf{w}\cdot\mathbf{n}dS+\oint_{CS}\beta\mathbf{U}\cdot\mathbf{n}dS\\&=\int_{S_w}\beta\mathbf{w}\cdot\mathbf{n}dS+\int_{S_{in}}\beta\mathbf{w}\cdot\mathbf{n}dS+\int_{S_{out}}\beta\mathbf{w}\cdot\mathbf{n}dS+\int_{CV}\nabla\cdot(\beta\mathbf{U})dV\,,\end{aligned} \tag{3-6}$$

where the last term was obtained by the divergence theorem. In our coordinate system x represents the axial coordinate and the surface normal vectors are given by **n**=(0, 0, -1) on S_{in} and **n**=(0, 0, 1) on S_{out}. Consequently, we have

$$\oint_{CS}\beta\mathbf{W}\cdot\mathbf{n}dS=\int_{S_w}\beta w_n dS+\int_{S_{out}}\beta w_x dS-\int_{S_{in}}\beta w_x dS+\int_{CV}(\mathbf{U}\cdot\nabla\beta)dV\,, \tag{3-7}$$

where w_n is the component of **w** along the surface normal of side wall. Since the two end surfaces, with $x=x_0$ and $x=x_1$, of the tube are fixed, so we have $S(x_0, t)=S(x_0)$ and $S(x_1, t)=S(x_1)$ and their velocities of $\mathbf{W}(x_0)$ and $\mathbf{W}(x_1)$ vanish, which means **w**=-**U** at the two end surfaces. Thus, we can write

$$\begin{aligned}\oint_{CS}\beta\mathbf{W}\cdot\mathbf{n}dS &= \int_{S_w}\beta w_n dS - \mathrm{S}_{out}\left\langle\beta U_x(x=\mathrm{x}_1,t)\right\rangle + \mathrm{S}_{\mathrm{in}}\left\langle\beta U_x(x=\mathrm{x}_0,t)\right\rangle + \int_{CV}\nabla\cdot(\beta\mathbf{U})dV,\\ &= \int_{S_w}\beta w_n dS - \int_{x_0}^{x_1}\frac{\partial}{\partial x}\{\mathrm{S}\langle\beta U_x\rangle\}dx + \int_{CV}\nabla\cdot(\beta\mathbf{U})dV\end{aligned} \quad .(3\text{-}8)$$

Applying Eq. (*3-4*) and Eq. (*3-8*), Eq. (*3-3*) becomes

$$\int_{x_0}^{x_1}\{\frac{\partial}{\partial t}(\langle\beta\rangle S) + \frac{\partial}{\partial x}(\mathrm{S}\langle\beta U_x\rangle)\}dx = \int_{CV}\{\frac{\partial\beta}{\partial t} + \nabla\cdot(\beta\mathbf{U})\}dV + \int_{S_w}\beta w_n dS\,. \quad (3\text{-}9)$$

We can further convert the volume and surface integral terms on the RHS of Eq. (*3-9*) into axial ones as

$$\int_{CV}\{\frac{\partial\beta}{\partial t} + \nabla\cdot(\beta\mathbf{U})\}dV + \int_{S_w}\beta w_n dS = \int_{x_0}^{x_1}\{\int_{S(x,t)}\{\frac{\partial\beta}{\partial t} + \nabla\cdot(\beta\mathbf{U})\}dS + \oint_{C(x,t)}\beta w_n dC\}dx \quad (3\text{-}10)$$

where C(x, t) is the circumference of S(x, t). This equation can be used to turn Eq. (*3-9*) into an 1D form of the Reynold transport equation by the requirement of this equation to be true for any value of tube length x_1-x_0

$$\frac{\partial}{\partial t}(S\langle\beta\rangle) + \frac{\partial}{\partial x}(\mathrm{S}\langle\beta U_x\rangle) = \int_{S(x,t)}\{\frac{\partial\beta}{\partial t} + \nabla\cdot(\beta\mathbf{U})\}dS + \oint_{C(x,t)}\beta w_n dC\,. \quad (3\text{-}11)$$

3.1.2 Equation of mass conservation

As the first application of the Reynolds transport equation, we can obtain the following 1D form of mass conservation equation from Eq. (*3-11*)

$$\frac{\partial S(x,t)}{\partial t} + \frac{\partial\{S(x,t)\mathbf{U}(x,t)\}}{\partial x} = \int_{S(x,t)}\nabla\cdot\mathbf{U}dS + \oint_{C(x,t)}w_n dC = \oint_{C(x,t)}w_n dC\,, \quad (3\text{-}12)$$

by setting β = 1and applying ∇·**U** = 0 for incompressible fluid. Define $Q = \int_{S(x,t)} S\mathbf{U}dS$ as volume flux and ψ as volumetric outflow of blood from side wall with -**w** as the velocity of blood relative to wall

$$\psi(x,t) = -\oint_{C(x,t)} w_n dC \cdot \tag{3-13}$$

Then we can determine the differential form of mass conservation for a tube and serves as the first equation of momentum (EOM) for 1D blood flow modeling

$$\frac{\partial S}{\partial t} + \frac{\partial (SU)}{\partial x} + \psi = \frac{\partial S(x,t)}{\partial t} + \frac{\partial Q(x,t)}{\partial x} + \psi(x,t) = 0 \cdot \tag{3-14}$$

3.1.3 Equation of momentum balance

Considering blood as the Newtonian or incompressible and viscous fluid, we can derive the momentum balance equation as the second EOM for 1D blood flow modeling. In this case we have $\nabla \cdot \mathbf{U} = 0$ and set $\beta = U_x(x, t)$ in the Reynold transport equation (*3-11*) which becomes

$$\frac{\partial}{\partial t}(S\langle U_x \rangle) + \frac{\partial}{\partial x}(\mathrm{S}\langle U_x^2 \rangle) = \int_{S(x,t)} (\frac{dU_x}{dt}) dS + \oint_{C(x,t)} U_x w_n dC, \tag{3-15}$$

where $\langle U_x^2(x,t) \rangle = \frac{1}{S(x,t)} \int_{S(x,t)} U_x^2(x,t) dS$. To proceed, we need to find out the integral term with dU_x/dt on RHS of the above equation, which could be obtained by analysis of the forces on a fluid element of volume δV based on the Newton's second law.

As a viscous fluid moves, friction forces arise in the contact surfaces of the element δV with other parts of the fluid. Newton's second law provides the equation of motion as

$$\sum \delta \mathbf{F} = \frac{d}{dt} \delta \mathbf{P} = \rho \delta V \frac{d\mathbf{U}}{dt}, \tag{3-16}$$

where $\mathbf{P} = (p(x), p(y), p(z))$. The total force $\Sigma \delta \mathbf{F}$ on the element δV consists of three forces. The external body force $\mathbf{f}_b \delta V$ with $\mathbf{f}_b$ as body force density is usually given by gravity force per unit volume $\rho \mathbf{g}$. The second one is due to inward fluid pressure p on each of the surfaces. The last force is the results of internal friction of viscous fluid and is denoted as $\mathbf{f}_v \delta V$ with $\mathbf{f}_v$ as the friction force density. Combining these force terms leads to

$$\begin{aligned}\sum \delta \mathbf{F} &= \mathbf{f}_b \delta V + \mathbf{f}_v \delta V - \{\delta y \delta z[p(x+\delta x) - p(x)]\mathbf{x} + \delta x \delta z[p(y+\delta y) - p(y)]\mathbf{y} \\ &\qquad + \delta x \delta y[p(z+\delta z) - p(z)]\mathbf{z}\} \\ &= \mathbf{f}_b \delta V + \mathbf{f}_v \delta V - \delta V \nabla p\end{aligned} \quad . \tag{3-17}$$

Taking the above into Eq. (*3-16*) leads to

$$\rho \frac{d\mathbf{U}}{dt} = \mathbf{f}_b - \nabla p + \mathbf{f}_v \cdot \tag{3-18}$$

The friction forces arising in the contact surfaces of the element δV with other parts of the fluid can be defined by a stress tensor [**σ**] and a viscous shear stress tensor [**τ**] as

$$[\boldsymbol{\sigma}] = \begin{pmatrix} \sigma_{11} & \sigma_{12} & \sigma_{13} \\ \sigma_{21} & \sigma_{22} & \sigma_{23} \\ \sigma_{31} & \sigma_{32} & \sigma_{33} \end{pmatrix} = \begin{pmatrix} -p + \tau_{11} & \tau_{12} & \tau_{13} \\ \tau_{21} & -p + \tau_{22} & \tau_{23} \\ \tau_{31} & \tau_{32} & -p + \tau_{33} \end{pmatrix} . \tag{3-19}$$

The diagonal elements σ_{ii} define the stresses along surface normal $\mathbf{n}_i$ // $\mathbf{x}_i$ and contains two parts of -p by fluid pressure and another of friction while the off-diagonal elements σ_{ij} define shear friction stresses related to tangential surface forces due to relative motion of fluid elements. The tensor [**σ**] is also called Cauchy stress tensor and [**τ**] the deviatoric stress tensor. With the deviatoric stress tensor, the friction force density $\mathbf{f}_v$ can be written in a matrix form as

$$\mathbf{f}_v = \frac{\delta \mathbf{F}_v}{\delta V} = \begin{pmatrix} \frac{\partial}{\partial x} & \frac{\partial}{\partial y} & \frac{\partial}{\partial z} \end{pmatrix} \begin{pmatrix} \tau_{11} & \tau_{12} & \tau_{13} \\ \tau_{21} & \tau_{22} & \tau_{23} \\ \tau_{31} & \tau_{32} & \tau_{33} \end{pmatrix} \equiv \nabla \cdot [\boldsymbol{\tau}] . \tag{3-20}$$

Taking the matrix form of $\mathbf{f}_v$ back to the Eq. (*3-18*) for viscous fluid, we arrive at the equation of linear momentum balance which is also called the Cauchy's equation as follows

$$\rho(\frac{\partial \mathbf{U}}{\partial t} + (\mathbf{U} \cdot \nabla)\mathbf{U}) = \mathbf{f}_b - \nabla p + \nabla \cdot [\boldsymbol{\tau}] , \tag{3-21}$$

where the acceleration vector d **U** /dt in the LHS of Eq. (*3-18*) were separated into two terms.

By volume integrates the Cauchy's Equation as

$$\int_{CV} \frac{d\mathbf{U}}{dt} dV = \int_{CV} \frac{1}{\rho} \{\mathbf{f}_b + \nabla \cdot (-p[I] + [\boldsymbol{\tau}]\} dV \,. \tag{3-22}$$

And setting dV=dSdx, we can obtain the following result with arbitrarily chosen constant tube length

$$\int_{S} \frac{d\mathbf{U}}{dt} dS = \int_{S} \frac{1}{\rho} \{\mathbf{f}_b - \nabla p + \mathbf{f}_v\} dS \,. \tag{3-23}$$

with the friction force $\mathbf{f}_v = \nabla \cdot [\boldsymbol{\tau}]$ defined in Eq. (*3-20*). The *x*-component of the above equation is given by

$$\int_{S} \frac{dU_x}{dt} dS = \frac{S}{\rho} \{\langle f_{bx} \rangle - \frac{\partial \langle p \rangle}{\partial x} + \langle f_{vx} \rangle\} \,. \tag{3-24}$$

Taking Eq. (*3-24*) back to Eq. (*3-15*) yields the 1D form of the equation of momentum balance

$$\frac{\partial}{\partial t}(S\langle U_x \rangle) + \frac{\partial}{\partial x}(\mathrm{S}\langle U_x{}^2 \rangle) = \frac{S}{\rho} \{\langle f_{bx} \rangle - \frac{\partial \langle p \rangle}{\partial x} + \langle f_{vx} \rangle\} + \oint_{C(x,t)} U_x w_n dC \,. \tag{3-25}$$

A shape factor α, also called momentum-flux correction coefficient or Coriolis coefficient, can be defined by

$$\alpha(x,t) \equiv \frac{1}{S\langle U_x \rangle^2} \int_{S(x,t)} U_x{}^2 dS = \frac{\langle U_x{}^2 \rangle}{\langle U_x \rangle^2} \,. \tag{3-26}$$

The value of α depends on the cross-sectional profile of U_x with α=1 for top-hat flow and α=4/3 for parabolic Poiseuille flow as shown in Figure 3-3. Consequently, the shape factor α accounts for the deviation of $< U_x^2>$ from $\mathbf{U}^2$ for cases of $U_x = U_x(\mathbf{r})$.

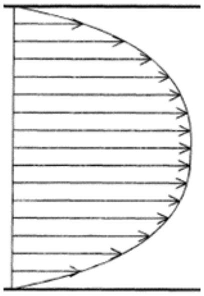

Figure 3-3 The cross-sectional profile of U_x with shape factor α

The shear stress in a fluid causes deformation, which can be quantified by a strain tensor [**ε**] to measure relative size changes or displacement gradient

$$[\boldsymbol{\varepsilon}] = \begin{pmatrix} \frac{\partial \delta x}{\partial x} & \frac{1}{2}(\frac{\partial \delta x}{\partial y} + \frac{\partial \delta y}{\partial x}) & \frac{1}{2}(\frac{\partial \delta x}{\partial z} + \frac{\partial \delta z}{\partial x}) \\ \frac{1}{2}(\frac{\partial \delta y}{\partial x} + \frac{\partial \delta x}{\partial y}) & \frac{\partial \delta y}{\partial y} & \frac{1}{2}(\frac{\partial \delta y}{\partial z} + \frac{\partial \delta z}{\partial y}) \\ \frac{1}{2}(\frac{\partial \delta z}{\partial x} + \frac{\partial \delta x}{\partial z}) & \frac{1}{2}(\frac{\partial \delta z}{\partial y} + \frac{\partial \delta y}{\partial z}) & \frac{\partial \delta z}{\partial z} \end{pmatrix} = [\boldsymbol{\varepsilon}]^T , \tag{3-27}$$

where the diagonal elements of [**ε**] measure the relative changes of sizes along each of three axes and the off-diagonal elements of [**ε**] measure the shear strains. Newtonian fluid is defined under shear stress by a linear relation between the shear stress tensor [**σ**] and strain rate tensor d[**ε**]/dt. This definition is based on the observations of the relation between friction force and flow speed in simple cases of an objects moving in air and water, etc.. The constant coefficient μ between [**σ**] and d[**ε**]/dt for a Newtonian fluid is defined as the fluid viscosity or dynamic viscosity shows below

$$[\boldsymbol{\tau}] = 2\mu \frac{\partial[\boldsymbol{\varepsilon}]}{\partial t} \equiv \mu\{\nabla \mathbf{U} + (\nabla \mathbf{U})^T\} . \tag{3-28}$$

Assume the fluid viscosity μ is constant, the divergence of above equation is

$$\nabla \cdot [\boldsymbol{\tau}] = \mu\{\nabla^2 \mathbf{U} + \nabla(\nabla \cdot \mathbf{U})\} . \tag{3-29}$$

If the fluid is incompressible, the divergence of **U** becomes

$$\nabla \cdot \mathbf{U} = \frac{\partial U_x}{\partial x} + \frac{\partial U_y}{\partial y} + \frac{\partial U_z}{\partial z} = 0\,. \tag{3-30}$$

Then we obtain the divergence of $[\boldsymbol{\tau}]$ as

$$\nabla \cdot [\boldsymbol{\tau}] = \mu \nabla^2 \mathbf{U} = \mu \left(\frac{\partial^2 U_x}{\partial x^2} + \frac{\partial^2 U_x}{\partial y^2} + \frac{\partial^2 U_x}{\partial z^2} \quad \frac{\partial^2 U_y}{\partial x^2} + \frac{\partial^2 U_y}{\partial y^2} + \frac{\partial^2 U_y}{\partial z^2} \quad \frac{\partial^2 U_z}{\partial x^2} + \frac{\partial^2 U_z}{\partial y^2} + \frac{\partial^2 U_z}{\partial z^2} \right).$$

(3-31)

Hence, we can obtain the Navier-Stokes equation from the Cauchy's equation for incompressible Newtonian fluids

$$\rho(\frac{\partial \mathbf{U}}{\partial t} + (\mathbf{U} \cdot \nabla)\mathbf{U}) = \rho \mathbf{g} - \nabla p + \mu \nabla^2 \mathbf{U}\,. \tag{3-32}$$

Substituting the Eq.(*3-31*) to Eq. (*3-20*), we can obtain the cross-sectionally averaged axial component of the friction force as

$$\begin{aligned} \langle f_{vx} \rangle &= \frac{1}{S} \int_S \nabla \cdot [\boldsymbol{\tau}]\big|_x \, dydz = \frac{\mu}{S} \int_S \nabla^2 U_x dS \\ &= \frac{\mu}{S} \int_S \{\nabla_x{}^2 + \nabla_S{}^2\} U_x(S) dS \\ &= \frac{\mu}{S} \int_S \frac{1}{S} \frac{d}{dS} (S \frac{d}{dS} \{2\{1 - (\frac{S}{R})^2\} \langle U_x \rangle\} dS \\ &= -\frac{8\pi\mu}{S} \langle U_x \rangle \approx -\frac{\kappa_R}{S} U_x \end{aligned}, \tag{3-33}$$

where we assumed the Poiseuille paraboloid flow profile [93] is

$$U_x(x, y, z) = U_x(S) = 2\{1 - (\frac{S}{R})^2\} \langle U_x \rangle \tag{3-34}$$

The positive parameter of $\kappa_R \equiv 8\pi\mu > 0$ is defined as the viscous resistance of the flow per unit length of tube [94]. With specified α and κ_R, the momentum balance Eq. (*3-25*) which used as the second EOM of 1D blood flow dynamics becomes

$$\frac{\partial}{\partial t}(SU_x)+\frac{\partial}{\partial x}(\alpha S{U_x}^2)=\frac{S}{\rho}\{\langle f_{bx}\rangle-\frac{\partial\langle p\rangle}{\partial x}\}-\frac{\kappa_R}{\rho}U_x+\oint_{C(x,t)}U_x w_n dC \tag{3-35}$$

for modeling blood as a Newtonian and incompressible fluids.

3.2 The effect of boundary conditions on pressure waveform

Modeling blood dynamics and pressure wave in artery presents a challenging problem due to the complex tree structure and the elastic artery wall. Since the wavelength (~ 1m) of blood pressure wave is much longer than the artery size (~ 1mm) in the transverse cross-section, a long wavelength approximation can be applied to consider blood flow as a quasi-1D motion along the axial direction. At an outlet surface or a junction of artery branches, boundary conditions (BCs) may be further quantified by 0D models of blood flow which parameterize the time dependence of a boundary value of blood pressure or flow rate in analogy to a circuit of lumped elements in response to the propagation of EM waves of long wavelengths [90, 91, 95]. The complexity of fluid dynamic modeling can be much reduced for the cases of laminar flow. A widely used criterion for laminar flow condition is provided by requiring the Reynolds's number Re to be smaller than 2000. The definition of Re is given by

$$\mathrm{Re}=\frac{\rho \mathbf{U} x_{Re}}{\mu}, \tag{3-36}$$

where x_{Re} is a characteristic length or linear dimension of a concerned vessel. In 1D modeling of the blood flow investigated in this study, the blood flow is treated as laminar since the Re values are well below 2000 for radial or ulnar arteries of diameters on the scales of millimeters under normal physiological conditions.

Generally, the body force on blood by gravity affects blood transport modeling in thin-walled vascular structures like veins of significant deformability. For thicker-walled artery considered in our research, body force can be ignored unless in the cases of postural changes. With these assumptions, the 1D model developed in this study enables us to focus on the temporal dependence of blood flow at different positions along the axial direction of artery and replace variables by their cross-sectional averaged values.

3.2.1 Simplification of EOMs of 1D blood vessel model

We first set $\mathbf{f}_{bx}$=0, w_n=0 (no-slip boundary condition) and ψ=0 since blood is assume here as a homogeneous with a constant fluid density ρ, incompressible Newtonian fluid with negligible body force and impermeable vessel wall. In 1D scenario, we denote that $U=U_x$. The mass conservation equation (*3-14*) is simplified as

$$\frac{\partial S}{\partial t}+\frac{\partial (SU)}{\partial x}=0\,. \tag{3-37}$$

The assumption conditions above can be further used to simplify the momentum balance equation (*3-35*) to

$$\frac{\partial U}{\partial t}+(2\alpha-1)U\frac{\partial U}{\partial x}+(\alpha-1)\frac{U^2}{S}\frac{\partial S}{\partial x}+\frac{1}{\rho}\frac{\partial p}{\partial x}+\frac{1}{S\rho}\kappa_R U=0\,, \tag{3-38}$$

where we have replaced < p > by p as cross-sectional averaged pressure.

Finally, we obtain two EOMs for 1D model of blood flow as

$$\begin{aligned}&\frac{\partial S}{\partial t}+\frac{\partial (SU)}{\partial x}=0,\\&\frac{\partial U}{\partial t}+(2\alpha-1)U\frac{\partial U}{\partial x}+(\alpha-1)\frac{U^2}{S}\frac{\partial S}{\partial x}+\frac{1}{\rho}\frac{\partial p}{\partial x}+\frac{1}{S\rho}\kappa_R U=0\end{aligned}\,. \tag{3-39}$$

If we define the flow rate Q=SU, and set top-hat profile α=1 and $\kappa_R=8\pi\mu$, the EOMs become as following

$$\begin{aligned}&\frac{\partial S}{\partial t}+\frac{\partial(Q)}{\partial x}=0,\\&\frac{\partial Q}{\partial t}+\frac{\partial}{\partial t}(\frac{Q^2}{S})=-\frac{S}{\rho}\frac{\partial p}{\partial x}-\frac{8\pi\mu}{\rho S}Q\end{aligned}\quad. \tag{3-40}$$

3.2.2 BCs at artery wall and end surfaces

As blood flow is driven by heartbeat, the blood pressure inside a vessel depends on time and vessel position, and thus modify the size of elastic vessel. The relationship between pressure and vessel size is required to solve problems of blood flow dynamics, which is termed as fluid-structure interaction model. A structure model was proposed for modeling of flood flow dynamics in arteries with a thin, incompressible, homogeneous, isotropic vessel wall. And the elastic membrane deformation mainly happens in the normal direction to the wall surface [96-99]. For circular tubes typical of blood vessels, the constitutive relation governing the fluid-structure interaction [100, 101] is

$$p(S)-p_0=\frac{2\rho\mathbf{V}_0^{\ 2}}{b}\{(\frac{S}{S_0})^{b/2}-1\},\ b=\frac{2\rho\mathbf{V}_0^{\ 2}}{p_0-p_{collapse}}\ , \tag{3-41}$$

where p_0 is external pressure of tissues outside the blood vessel, S_0 and $\mathbf{V}_0$ is respectively the reference cross-section area, velocity at pressure p_0. The parameter $p_{collapse}$ corresponds to, is the pressure when S → 0 [100]. The equation can also be given by the constitutive equation as a nonlinear relation between p and S, which is similar to Eq.(*3-42*) above but simplified with b = 1

$$p(S)-p_{ext}=\beta_0(\sqrt{S}-\sqrt{S_0})\ \ , \tag{3-42}$$

where $\beta_0\equiv\frac{\sqrt{\pi}hE}{S_0(1-\nu_P^{\ 2})}$, E is Young's modulus of wall, h is wall thickness, ν_P is Poisson's ratio which is defined as the ratio of strains in transverse direction and axial directions under an axial stress, the reference area S_0 satisfies $p(S_0)=p_{ext}$. It is assumed that $\nu_P=0.5$ for blood vessel wall.

This equation is also named as material relation, and it is the third equation to solve the 1D blood flow dynamics.

For a 1D blood flow dynamics system, there are usually three types of BCs [102]. The first one is the BC defined at inlet of x=0 by flow rate profile Q, pressure, or area such as

$$Q(0,t) = f(t). \tag{3-43}$$

The other BCs can be defined at the outlets, where parameters of BCs depend on those of the outlets as given by 0D Windkessel model. The Windkessel based BCs relate to the blood flow rate and pressure by using an equation equivalent of an RCR circuit to account for the impact of the downstream vasculature. At each outlet i, the BC equation is given by

$$R_1 \frac{\partial Q(x_i,t)}{\partial t} + \frac{R_1 + R_2}{R_2 C} Q(x_i,t) = \frac{\partial p(x_i,t)}{\partial t} + \frac{1}{R_2 C} p(x_i,t), \tag{3-44}$$

where x_i refers to an outlet i. The above defines a 3-element Windkessel model consist of a proximal resistance R_1 in series with a parallel connected capacitor C and a resistance R_2 as show in Figure 3-4. R_1 represents the characteristic flow impedance of the peripheral artery, R_2 that of the distal artery and C the compliance of distal arteries. The outflow pressure at which flow to the microcirculation ceases is assumed to zero.

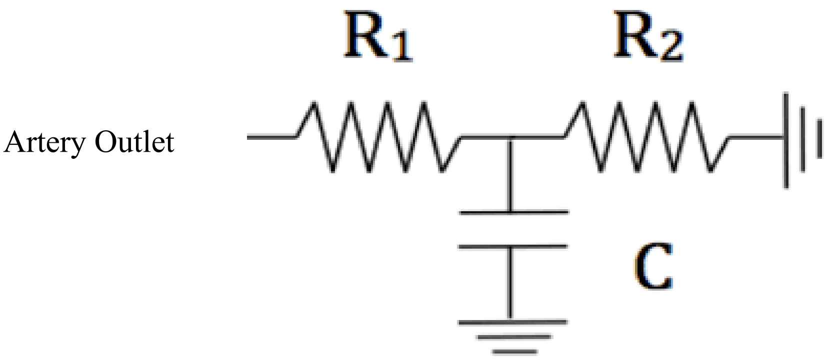

Figure 3-4 A schematic of the 3-element Windkessel model of blood flow dynamics.

Finally, if the vessel model has junctions, we assume conservation of flow and continuity of pressure at each junction as follows

$$Q_{pa}(x_{pa},t)=\sum_{i}^{n}Q_{d_i}(0,t), \tag{3-45}$$

$$p_{pa}(x_{pa},t)=p_{d_i}(0,t), i=1,\ldots,n, \tag{3-46}$$

where subscript “pa” denotes the parent vessel, d_i denotes the i^{th} daughter vessel, x=0 refers to the inlet and $x=x_{pa}$ denotes the length of the parent vessel.

3.3 Modeling of light scattering in tissues by radiative transfer theory

Light-tissue interaction is concerned in many clinical applications and optical and morphologic features of human tissues are important diagnostic indicators [103]. Human tissues are considered as turbid media. Light propagate in turbid media is driven by absorption and scattering events. Fundamentally, light-tissue interaction needs to be modelled by Maxwell equations or wave equations by consideration of optical heterogeneity of tissue on the scales of wavelength [104]. The computational costs of numerically solving these equations such as Finite-Difference Time-Domain or Discrete Dipole Approximation are simply too high once the sizes of tissues are much larger than light wavelength. Instead, the RT theory (Troitskii, 1954; Chandrasekhar, 1960; Sobolev, 1963) can be used to model such problems in which only the transport of light energy is considered[105]. It has been widely known that that the RT parameters can be associated with the differential absorption and scattering cross sections calculated by wave equations in turbid sample of particle suspensions [106] with low concentrations [106-109]. Therefore, the RT theory can be regarded as an approximation to the wave model of light-tissue interaction in which the phases of propagating electromagnetic wavefields are fully randomized due to multiple scattering and their effect on light distribution becomes negligible.

In turbid medium, light transport process is affected by elastic scattering with energy attenuated by absorption. The absorption and scattering events can be characterized by the RT theory that provides a framework to model light transport in a turbid medium. The RT equation is based on the balance of energy and its time-independent form can be expressed as [110]:

$$\mathbf{s}\cdot\nabla L(\mathbf{r},\mathbf{s}) = -(\mu_a+\mu_s)L(\mathbf{r},\mathbf{s}) + \mu_s \int_{4\pi} p(\mathbf{s},\mathbf{s}')L(\mathbf{r},\mathbf{s}')d\omega' + \varepsilon_e(\mathbf{r},\mathbf{s}) \tag{3-47}$$

where **s** is an unit vector in the direction of light propagation, L(**r**, **s**) is the radiance with a unit of W $\cdot$sr^{-1} $\cdot$m^{-2} describing the light energy flow rate propagating at **r** position and along **s** direction per unit of area and solid angle, μ_a in the unit of mm^{-1} is the absorption coefficient, μ_s is the scattering coefficient, p(**s**, **s**') is the scattering phase function describing the probability of light being scattered from **s**' to **s** direction, dω' is the differential solid angle along the direction **s**', ε_e(**r**, **s**) is the radiance density of light source at position **r** along a unit vector of direction **s** with a unit of W$\cdot$sr$^{-1}\cdot$m^{-3}.

The LHS of above equation provides the component of vector ∇L projected along the **s** direction which describes the increase of radiance per unit of pathlength along **s** direction. The RHS of above equation consists of three terms. The first term describes the attenuation rate of radiance per unit pathlength due to absorption and scattering loss along **s** direction. The second term means the increasing rate of L due to scattering of light from all other directions of **s**' to **s**. The third term is the radiance from external sources. Basically, the Eq. (*3-47*) describes the loss of L through absorption and scattering of photons out of **s** direction and the gain through scattering of photons from all others' directions and external sources. For our study here we can ignore the source term since human tissues concerned is source free. To clearly understand the meaning of μ_a and μ_s, we may break the radiance L(**r**, **s**) into three components as

$$L(\mathbf{r},\mathbf{s}) = L_a(\mathbf{r},\mathbf{s}) + L_s(\mathbf{r},\mathbf{s}) + L_{s'}(\mathbf{r},\mathbf{s})\,. \tag{3-48}$$

Then the Eq. (*3-47*) can also be separated into three equations:

$$\mathbf{s}\cdot\nabla L_a(\mathbf{r},\mathbf{s}) = -\mu_a L_a(\mathbf{r},\mathbf{s})\,, \tag{3-49}$$

$$\mathbf{s}\cdot\nabla L_s(\mathbf{r},\mathbf{s}) = -\mu_s L_s(\mathbf{r},\mathbf{s})\,, \tag{3-50}$$

$$\mathbf{s}\cdot\nabla L_{s'}(\mathbf{r},\mathbf{s}) = \mu_s \int_{4\pi} \mathrm{P}(\mathbf{s},\mathbf{s}')L(\mathbf{r},\mathbf{s})d\omega' + C_0\,, \tag{3-51}$$

where C_0 is a residue term representing the contribution of L_a and L_s to $L_{\mathbf{s}'}$.

By solving the Eq.(*3-49*)and Eq.(*3-50*), we can recognize the meanings of the two coefficients with μ_a^{-1} as the pathlength of a propagating light radiance attenuated to e^{-1} of its value at incident position due to absorption only and μ_s^{-1} as the corresponding pathlength due to scattering only. In Eq.(*3-51*), the scattering phase function p(**s**, **s**') is in general a function of polar and azimuthal angles measured from the **s** direction to **s**'. It could be simplified to a function of axial symmetry to reduce the complexity of modeling. A widely used function of axial symmetry to replace p(**s**, **s**') is the Henyey-Greenstein (HG) function $p_{HG}(\cos\theta)$ [110, 111], where the θ= **s•s**'. The HG phase function has been widely used since it has a simple functional form with single parameter as

$$p_{HG}(\cos\theta) = \frac{1-\mathrm{g}^2}{4\pi(1+\mathrm{g}^2-2\mathrm{g}\cos\theta)^{3/2}}\,. \tag{3-52}$$

The parameter g is equal to the angularly averaged value of cosθ if $p_{HG}(\cos\theta)$ is used as the distribution function

$$<\cos\theta>= \int_{4\pi} p(\mathbf{s},\mathbf{s}')\cos\theta d\omega' = 2\pi\int_0^{\pi} p_{HG}(\cos\theta)\cos\theta\sin\theta d\theta = g\,. \tag{3-53}$$

This leads to the designation of g as the anisotropy factor. Consequently, combine the RT equation and HG phase function, we define three RT parameters of μ_a, μ_s, and g to model light propagate in a turbid medium.

To apply the RT theory for modeling light propagation in a realistic tissue phantom, one must incorporate proper boundary conditions. Since light consists fundamentally of electromagnetic wavefields, the Fresnel equations for treatment of transport through an interface between different media are typically applied as boundary conditions. The Fresnel equations can be used to determine the reflection and refraction of light rays at the concerned interface by the real values of refractive indices of n and n' for neighboring media by the coherent reflectance [112, 113]. Thus, the four scalar parameters (μ_a, μ_s, g, n) provide the set of RT parameter to characterize propagation of light in heterogeneous turbid media.

3.4 Numerical modeling by Monte Carlo method

To model the iPPG signals as a reflection imaging problem, we adopted a statistical method of MC simulation as a method of choice to quantify light-tissue interaction within the framework of RT theory. With MC simulation as an accurate model of tissue optics, the reflection image data acquired by an iPPG system can be used to determine the optical or morphologic parameters of the imaged tissues containing artery network [114-116]. The high computational cost associated with MC simulations has been reduced significantly by development of parallel execution on graphics on a card of processing unit (GPU).

Most human tissues are highly turbid [110]. The light-tissue interaction is dominated by light scattering that makes analysis of the image data very challenging for accurate interpretation. The absorption of light depends on the molecular composition of the tissue while the scattering related to the morphological structure of the tissue components such as different skin layers and blood vessels [115]. Over last few decades, numerical algorithms and various measurement methods [114, 117-119] are employed to characterize tissues by the absorption coefficient μ_a, scattering coefficient μ_s, anisotropy factor g within the framework of the RT theory [110] and further the geometry of the tissue components [116]. The Monte Carlo theory employs the stochastic techniques in which random numbers with desired probability distributions are used to simulate the absorption and scattering processes defined with the RT equation coupled with specific boundary conditions.

3.4.1 Monte Carlo algorithm

Monte Carlo simulation allows calculation of the light distribution and detection by tracking photons within a tissue and signals acquired with detectors. A typical MC simulation tracks N photons or photon package as independent particles undergoing random events of scattering and absorption in a turbid sample characterized by optical parameters (μ_a, μ_s, g, n) and geometric parameters. The scattering events are implemented in a MC simulation to update the propagation direction and free pathlength at each event. The handling of absorption event differs in different implementations of the MC algorithms[114-116, 118, 120, 121]. By calculating the trajectories and propagation directions of all N photons in 3D space, one could obtain the light distribution and/or signals which can be measured. These include the cases of reflection imaging with a camera to record the spatial distribution of photons remitted from the tissue surface as iPPG images.

In statistical theory, a probability density function (pdf) $P(\xi)$ characterize the distribution of a random variable ξ and $P(\xi_0)d\xi$ gives the probability to find ξ between ξ_0 and $\xi_0+d\xi$. For example, the free pathlength $l_s \in [0, \infty]$ between two scattering events in an MC simulation can be treated as a random variable. The pdf of l_s can be defined as

$$P(l_s) = \frac{1}{Z_\lambda} e^{-\lambda l_s} \tag{3-54}$$

where λ is an adjustable parameter to satisfy the constrain and Z_λ is used for normalization. To ensure numerical calculation efficiency and statistical independence, one typically map the concerned random variable like l_s to a uniformly distributed random variable. This can be achieved by a random number (RND) $\xi \in [0, 1)$ from a widely available random number generator. Therefore, we define a function f to map the two random variables of ξ and l_s

$$\xi = f(l_s), \tag{3-55}$$

and requires that the two probability distribution functions satisfy the following equation

$$\int_{l_1}^{l_2} P(l_s^{'}) dl_s^{'} = \int_{f(l_1)}^{f(l_2)} P(\xi^{'}) d\xi^{'} . \tag{3-56}$$

Since P(ξ)=1, the accumulated probability of finding a photon having a free pathlength between 0 and l_s becomes

$$\xi = f(l_s) = P_d(0 \le l_s' \le l_s) = \int_0^{l_s} P(l_s')dl_s' . \tag{3-57}$$

This mapping relation yields the foundation for MC simulation of light-tissue interaction process in a turbid medium.

According to the solution of Eq. (3-50), the radiance L(**r**, **s**) of a propagating light at current position **r** from its incident position $\mathbf{r}_0$ is related by an exponential function. This solution combined with Eq. (*3-54*) yields the following equation

$$\frac{L(\mathbf{r},\mathbf{s})}{L(\mathbf{r}_0,\mathbf{s})} = \frac{P_d(l_s \le l_s' \le \infty)}{P_d(0 \le l_s' \le \infty)} = 1 - P_d(0 \le l_s' \le l_s) = e^{-\mu_s l_s} . \tag{3-58}$$

Applying the normalization condition of $P_{d_{ls}}(0 \le l_s < \infty) = 1$, we can derive

$$P_d(0 \le l_s' \le l_s) = 1 - e^{-\mu_s l_s} . \tag{3-59}$$

Then the pdf of scattering free pathlength $P_{l_s}(l_s) = \frac{dP_{d_{ls}}(0 \le l_s' \le l_s)}{dl_s} = \mu_s e^{-\mu_s l_s}$. Now, we can apply the mapping relation between RND=ξ and l_s of the MC algorithm in Eq. (*3-57*) to find

$$RND = \int_0^{l_s} P_{l_s}(l_s')dl_s' = 1 - e^{-\mu_s l_s} . \tag{3-60}$$

Invert the above equation leads to

$$l_s = -\frac{\ln(1-RND)}{\mu_s} . \tag{3-61}$$

Using the same method, we can obtain the absorption free pathlength l_a

$$l_a = -\frac{\ln(1-RND)}{\mu_a} . \tag{3-62}$$

3.4.2 Voxel based iMC algorithm

In our previous work, we have developed an iMC code that tracks photons in the finite volume of a heterogeneous tissue phantom [116]. Later, a updated MC based algorithm has been developed to rapidly obtain μ_a, μ_s with one optically thick sample at multiple wavelengths [121]. In the iMC algorithm, a total pathlength l_a is first determined from a RND before an incident photon starts to be tracked in a turbid sample. Then the first scattering pathlength l_{s1} is determined from another RND and the initial direction $\mathbf{s}_1$ of (θ_1, φ_1) or cosines (u_{x1}, u_{y1}, u_{z1}) for the tracked photon is determined from the Snell's law. The photon is followed as it propagates from an initial position $\mathbf{r}_{j-1}$ to $\mathbf{r}_j$ along $\mathbf{s}_j$ direction over pathlength l_{sj}. At the next position $\mathbf{r}_j$, one calculates an accumulated pathlength l_c defined as

$$l_c = \sum_{i=1}^{j} l_{si} , \tag{3-63}$$

where i=1, 2, 3, …, j is the number of scattering events occurred to the tracked photon, and l_{si} is the free pathlength of the i^th scattering event. The tracking of the photon stops when either it exits from the boundary of the medium or the cumulated free pathlength of all the scattering events l_c is bigger than the total pathlength l_a.

At each scattering event, iMC algorithm determines the direction of scattered photon $\mathbf{s}_i$ relative to the incident direction $\mathbf{s}_{i-1}$ in terms of the polar angle θ_i and azimuthal angle φ_i. If the scattering phase function is axially symmetric as the one given by the HG function, we can obtain polar angle and azimuthal angle directly from RND after re-scaling by 2π

$$\phi_i = 2\pi \cdot RND , \tag{3-64}$$

$$\cos\theta_i = \begin{cases} \dfrac{1}{2g}\{1+g^2-[\dfrac{1-g^2}{1-g+2g\cdot RND}]^2\}, if\ g \neq 0 \\ 2\cdot RND-1. \qquad\qquad\qquad if\ g=0 \end{cases} . \tag{3-65}$$

For iPPG images from human skin, the geometric configurations cannot be modeled accurately due to the irregular distribution of arteries. Thus, a voxelized iMC (viMC)code has been developed to handle arbitrary geometries so that arteries embedded in skin can be modeled with good flexibility. This new viMC is based on the definition of optical parameters for each voxel combined with our iMC algorithm. The voxel parameters include the location index of the voxel (ix, iy, iz), the sizes of the voxel (Δx, Δy, Δz), μ_a, μ_s, g and the real refractive index n. These voxel parameters are imported to the viMC program as a geometry configuration file.

The photon transports between two voxels is quantified by a voxel ray tracing algorithm [122] and described below. Each voxel has six y-z, x-z and x-y boundary planes and the distance from a corner point of i^th voxel to the origin of coordinate system is used to label the voxel location as (x_{ix}, y_{iy}, z_{iz}) with $x_{ix}= x_{ix-1}+\Delta x$, $y_{iy}= y_{iy-1} +\Delta y$, and $z_{iz}= z_{iz-1}+\Delta z$. Let's consider a photon located at **r** = (x, y, z) in the ith voxel after jth scattering event of free pathlength l_{sj}, it may hit any of 6 boundary planes of the voxel. The nearest distances to these planes can be obtained by projecting along the scattering direction $\mathbf{s}_j$. These possible propagation distances are calculated as a set of six numbers (X1, X2, Y1, Y2, Z1, Z2) with a schematic in x-y plane presented in Figure 3-5. The propagation distances are defined as:

$$\begin{aligned} &X1=\frac{x-x_{ix-1}}{u_x}, Y1=\frac{y-y_{iy-1}}{u_y}, Z1=\frac{z-z_{iz-1}}{u_z}, \\ &X2=\frac{x_{ix}-x}{u_x}, Y2=\frac{y_{iy}-y}{u_y}, Z2=\frac{z_{iz}-z}{u_z} \end{aligned} \quad . \tag{3-66}$$

where u_x, u_y, u_z are associated with the propagation direction of photon.

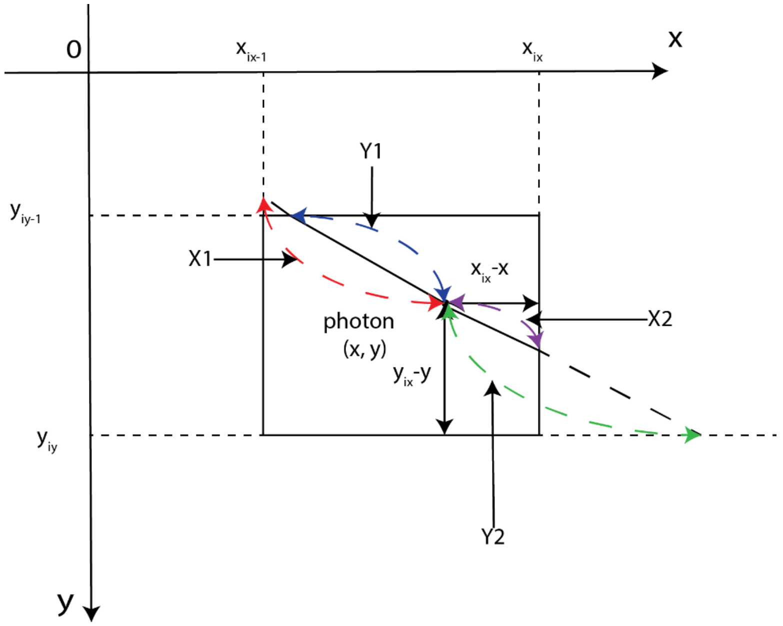

Figure 3-5 A schematic of the probability propagation in x-y plane.

There are three negative and three positive ones in the six possible propagation distances given a set of directional cosines of (u_x, u_y, u_z). The minimum positive value indicates the plane to be hit by the photon and provides distance from photon position at **r** to the plane, which is denoted as l_m. If $l_m > l_{sj}$, the photon travels over the free pathlength l_{sj} in the current voxel before the occurrence of next scattering event. If $l_m <= l_{sj}$, the photon enters the adjacent voxel of μ_a', μ_s', g', n' as optical parameters before the j^{th} scattering event. In this case, the residue free pathlength l_s' in l_{sj} and residue total pathlength l_a' in l_a need to be renormalized respectively as

$$\begin{aligned} l_s' &= \frac{n\mu_s}{n'\mu_s'}((l_s)_j - l_m), \\ l_a' &= \frac{n\mu_a}{n'\mu_a'}\{l_a - [l_m + \sum_{i=1}^{j-1}(l_s)_i]\} \end{aligned} . \tag{3-67}$$

where the refractive indices of n and n’ are used to account for the differences in optical pathlength in the two neighboring voxels.

3.5 iPPG data processing based on ICA algorithm

iPPG has emerged over the past two decades as a non-contact tool for retrieval of pressure pulse wave (PPW) related signals from image data [64, 68, 70, 123-132]. A video or raw image stack is acquired to record the spatiotemporal distribution of light backscattered from tissues in reflection mode. In this study, we have developed a novel and robust algorithm of pICA for retrieval of PPW related signals from monochromatic iPPG image stacks with high spatiotemporal resolutions.

An ICA algorithm of joint approximate diagonalization of eigenmatrices (JADE) was chosen for implementation of the pICA algorithm to isolate a cardiac component associated with the PPG signal from input signals of $\mathbf{I_n}(x, y; \lambda_p)$ after proper normalization [133, 134]. ICA assumes that the time dependence of input signals is caused by sources of different and statistically independent temporal variations. In our research, the signal sources include PPW driven by heartbeat at a mean rate of f_h and, among others, unintentional tissue motions and variations of tissues' optical properties unrelated to PPW. To perform ICA, K time vectors of $\mathbf{I}_{\mathbf{nk}}$ in row form are selected as the input signals with k $\in$ [1, K] that include a pixel of interest (POI) and pixels neighboring the POI. A linear relation is assumed input vectors of I_{nk} and unknown source vector of $\mathbf{S}_{k'}$ with k and k' $\in$ [1, K], then they can be related by an unknown mixing matrix [T] as

$$\begin{pmatrix} \mathbf{I}_{n1} \\ \vdots \\ \mathbf{I}_{nK} \end{pmatrix} = [T] \begin{pmatrix} \mathbf{S}_{1} \\ \vdots \\ \mathbf{S}_{K} \end{pmatrix}. \tag{3-68}$$

With the pixel data of iPPG in the form of $\mathbf{I}_{nk}$, one solves iteratively the mixing matrix [A] and output vectors of $\mathbf{S}_{\mathbf{k'}}$ until maximal statistical independence is achieved among $\mathbf{S}_{k'}$ that are called independent components (ICs). One IC given by $[T]^{-1}(\mathbf{I}_{n1}, \ldots, \mathbf{I}_{nK})^T$ is expected to be the cardiac component $\mathbf{S}_c$ for a POI near artery while other ICs of uncorrelated temporal variations are taken as the noise to be removed. For explaining the algorithm more clearly, we chose K=2 here to derive the formulas. The proposed pICA algorithm retrieves the PPG signals related to PPW from a monochromatic iPPG stack by illuminating the left hand of a volunteer with a light beam in a wavelength band of λ_p as the peak wavelength. Each image of the stack is segmented by separating all pixels into two groups of hand region and background region with a threshold $I_{max}/4$, where I_{max} is the maximum intensity of all pixels. The time dependence of each pixel intensity in the hand region of the image n can be expressed as a vector $\mathbf{I}_n(x, y; \lambda_p)$ with mean-center normalized components. By averaging the time vector $\mathbf{I}_n(x, y; \lambda_p)$ over all pixels in the hand region to obtain $I_{na}(t; \lambda_p)$, we determine the heartbeat rate f_h as the peak frequency within a band of width Δf_{hb} after Fourier transform of $I_{na}(t; \lambda_p)$ with Δf_{hb} set between 0.6Hz and 4.0Hz for the usual human heartbeat range.

For ICA based analysis of our measured iPPG stack data, we have carried out preliminary tests of different open-source codes and identified one that is based on the algorithm of JADE (Copyright (c) 2013, Jean-Francois Cardoso) algorithm built in Matlab for this study and set the number of components K defined in Eq. (*3-68*) at 3. The description of ICA-JADE algorithm is provided in the Appendix A. Throughout this study there are two different goals for processing the iPPG stack data with the ICA algorithm: One is to achieve high spatial resolution and the other to achieve significant SNR improvement. We have prepared two sets of input signals in the form of time vectors to meet these goals. The first set allows high spatial resolution in the outputs of ICA processing by defining single pixel-based input signal. In this set, the first signal vector is denoted as $\mathbf{I_p}(x, y; \lambda_p)$ at a location (x, y) of an image stack acquired at wavelength λ_p. And the two other input signals in Eq. (*3-68*) are formed by the time vectors averaged over pixels neighboring the one at (x, y). The second set of input signals are designed to improve SNR by increasing the areas for spatial averaging. A reference pixel area (RA) centered around a selected pixel at (x, y) is defined to obtain a time vector of $\mathbf{I_r}(x, y; \lambda_p)$ as the first input signal vector averaged over the pixels in RA. The other two input signals in this set are obtained by the two-time vectors of pixel intensities averaged over neighboring pixels outside of RA. For this set of input signals, the pixel numbers used for averaging are much larger than those used in the first set to increase SNR.

Before forming the input signals processing, we apply Z-Score normalization on each pixel of an input signals $\mathbf{I}_p$ (or $\mathbf{I}_r$). For example, the i^{th} component of the pixel time vector $\mathbf{I_p}(x,y)$ at a certain wavelength λ_p is normalized as

$$I_{p\_n}(x,y;i)=\frac{I_p(x,y;i)-\frac{1}{N}\sum_{k=1}^{N}I_p(x,y;k)}{(\frac{1}{N-1}\sum_{i=1}^{N}(I_p(x,y;i)-\frac{1}{N}\sum_{i=1}^{N}I_p(x,y;i))^2)^{1/2}}=\frac{I_p(x,y;i)-\mu_I(x,y)}{\sigma_I(x,y)} \qquad (3\text{-}69)$$

where μ_I and σ_I is respectively the mean and standard deviation over all discrete times. In the following discussion we dropped the pixel location (x, y) in notation for simplicity and assume all operations are performed for this pixel at λ_p unless noted otherwise. To simplify the matrix structure, we set $\mathbf{I_1}$ and $\mathbf{I_2}$ as two normalization input source vectors, $\mathbf{I_1}$ is $\mathbf{Ip\_n}$ or $\mathbf{Ir\_n}$, $\mathbf{I_2, \ldots, I_K}$ are the reference source vectors. Then the source matrix [I] and its covariance matrix [X] become

$$[I]=[\mathbf{I_1},\mathbf{I_2},\ldots,\mathbf{I_K}]^T, \qquad (3\text{-}70)$$

$$[X]=E\{([I]-E\{[I]\})([I]-E\{[I]\})^T\}=\begin{bmatrix}\mathrm{cov}(\mathbf{I}_1,\mathbf{I}_2) & \cdots & \mathrm{cov}(\mathbf{I}_1,\mathbf{I}_K)\\ \vdots & \ddots & \vdots\\ \mathrm{cov}(\mathbf{I}_K,\mathbf{I}_1) & \cdots & \mathrm{cov}(\mathbf{I}_K,\mathbf{I}_K)\end{bmatrix}. \qquad (3\text{-}71)$$

where E{ } is the expectation of the concerned random variables. After obtained [X], we calculated its eigenvalues ν_i and eigenvectors $\boldsymbol{\gamma}_\mathbf{i}$, which satisfied the following formula

$$\upsilon_i\boldsymbol{\gamma}_\mathbf{i}=[X]\boldsymbol{\gamma}_\mathbf{i}, i=1,2,\ldots,K. \qquad (3\text{-}72)$$

And assume $\nu_1 >= \nu_2 \ldots >= \nu_K$, then, we obtained the scaled principal component matrix $[B_r]$

$$[B_r]=[\frac{\boldsymbol{\gamma}_\mathbf{1}}{\upsilon_1^{1/2}},\frac{\boldsymbol{\gamma}_\mathbf{2}}{\upsilon_2^{1/2}},\ldots,\frac{\boldsymbol{\gamma}_\mathbf{K}}{\upsilon_K^{1/2}}]. \qquad (3\text{-}73)$$

Now the whitening matrix of [X] denoted as [W] becomes

$$[W]=([B_r][X])^T \qquad (3\text{-}74)$$

For a more intuitive understanding of estimating and diagonalizing the cumulant matrices, we created a symmetric matrix [Y] to store the optimized cumulant matrices.

$$Y=[Y(\mathbf{W_1},\mathbf{W_1}),\ldots,Y(\mathbf{W_m},\mathbf{W_m}),Y(\mathbf{W_m},\mathbf{W_{m\text{-}1}}),\ldots,Y(\mathbf{W_m},\mathbf{W_1})]. \qquad (3\text{-}75)$$

Each cumulant sub-matrix [Y($\mathbf{W_i}$, $\mathbf{W_j}$)] is defined as

$$[Y(Wi,Wj)] = (\sqrt{2})^{1-\delta_{ij}}\{\frac{([\mathbf{W_{ij}},\mathbf{W_{ij}},\mathbf{W_{ij}}]\odot[W])'}{N} - [E[W]]\delta_{ij} - \mathbf{e_i}\mathbf{e_j} - \mathbf{e_j}\mathbf{e_i}\}, \qquad (3\text{-}76)$$

where $\odot$ is Hadamard product which is a binary operation that takes two matrices of the same dimensions and produces another matrix of the same dimension as the operands, [E[W]] is an identity matrix with the same dimension as [W] as defined in Eq.(*3-1*), $\mathbf{e_i}$ is the column vector of [E], and $\mathbf{W_{ij}} = \mathbf{W_i} \odot \mathbf{W_j}$.

Then we initialized the eigenvector matrix of [W] before optimizing it using a "single" column vector from [W]. For example, we used $\mathbf{W_1}$ to obtain an initial rotation matrix [M], as [M] =[Y($\mathbf{W_1}$, $\mathbf{W_1}$)], and calculate the rotation results of the cumulant matrix as [Π]=$[M]^T$[Y].

To optimize the rotation matrix [X], we need do a loop here. For each pair of (a, b) with a ∈ (1, 2, …, K-1) and b ∈ (a+1, a+2, …K) as two numbers, we obtained a Givens' rotation matrix [A] about $\mathbf{M_a}$ and $\mathbf{M_b}$ in [M], which is a 2x2 matrix calculated as

$$[A] = \begin{bmatrix} A_{11} & A_{12} \\ A_{21} & A_{22} \end{bmatrix} = \begin{bmatrix} [O]-[P] \\ [Q]+[R] \end{bmatrix}\begin{bmatrix} [O]-[P] & [Q]+[R] \end{bmatrix}, \qquad (3\text{-}77)$$

where [O]= [Π (a,a), Π (a,a+K), …, Π(a,a+K*(n-1))], [P]= [Π(b,b), Π(b,b+K), …, Π(b,b+K*(n-1))], [Q]= [Π(a,b), Π(a,b+K), …, Π(a,b+K*(n-1))], [R]= [Π(b,a), Π(b,a+K), …, Π(b,a+K*(n-1))] with n= K(K+1)/2, the symbol Π (a,b) means the element (a, b) of matrix [Π]. Thus, the angle of the Given's rotation matrix [A] is calculated as

$$\tan 2\phi = \frac{A_{12}+A_{21}}{A_{11}-A_{22}+\sqrt{(A_{11}-A_{22})^2+(A_{12}+A_{21})^2}} \qquad (3\text{-}78)$$

In order to get the scaled principal component matrix [Br] closer to be orthogonalized, the rotation angle ϕ needs to approach zero. We set a threshold value T, for example 10^{-6}, if ϕ>T, then update the relative vector in the matrix [Π] and [M] as follow and select another number par (a’, b’):

$$\begin{bmatrix}\mathbf{M}_{\mathbf{a}} & \mathbf{M}_{\mathbf{b}}\end{bmatrix}=\begin{bmatrix}\mathbf{M}_{\mathbf{a}} & \mathbf{M}_{\mathbf{b}}\end{bmatrix}*[\begin{matrix}\cos\phi & -\sin\phi \\ \sin\phi & \cos\phi\end{matrix}], \tag{3-79}$$

$$\begin{bmatrix}\mathbf{\Pi}_{\mathbf{a}} \\ \mathbf{\Pi}_{\mathbf{b}}\end{bmatrix}=\begin{bmatrix}\cos\phi & \sin\phi \\ -\sin\phi & \cos\phi\end{bmatrix}*\begin{bmatrix}\mathbf{\Pi}_{\mathbf{a}} \\ \mathbf{\Pi}_{\mathbf{b}}\end{bmatrix}, \tag{3-80}$$

$$\begin{aligned}&\begin{bmatrix}\mathbf{\Pi}_{\mathbf{a}} & \mathbf{\Pi}_{\mathbf{a+m}} & \cdots & \mathbf{\Pi}_{\mathbf{a+m(M-1)}} & \mathbf{\Pi}_{\mathbf{b}} & \mathbf{\Pi}_{\mathbf{b+m}} & \cdots & \mathbf{\Pi}_{\mathbf{b+m*(M-1)}}\end{bmatrix}\\ &=[\cos\phi\mathbf{\Pi}_{\mathbf{a}}+\sin\phi\mathbf{\Pi}_{\mathbf{b}} \quad \cos\phi\mathbf{\Pi}_{\mathbf{a+m}}+\sin\phi\mathbf{\Pi}_{\mathbf{b+m}} \quad \ldots \quad \cos\phi\mathbf{\Pi}_{\mathbf{b+m(M-1)}}+\sin\phi\mathbf{\Pi}_{\mathbf{b+m(M-1)}}\\ &\quad -\sin\phi\mathbf{\Pi}_{\mathbf{a}}+\cos\phi\mathbf{\Pi}_{\mathbf{b}} \quad -\sin\phi\mathbf{\Pi}_{\mathbf{a+m}}+\cos\phi\mathbf{\Pi}_{\mathbf{b+m}} \quad \ldots \quad -\sin\phi\mathbf{\Pi}_{\mathbf{a}}+\cos\phi\mathbf{\Pi}_{\mathbf{b+m(M-1)}}]\end{aligned}, \tag{3-81}$$

where, $\mathbf{M_i}$ means the ith column vector of the matrix [M], $\mathbf{\Pi_i}$ means the ith row vector of the matrix [Π]. If ϕ<T, we obtain the optimized rotation matrix at the loop (a, b), denoted as [M_o] and the separating matrix [B_o] becomes:

$$[B_o]=[M_o]^T[B_r]. \tag{3-82}$$

Generally, we calculated the strongest source in the matrix [B_o] by sorting the source vectors of [B_o] in ascending order. This ascending order is according to the sorting of the ‘pseudo’ inverse matrix of [B_o]. Used ‘pseudo’ here because [B_o] may not have an inverse. The ‘pseudo’ inverse matrix of [B_o] is denoted as [C] which satisfied

$$[B_o][C][B_o]=[B_o]. \tag{3-83}$$

After the sorting, we finally obtain the separating matrix [B_s] as the final form of [B_o]. Now, the output source vector of ICA named as S_{ica} is given by

$$[S_{ica}]=[B_s][I]. \tag{3-84}$$

Among the K=3 ICA components or output source vectors, we selected the one whose frequency is in a range centered on f_{adj} with a width of ±10% f_{adj} as the signal source related to the heartbeat.

CHAPTER 4 NUMERICAL SIMULATION

The iPPG data acquired through this dissertation research are presented in the form of reflection images. Analysis of these image data and subsequent interpretations require an accurate modeling with an iMC based tissue optics model coupled with the fluid dynamic model of blood pressure wave propagation in additional to code optimization and parallel execution. In this chapter, we present the results of fluid dynamic simulations of blood in a single common carotid artery to validate the code and extended the modeling study to radial artery imaged by our iPPG system. Here we quantitatively analyzed different blood flow conditions, determined variation of radial artery radius during a cardiac cycle and calculated the values of pulse wave velocity for different arterial stiffnesses. We also present the results of MC simulations with different sets of tissue phantom configurations, optical parameters, and obtained the simulated iPPG waveforms under different artery conditions.

4.1 1D blood flow model and results

As derived in Chapter 3, the 1D fluid dynamic model treats blood as a Newtonian, incompressible fluid in an artery of elastic wall. The model consists of three equations of mass conservation given by Eq. (*3-14*), momentum balance by Eq. (*3-35*), a material relation by Eq. (*3-42*). In addition, a RCR Windkessel model is used to provide boundary conditions at the outlet plane by Eq. (*3-44*) and suitable initial conditions of blood flow rate at the inlet plane. Among various choices tested in this dissertation research for implementation of the 1D model, we selected an open-source code of SimVascular [135] for our numerical simulations which is based on a stabilized space-time finite element method with details of algorithm given in [136] . In this section, we present simulation results obtained by the SimVascular software that illustrate important characteristics of blood flow and pressure wave in different artery segment as deformable vessels. The execution details of 1D blood flow simulation can be found in the Appendix B.

In each simulation case, we set the step sizes for time discretization and size of finite elements of a concerned artery. More importantly, we examined the dependence of simulation results on the material properties and boundary conditions. Figure 4-1 shows a schematic representation of the artery configuration used in this study. The boundary conditions are given by the flow rate at the inlet and Windkessel model parameters at the outlet. The 1D geometry of the artery is characterized by the vessel diameters, wall thickness and length.

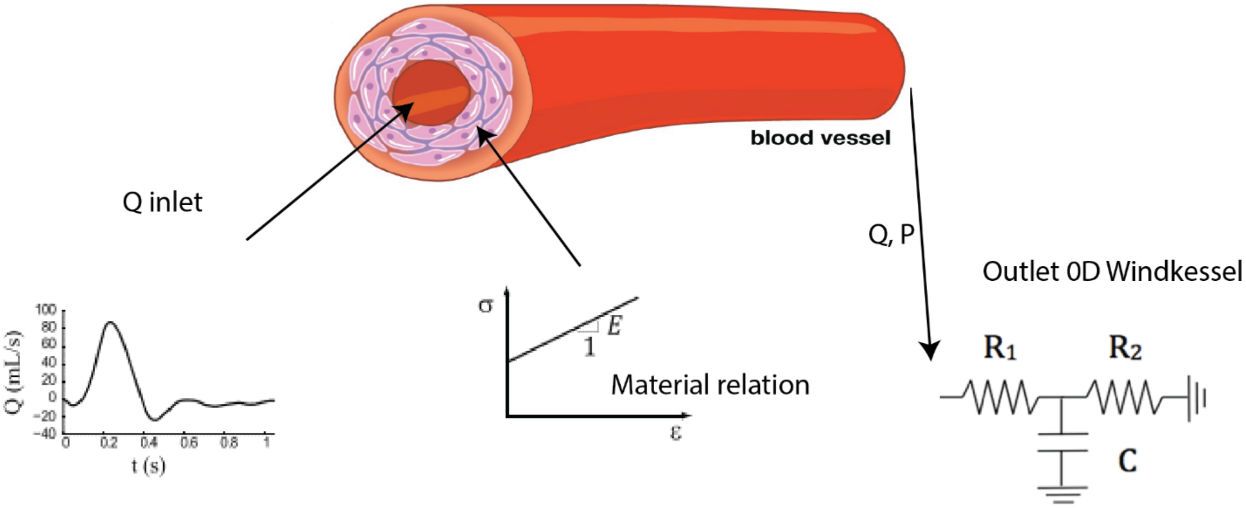

Figure 4-1 Schematic of the 1D fluid dynamic model for blood flow designed for this study.

Common carotid artery modeling

We first investigated a deformable artery of the common carotid artery in the form of a straight cylinder with properties independent of axial coordinate for comparison to published work for validating the code [102]. Carotid artery is a large artery that provides main blood supply to the head and neck. The outlet boundary condition for simulation of blood flow in large arteries is typically handled by a 0D Windkessel model of RCR circuit located at the outlet of the vessel to simulate the effect of downstream artery on the blood flow. The other parts of the boundary condition are given by setting the external pressure to a constant value of atmospheric pressure at the outside of vessel side wall and the outlet of the RCR circuit. The parameters of geometry and mechanical of the human common carotid artery are listed in Table 4-1 that also includes those ones related to the initial conditions at the inlet [102]. The systolic pressure at the systolic peak is the maximum pressure in a cardiac cycle and denoted as P_s in the following table while the diastolic pressure is the minimum pressure at the first foot of a cycle and denoted as P_d.

Table 4-1 Hemodynamic properties of the human common carotid artery (CGS & SI Units).

Property	Value
Length, L	12.6 cm
Radius at diastolic pressure, r_d	0.3 cm
Wall thickness, h	0.03 cm
Young's modulus, E	7.0 e+6 dyne/cm^2
Mean flow rate, $\overline{Q_{in}}$	6.5 ml/s
Systolic pressure, P_s	1.67 e+5 dyne/cm^2
Diastolic pressure, P_d	1.09 e+5 dyne/cm^2
Windkessel resistance, R_1	2487.5 (dyne/cm^2) s cm^{-3}
Windkessel resistance, R_2	18697 (dyne/cm^2) s cm^{-3}
Windkessel compliance, C	1.7529 e-5 cm^{-3} (dyne/cm^2)$^{-1}$
Blood density, ρ	1060 kgm^{-3}
Blood viscosity, μ	4 mPa

The simulation parameters were given by the time step Δt = 0.1ms, total number of time steps N_t=8800, total simulation time 8.8 s for 8 cardiac cycles, the spatial step Δx=0.042mm with total number of spatial steps N_x=300. We denote the initial inlet area as S(0, t)=S_0 which relates to the reference diastolic area S_d as

$$S_0 = S_d(1-\sqrt{S_d}\frac{P_d}{\beta})^2, \tag{4-1}$$

where $S_d = \pi r_d^2$, $\beta = \frac{4}{3}\sqrt{\pi}hE$ and $P_d(t)=p(0,t)$ is the inlet pressure. For the temporal profile of $P_d(t)$ at the inlet, we adopted the flow rate profile from [102] as an *in vivo* signal, and the wall is assumed to be linearly elastic characterized by the Young's modulus. Figure 4-2 shows common carotid simulation results of different flow parameters versus time t including the inlet flow rate, the outlet flow rate, the outlet pressure and cross-section area. Generally, the waveforms in the first few cycles are affected by initial conditions as flow rate, pressure or radius of artery wall. An iteration approach was employed to simulate the periodic propagation of flow rate and pressure waves. Iteration is carried out over 8 cycles to reach a stable simulated waveform. In our simulation, the stable solution starts in the second cycle.

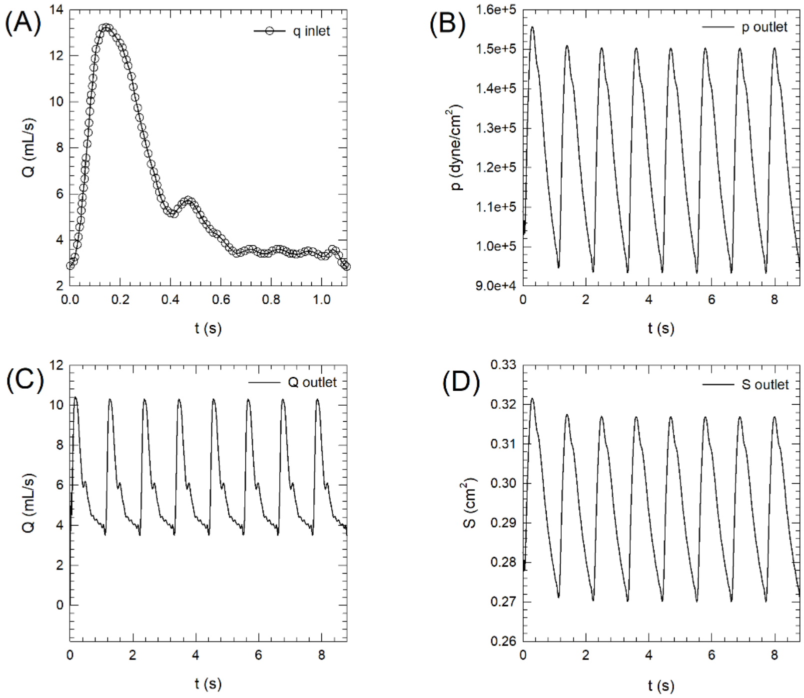

Figure 4-2 Simulation results of blood flow parameters versus time t of common carotid artery: (A) flow rate Q at the inlet; (B) blood pressure p at the outlet; (C) flow rate Q at the outlet; (D) cross-section area S at the outlet.

To validate the 1D model we compare the effects of vessel length and wall elasticity on blood flow for different boundary conditions at the inlet. We compared the pressure profile at inlet, mid-point and outlet of the common carotid artery as shown in Figure 4-3. The left, middle, right column are the result at vessel length equals to 10.6 cm, 12.6 cm, and 14.6 cm respectively. The top row is the spatial blood pressure waveforms along the axial of artery which reaches a stable waveform during the second cycle. The bottom row is the temporal blood pressure profile at inlet, mid-point, and outlet during this period. The time of the last foot before the systolic upstroke increases along the vessel length, indicating the propagation of the pressure wave, and the same tendency can be seen for the variations of P_d and P_s.

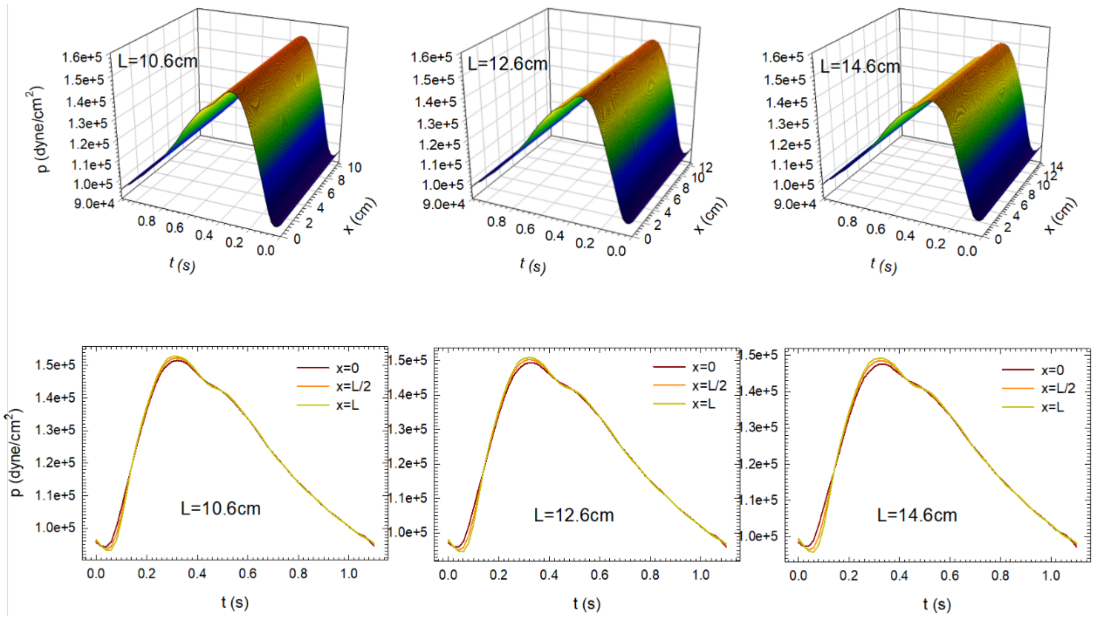

Figure 4-3 Pressure profiles of a single common artery in the second cycle at different artery lengths.

The results of varies of the cross-section area at different vessel lengths are plotted in Figure 4-4. The difference time of the first foot at the beginning of systolic upstroke, and the first peak or named the systolic peak increase along the vessel length. This phenomenon is similar to the case of pressure profile in Figure 4-3 because of the material relation we approximated as Eq. (*3-42*) where pressure and artery radius r is linearly. Flow rate is not sensitive to vessel length in this simulation, the results show in Figure 4-5. The layouts of Figure 4-4 and Figure 4-5 are the same as described in Figure 4-3.

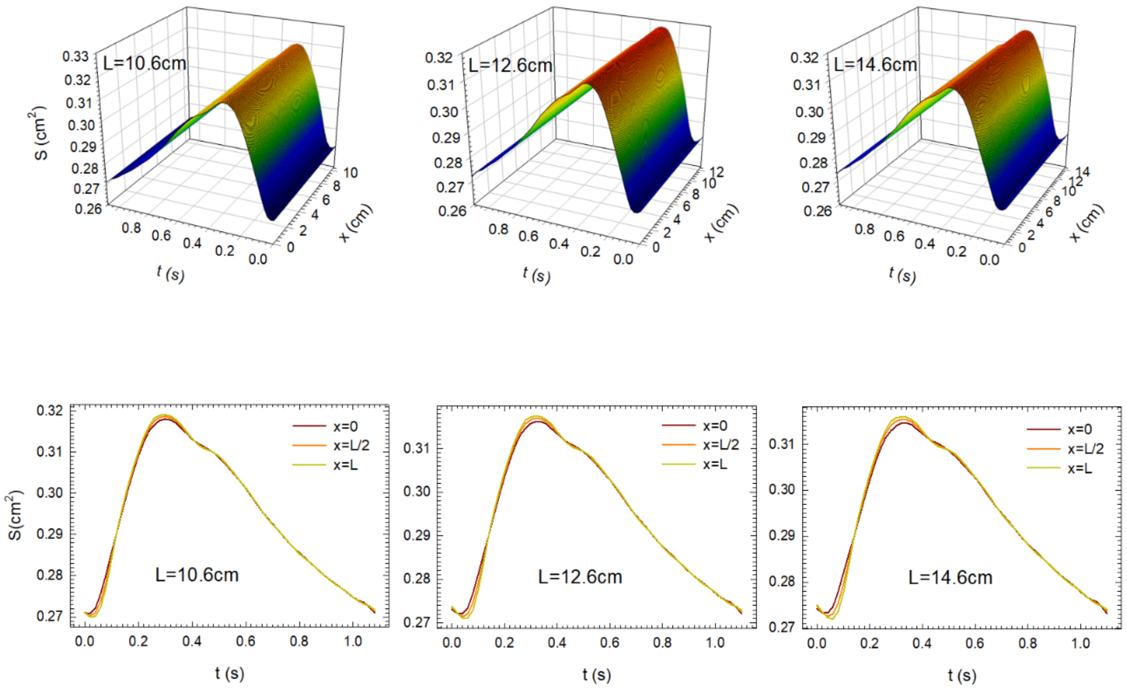

Figure 4-4 Cross-section area of a single common artery in the second cycle at different artery lengths.

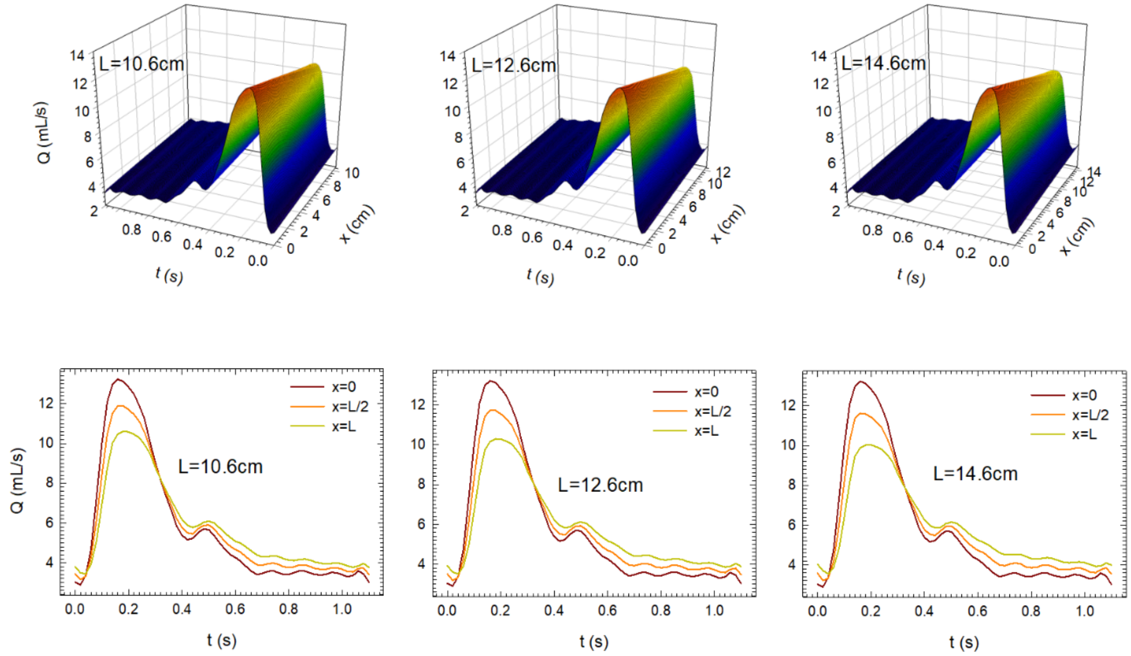

Figure 4-5 Flow rate profile of a single common artery in the second cycle at different vessel lengths.

In our study, the artery wall is assumed to be linearly elastic by treating the Young's modulus E of artery wall as a constant parameter along the artery. Using the same setting of parameters listed in Table 4-1, and denoted $E_0=7\text{x}10^6$ dyne/cm^2 as a physiologically normal value [102], the time and spatial dependences of pressure, flow rate and cross-section area of the common artery at different values of E are shown in Figure 4-6, Figure 4-7 and Figure 4-8 respectively. In each figure, the top row provides the spatial profiles along the axial direction of the artery during the second period and the bottom row illustrates the temporal profiles at inlet, mid-point, and outlet during the cycle. From the Figure 4-6, we found that the blood pressure profile is sensitive to the value of Young's modulus E of the artery wall. Specially, for 'soft' artery with E set to $0.1E_0$, there are numerous of wave foots and peaks in a cycle. We can see from the Figure 4-6, P_d decreases but the P_s increases as the value of E increases. But the time variations of the first foot of the waveform at different locations become smaller when the value of E increases. The difference time of the first foot between inlet and outlet is around 0.5s at the case $E=0.1E_0$, but it almost the same when $E=10E_0$.

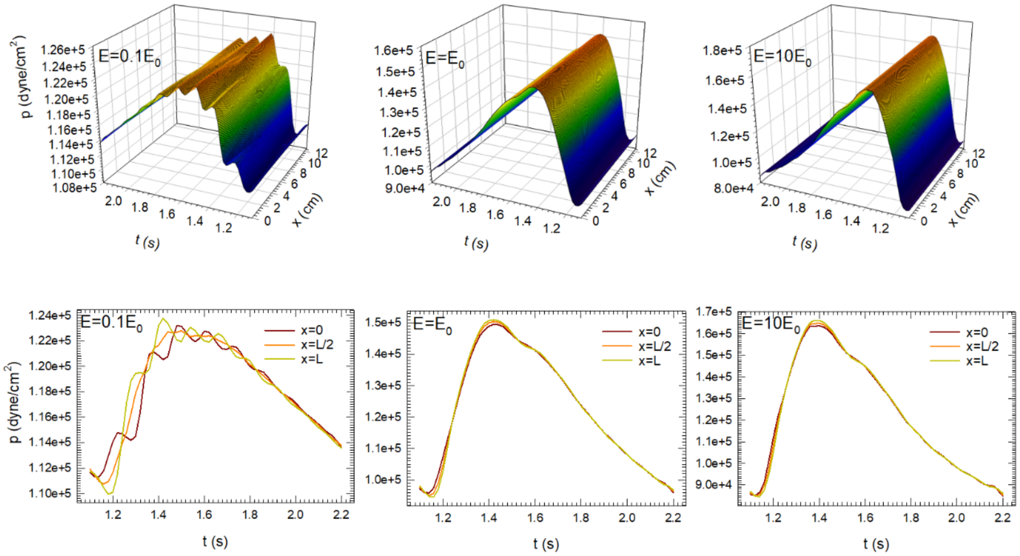

Figure 4-6 Pressure profile of a single common artery modeled at different values of E.

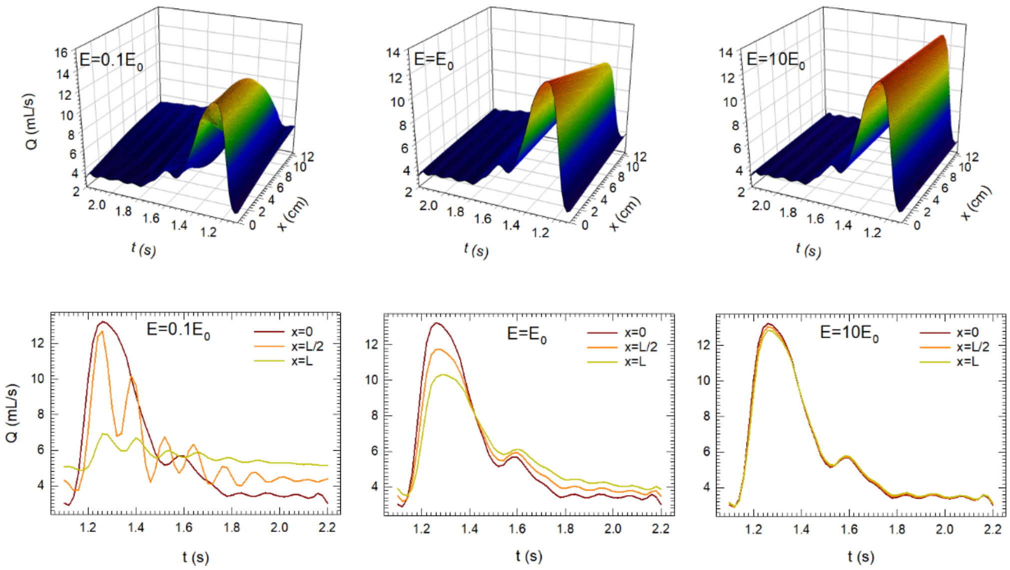

Figure 4-7 Flow rate of a single common artery modeled at different values of E.

For flow rate, we can find through Figure 4-7, as artery wall harden with increasing E, the profile of flow rate decreases more slowly from the inlet to outlet. In the condition of E=10E$_0$, the flow rate at the outlet almost keeps the same as at the inlet except the peak of the profile is slightly smaller. But when E decreases to 0.1E$_0$, the flow rate decays to around 6 mL/s at the outlet, especially during the second half cardiac cycle or the diastolic phase. The result of the vessel cross-section area S shows in Figure 4-8. Different from the results of variation of vessel lengths cases, the tendency of S with different E is not the same as the pressure variation. We found that the most significant variation of S at different locations is in the case of the Young's modulus E= E_0, and the range of variation in cross-section area of artery increases as the value of E decreases.

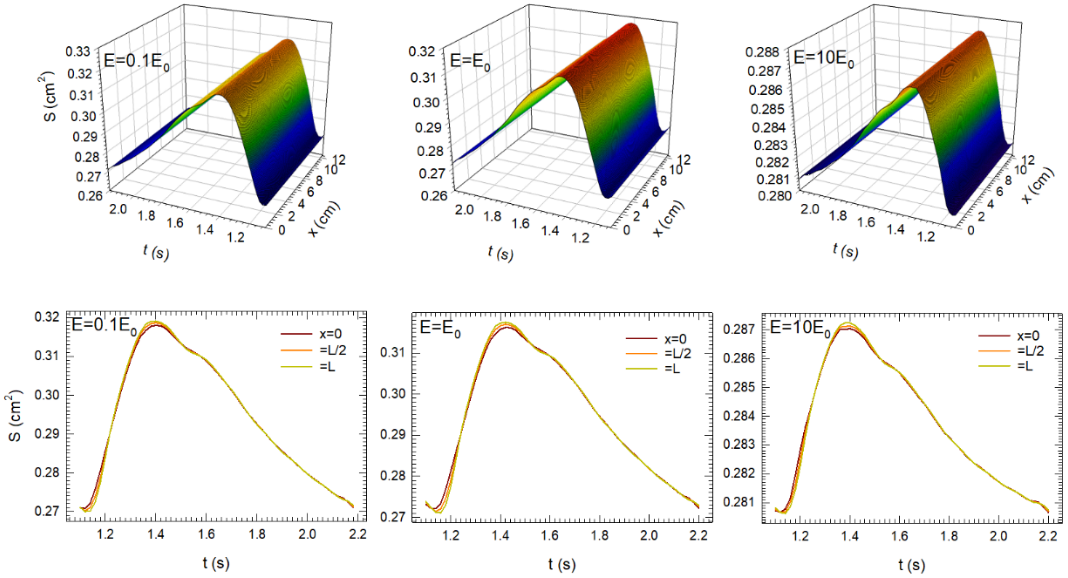

Figure 4-8 Cross-section area of a single common artery modeled at different values of E.

4.1.2 Radial artery modeling

After validation of the 1D blood flow model by a single common carotid artery, we focus rest of simulation study on the radial artery which are related to the measured iPPG image stack for this dissertation study. The radial artery is a large blood vessel which provides oxygenated blood to the lateral aspect of the forearm, wrist, and hand. It is considered as a deformable vessel in the form of a straight cylinder with properties independent of axial coordinate. The inlet flow rate profile is an *in vivo* signal taken from the ‘Figure 13’ in [137]. The initial value P_d is set to 1.0×10^5 dyne/cm^2 as a common value, the mean flow rate is estimated from the inlet flow rate profile. The outlet boundary condition is handled by a 0D Windkessel model of RCR circuit. The values of the artery geometry, mechanical and initial conditions listed in Table 4-2 were taken from [138]. The number of time step is 8000 with step size Δt=0.001s, and the spatial step number is 300. The same as we set in the study of the common artery above, we still simulate eight cardiac cycles which has a new cardiac cycle time 1s instead of 1.1s in the common artery case. Figure 4-9 shows the simulated temporal profiles of inlet flow rate, the outlet flow rate, the outlet pressure, and the outlet area. In this simulation, a stable solution was obtained after 2 cycles. If we change the unit from CGS to SI, the values of P_d and P_s at the outlet are about 71mmHg and 111mmHg, which are agreement with normal blood pressure.

Table 4-2 Hemodynamic properties of the radial artery (CGS UNIT & SI Unit).

Property	Value
Length, L	23.5 cm
Radius at diastolic pressure, r_d	0.17 cm
Wall thickness, h	0.017 cm
Young's modulus, E	7.00e+6 dyne/cm^2
Mean flow rate, $\overline{Q_{in}}$	1.14 ml/s
Systolic pressure, P_s	1.62e+5 dyne/cm^2
Diastolic pressure, P_d	1.0e+5 dyne/cm^2
Windkessel resistance, R_1	27539 (dyne/cm^2) s cm^{-3}
Windkessel resistance, R_2	31262 (dyne/cm^2) s cm^{-3}
Windkessel compliance, C	5.285e-7 cm^{-3} (dyne/cm^2)$^{-1}$
Blood density, ρ	1040 kgm^{-3}
Blood viscosity, μ	4 mPa

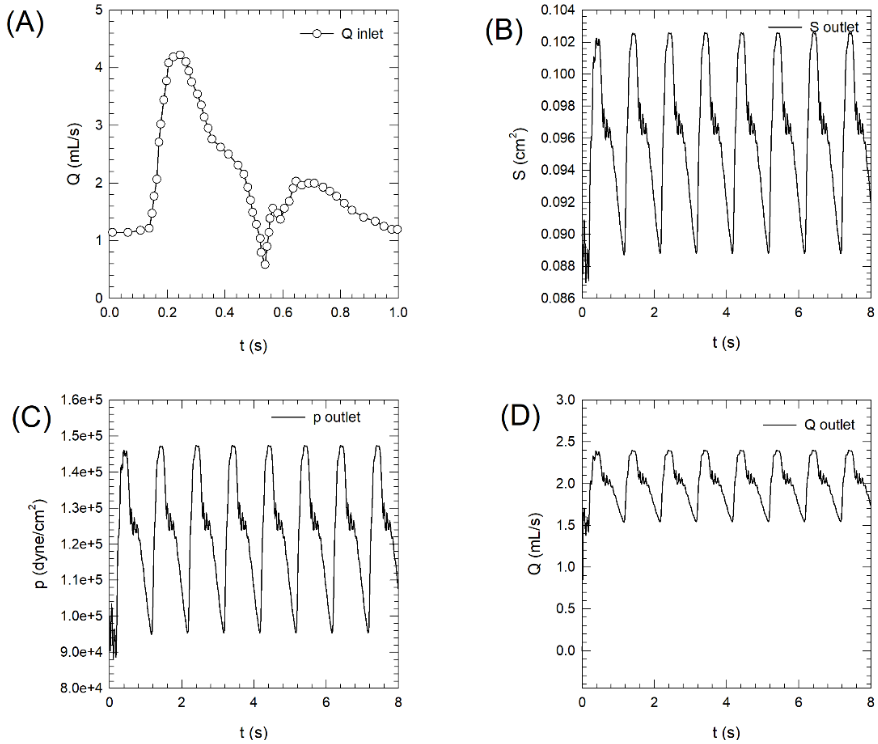

Figure 4-9 Simulation results of blood flow parameters versus time t of radial artery: (A) flow rate Q at the inlet; (B) cross-section area S with time at the outlet; (C) blood pressure p at the outlet; (D) flow rate Q at the outlet.

After radial artery travels across the wrist, it branches to form a network of blood supply vessels in the hand as palmar arch, common digital arteries. The strongest iPPG signals which obtained in our experiment study is considered around the outlet of the simulation radial artery model. The skin phantom size in our iMC study is around 1 to 2cm based of the computing cost and the memory size of the GPU card. To obtain the spatial radius along the simulation size in our MC simulation, we compared the variation of cross-section area S near the outlet of the radial artery. The results in Figure 4-10 A show that the tendency of the deformation of radial artery at the outlet are basically the same. Thus, we chose the radius at location x=22.8cm as the simulation data in our iMC study, and the radius profile is plotted in Figure 4-10 B.

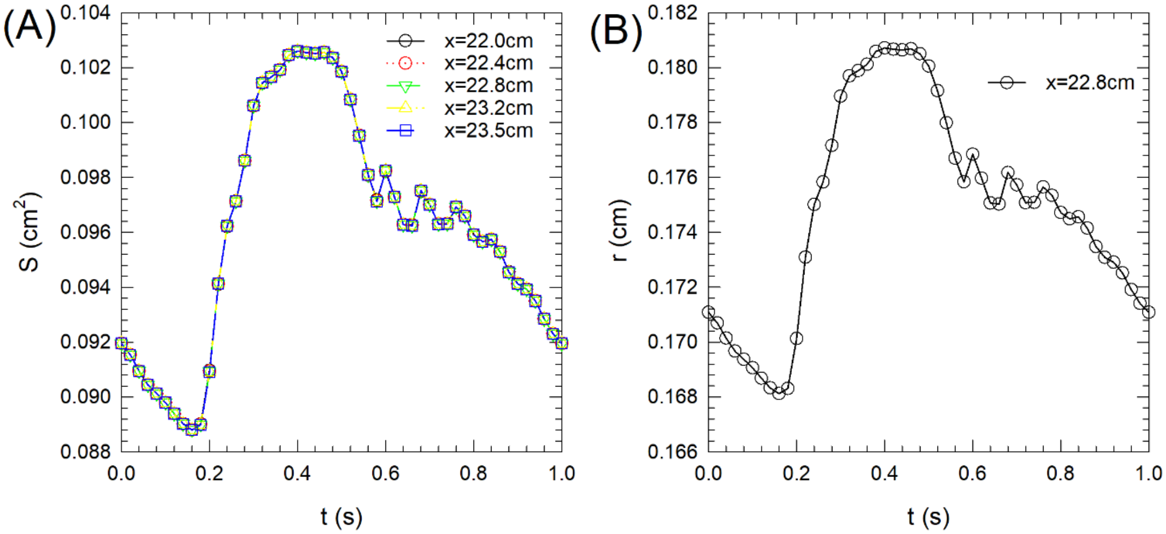

Figure 4-10 Deformation of artery size at the end of the radial artery in a cardiac cycle: (A) cross-section areas at 5 different locations; (B) the radius of radial artery at x=22.8cm.

To validate the boundary conditions at the outlet which called RCR Windkessel conditions, we compared the temporal pressure profile at the outlet in different Windkessel parameters. The simulation parameters we used in these cases are listed in Table 4-2. We denoted the total resistance as R_t with $R_t=R_1+R_2$ and increased the R_t from $R_{t0}=58801$ dyne ·s ·cm^{-5} to 1.2 R_{t0}. As shown in Figure 4-11 A, we found that the entire blood pressure profile rising with increased R_t. In Figure 4-11 B, we varied the compliance C from $C_0=5.285\text{x}10^{-7}$ dyne^{-1}·cm^{-1} up to $100C_0$. Different from the result in Figure A, the variation of P_d and P_s are significant bigger than others. That means the pressure difference given by P_s-P_d goes up with C. In Figure 4-11 C, we kept total resistance R_t constant as R_{t0} and varied the ratio of R_1/R_2. The pressure difference P_s-P_d goes down when the ratio decreases.

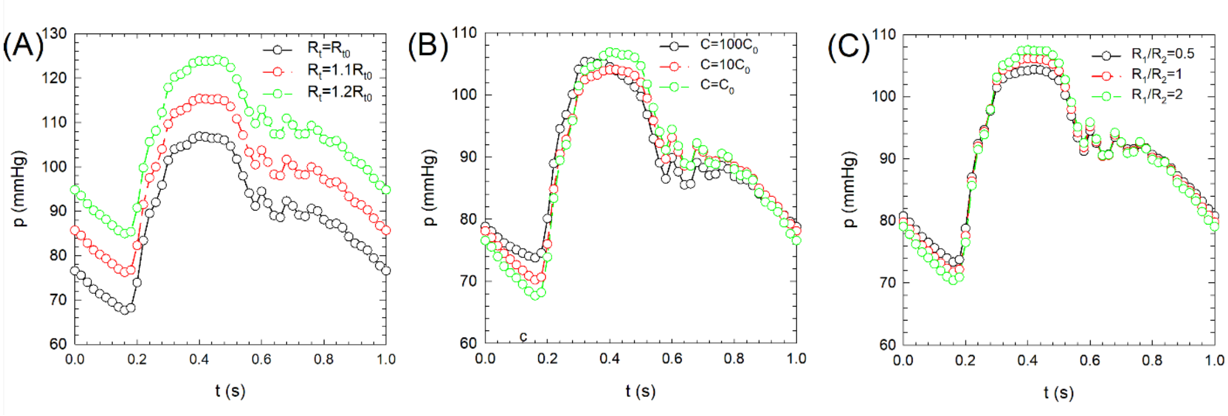

Figure 4-11   Impact of RCR Windkessel parameters: (A) the outlet blood pressure at different R_t, where $R_t=R_1+R_2$; (B) the outlet blood pressure at different compliance C; (C) the outlet blood pressure at different ratio of R_1/R_2.

In the iPPG waveform, beside of the systolic and diastolic peak, there is another feature called dicrotic notch. To explore how E effects dicrotic notch, we varied the Young's modulus of the radial artery wall from $3\text{x}10^6$ dyne/cm^2 to $2.2\text{x}10^7$ dyne/cm^2 of 10^6 dyne/cm^2 in step size. Figure 4-12 A shows the temporal pressure profiles at the outlet during a cardiac cycle with different values of E. We found out the same as the result in Figure 4-6, P_s becomes higher with increased E, but P_d inversed. We also found that the dicrotic notch pressures have a peak value at $E=9\text{x}10^6$ dyne/cm^2 although the appearing time of dicrotic notches keeps the same. The result is presented in Figure 4-12 B.

Occurred in parallel with the wider use of blood pressure measurements, identifying arterial stiffness as a factor was an important milestone in the understanding of clinical hypertension as well as in the development of treatment strategies [139]. We studied how the artery stiffness effect the PWV by variation values of Young's modulus E. We calculated PWVs from the delay of the pressure profile at different location of all the cases in Figure 4-12. As shown in Figure 4-13 A, $t_{L/2}$ is the time of P_d at location x=L/2 in a cardiac cycle, and t_L is time at x=L. The time delay of the pressure wave could calculate as t_L - $t_{L/2}$. We plotted t_L and $t_{L/2}$ versus E in Figure 4-13 B and found that t_L is more sensitive to the value of E than $t_{L/2}$. So, the PWV of radial artery blood becomes slower when the artery wall is 'softer'. From the Figure 4-13 C, we found that the relationship between the PWV and E is approximately linear, and the PWV varies from 6 m/s with E=3e^6 dyne/cm^2 to 18 m/s with E=2.2e^7 dyne/cm^2 in our simulation.

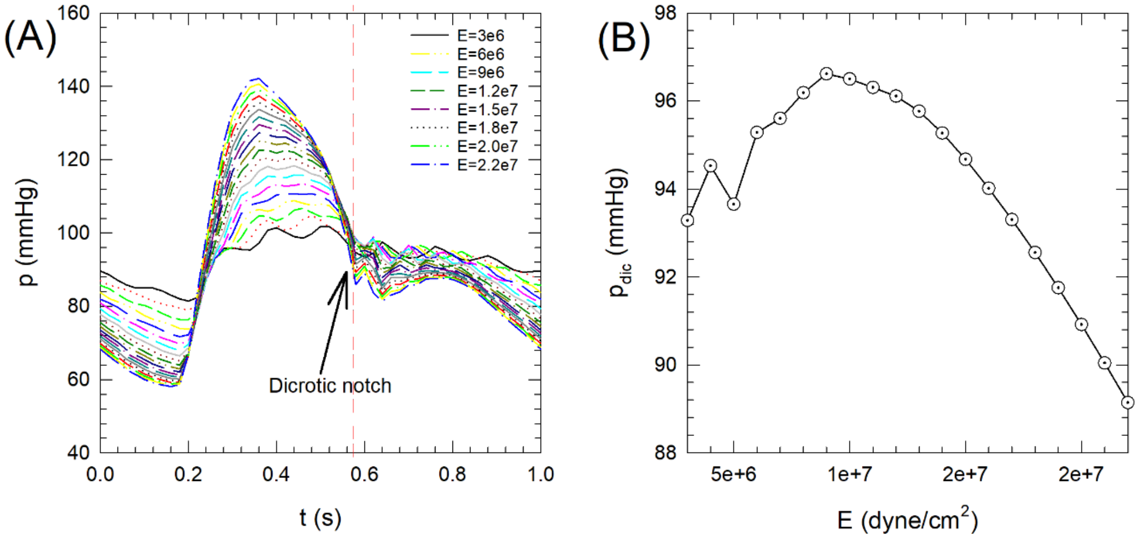

Figure 4-12 (A) Outlet pressure profiles with different values of E; (B) Dicrotic notch pressure at different value of E.

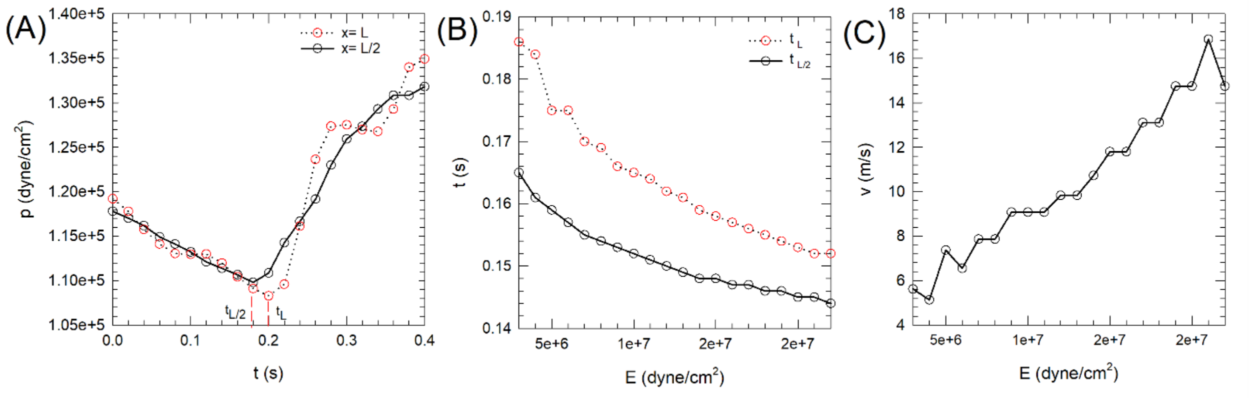

Figure 4-13 (A) Pressure profile of first foot before systolic upstroke at locations x=L/2 and L, where $t_{L/2}$ and t_L are the time of P_d in a cardiac cycle; (B) $t_{L/2}$ and t_L at different values of E; (C) simulated PWV of radial artery at different values of E.

4.2 Modeling of Tissue Optics by iMC simulations

The MC method is a stochastic solver of boundary-value problems based on the RT theory with Fresnel's equation as the boundary conditions. MC simulation provides an accurate tool for turbid media of complex structure to calculate light distributions near interfaces of modest or large index mismatch and at small source-detector distances. The main barrier to wide application of the MC methods lies in their high computational cost. With the rapid development of parallel computing platforms implemented with graphics processing units (GPUs), the MC method has gained increasing popularity in modeling of tissue optics over the past decade [140]. We have previously developed an iMC code that tracks photons in the finite volume for inverse determination of optical parameters of cutaneous nevi and normal skin tissue from melanoma patients [116]. For this dissertation research, we have developed a voxel based iMC code to incorporate blood vessels into the skin tissue phantom, which enables quantitative analysis of iPPG data in terms of artery parameters based on 1D blood flow model.

4.2.1 Tissue phantom configuration and coordination system

As show in Figure 4-14, a 3D Cartesian coordinate system is applied in our simulation for photon location tracking and a spherical coordinate system attached to the tracked photon for interaction of photon with matter. The origin of coordinate system is located on the incident surface of the skin tissue phantom. The z-axis is pointing toward inside of the phantom along the normal direction of this surface or x-y plane. To simulate iPPG imaging by LED arrays, three collimated beams of finite radius R and uniform intensity distribution illuminate the phantom with the same incident angle of $\theta=45^o$ from the z-axis but different azimuth angles of $\varphi=0^o$, 120^o, 240^o from the x-axis. The artery is considered as a cylinder of finite radius R_a with its symmetry axis in the x-z plane. The distance from this symmetry axis to phantom surface of x-y plane is denoted as d_a. All phantom voxels are of rectangular shape with sides along the coordinate axis. The voxel parameters consist of the voxel side lengths of Δx, Δy and Δz, the voxel index vector $\mathbf{J} = (i, j, k)$ with $i \in [0, N_x-1]$, $j \in [0, N_y-1]$ and $k \in [0, N_z-1]$, and the material type vector $\mathbf{M}_w = (n_w, \mu_{aw}, \mu_{sw}, g_w)$ of optical parameters with $w \in [1, N_m]$. In the above two vectors, the values of N_x, N_y, N_z and N_m are respectively given by the number of voxels along the x-, y- and z-axis and the material types. For example, if the phantom contains only three types of tissues as skin epidermis, dermis, and the blood in artery, then we have $N_w=3$, $\mathbf{M}_1$ for epidermis, $\mathbf{M}_2$ for dermis and $\mathbf{M}_3$ for artery. The ambient media around the phantom is air with refractive index defined as n_{air}. The tracked photon number on a voxel of $J|_{k=0}$ in the phantom surface at an incident angle θ is denoted as $N(\mathbf{J})$ and is calculated by integrating incident photon intensity over the voxel area as

$$N(\mathbf{J}) = \int_{s(\mathbf{J})} \rho(x, y, z) ds \,, \qquad (4\text{-}2)$$

where ρ(x,y,z) the arbitrary incident photon intensity distribution, s(**J**) the incident area of the voxel **J**.

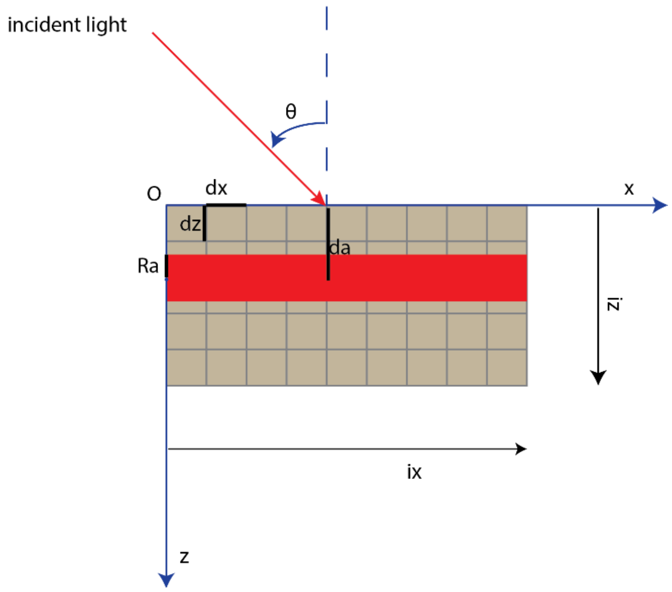

Figure 4-14 Source-sample configuration: red line indicates an incident light; shaded block indicates skin and red block artery.

4.2.2 Tissue parameters and photon tracking algorithm

Skin consists of epidermis on its outer part, which is squamous keratinized epithelium, and an inner layer called dermis, which is fibrous connective tissue. The hypodermis, which is a loose subcutaneous connective tissue, attaches the skin to underlying structures. Skin thickness varies regionally between 0.5 and 3mm. Generally, skin is classified into thick or thin depending on the thickness of the epidermis. The epidermis of thick skin is 0.8-1.5mm thick, and that of thin skin is 0.07-0.15mm thick [141]. Thick skin is found on the soles of feet and palms of hands, glabrous. Histologically, the boundary between avascular epidermis and vascularized dermis is highly corrugated. Here, to simplify the model, we considered the skin as a single layer of dermis and an artery is buried inside. In 2005, Ma X et al. reported the bulk optical parameters of porcine skin dermis at eight wavelengths [50]. Bosschaart N et al. provide the tabulated data for the compiled spectra of μ_a, μ_s, g of whole blood [51]. Based on those, our model could be simplified as two material contains dermis and blood. The light source wavelength is 850 nm which has better performance in our multi-wavelength iPPG research. The optical parameters of phantom at 850nm are taken from these two papers, show in Table 4-3.

Table 4-3 Optical parameters of whole blood and dermis at 850nm.

Wavelength	Sample types	μ_a	μ_s	g	n
850nm	Whole blood (98% spo2)	0.49	74.2	0.9832	1.4
	dermis	0.16	9.0	0.88	1.364

In our iMC study, the incident light beam is considered as totally N photons. For each photon, it is refracted at the phantom surface based on Fresnel' equation, then repeatedly scatters between voxels and then terminate propagation in two states. First state, it may be absorbed by tissues while its total pathlength l_a drop below zero. Second state, the photon escapes from the phantom to the ambient medium. During these scattering events, the photon scatter from one voxel to the adjacent voxel. For each scattering event, we determine if the photon enters to another voxel or out to the ambient medium as describing in section **3.4.2**. When the photon propagates to the ambient medium, it is record depending on whether it hits the detector. If the ambient medium is on the incident surface side, the photon is record as the reflection image data. And if the photon moves into adjacent voxel, it continues this scattering event or start a new scattering event, which depends on whether the propagation distance in current voxel bigger than the free pathlength l_s. When the photon enters a new voxel, the status of the photon is updated including the position, the direction, the voxel index, the optical parameters, and specially, the free pathlength l_s' and residue total pathlength l_a'. l_s' and l_a' are renormalized respectively by Eq. (*3-67*). The flowchart of the viMC code shows in Figure 4-15.

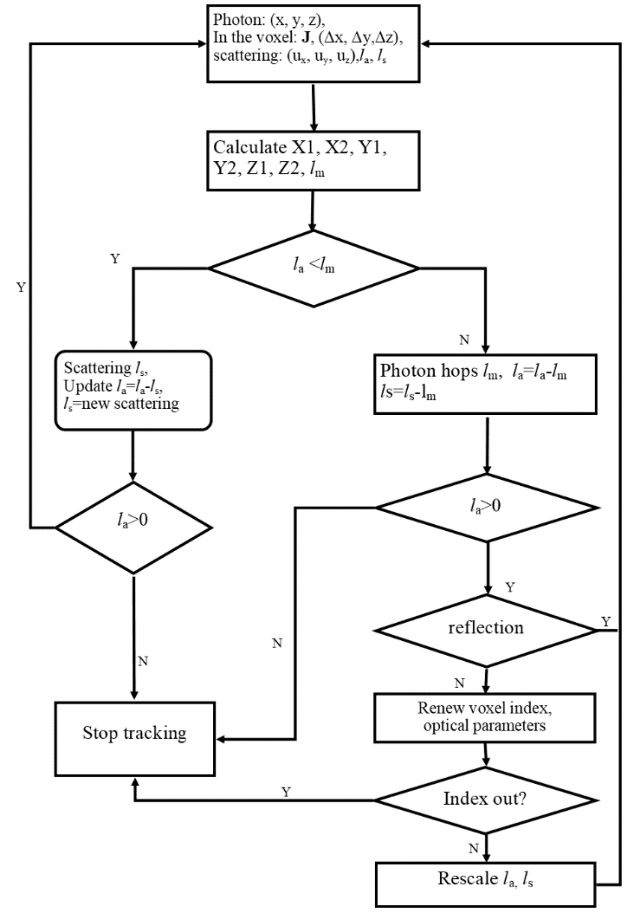

Figure 4-15 Flowchart of photon propagation in tissues phantom based on viMC method.

4.3 CUDA-based GPU programming and accelerating

In essence, the iMC simulation is a statistical method of photon transport in a medium under the framework of radiative transport theory and Fresnel' equations. To reduce statistical errors, the propagation of large number of photons needs to be simulated in our vivo studies of arterial blood interaction with light. The direct routine simulation would take amount of time. But according to the radiative transport theory, the tracking of individual photon is an independent process. These characteristics make our simulation a good candidate for parallel computing.

The GPUs is designed for highly parallel computations such as more transistors are devoted to data processing. Compute Unified Device Architecture (CUDA), introduced by NVIDIA in

2006, is a general-purpose parallel computing platform and programming model that allows developers to use high level programming language such as C, C++, Fortran. At its core are three key abstractions - a hierarchy of thread groups, shared memories, and barrier synchronization [142]. Basically, CUDA is a heterogeneous programming model, in which CPU and GPU are used. The CPU and its memory are referred as the host, and the GPU and its memory are referred as the device. Code programming on the host manages the memory on the host and the GPU device, then launches the kernel functions which executes on the device in parallel method by a huge amount of GPU threads. A thread is an independent execution context that can simulate an individual photon in our viMC algorithm. A typical procedure for converting code from C to CUDA-C could be divided into four steps. First, declares the input and output parameters and allocates host and device memory space for them. Second, initialize the host and device data and copy the host data to the corresponding device memory. then, rewrite code sections suitable for parallel computation into kernel functions and execute them. Finally, after processing, copy the result from device memory to host memory.

After code converting, improving parallel efficiency is our main goal. General graphics cards called device in CUDA, typically have numbers of streaming multiprocessors (SMs). SM creates, manages, schedules, and executes threads in groups of 32 parallel threads called warps. The parallel computing method is realized by an architecture named single-instruction, multiple-thread (SIMT). Threads can be identified using dimensional thread index forming dimensional block of threads, called thread block. These thread blocks are distributed in SMs, so that the total number of threads is equals to the number of threads per block times the number of blocks. The number of SMs and the maximum number of threads per SM (or per block) depends on the computing capability of the graphics card. For example, GeForce RTX 2060 has 15 SMs and maximum thread per SM is 1024. The device has its own memory which could be classified as off-chip and on-chip memory. The off-chip memory is relatively slow but larger, including local, global, constant and texture memory. The on-chip memory is small but much faster, including registers, shared memory, constant cache, and texture cache. The read only constant and texture cache makes the fast access to constant and texture memory. Specially, the random access is better supported by texture memory [142].

According to the CUDA Guide, parallel optimization is based on four strategies: maximum utilization, maximum memory throughput, maximum instruction throughput and minimize memory thrashing. Applying these to our viMC code, there are some methods to improve the computational efficiency, the speedup shows in Table 4-4 and the stratagem detail follows. The flowchart of the parallel voxelized iMC simulation based on CUDA-C shows in Figure 4-16.

Table 4-4 Performance increase for each optimization methods than above (GeForce RTX 2060).

Optimization	Incremental Speedup
CPU code	NAN
Naïve CUDA version	10x
CUDA math operations and single- precision floating-point	1.8x
Sort the total free pathlength l_as	1.6x
Redefine the l_a without RN generate (RNG)	1.2x
Remove the specular reflection at the incident surface	1.4x
Optimized the photon launch logic	1.4x

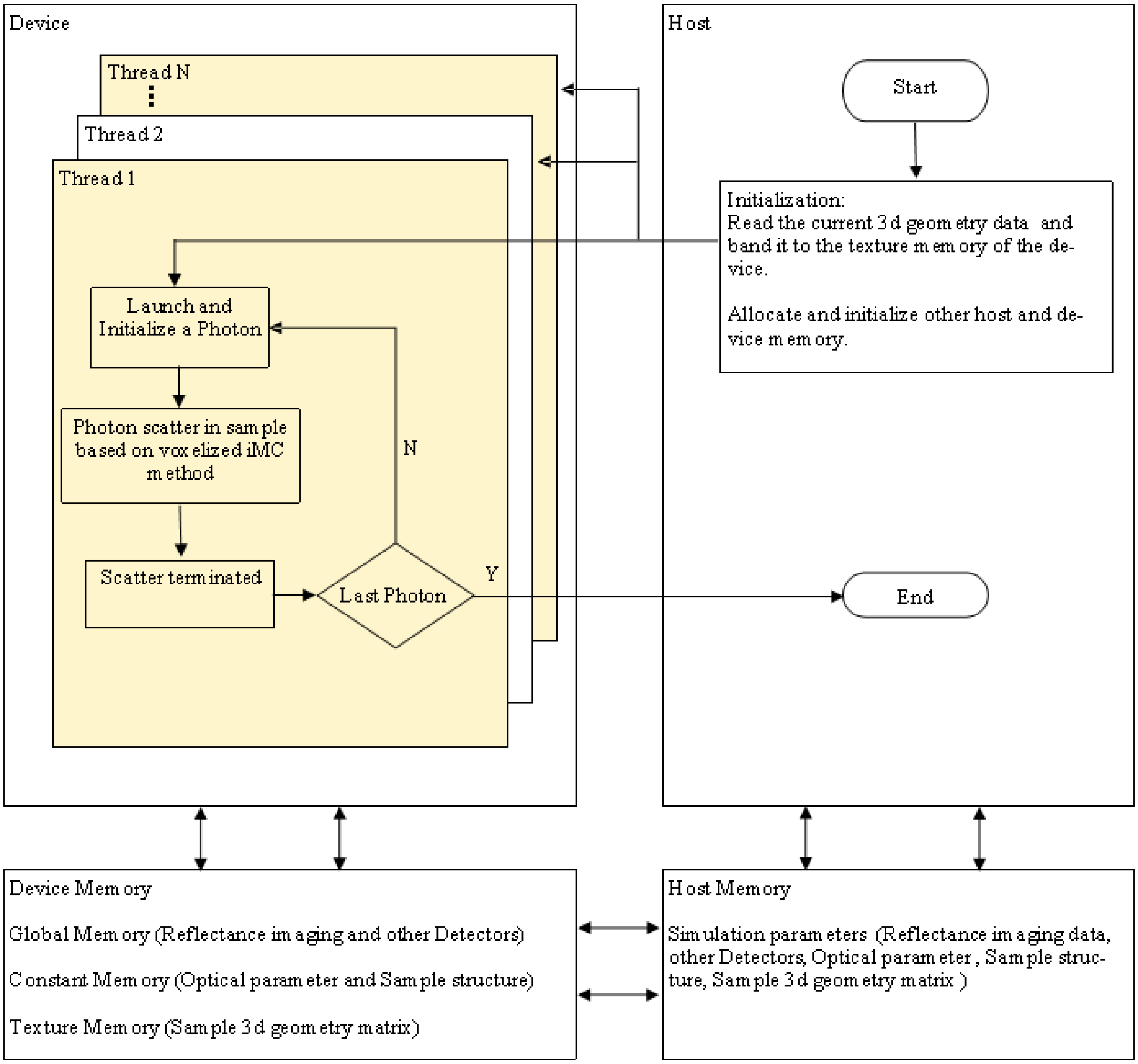

Figure 4-16 The flowchart of the parallel voxelized iMC method based on CUDA.

Naïve CUDA version:

Changing our serial programming C code to parallel CUDA-C need some steps as: find a suitable random number generation (RNG); declare variable parameters as photon location and scattering parameters, in host and device memory; declare the constant parameters used by high frequency such as sample geometry structure, sample optical parameters, in constant memory; rewrite the tracking code for per photon propagating in skin phantom to kernel functions.

According to the theory method in Chapter 3, the accuracy of MC simulation first depends on the uniformity of RND. In serial execution, people use a long period RNG to keep out of the overlap of RND sequence. But in parallel execution, we need general unrelated RND sequences for each thread by choosing property seeds. Now the function curand() from CUDA support bit generation and could be initiated by coder using seed, the numbers of sequence, and offset. It is faster than other RNG and has a long period greater than 2^{190} which is long enough for our iMC simulation. The structures are saved in global memory and global memory instructions support size is 1, 2, 4, 8, or 16 bites. To maximize memory throughput, we could align the structure to 16 bytes. Also, if the constant data is too big to store in constant memory, we can use texture memory instead. Texture memory present some benefits for the random-access or broadcast to separates variables in a single operation [142, 143].

CUDA math operations and single- precision floating-point:

The processing power of single- precision floating-point () is dozens of times as the processing power of double-precision floating-point (DPFP) in the GeForce cards of Nvidia. The series before GeForce 400 only support SPFP processing. So, we should avoid DPFP calculations to increase computing speed. SPFP standard functions defined by CUDA can be executed faster than the standard DPFP functions in chips with less accurate. Coder could apply the global command '-use-fast-math' in the compiler to replace all DPFP functions by SPFP functions. But this may affect the accuracy in our study. Hence, we optimized some functions which has better acceleration such as __fdividef(), __sinf(), __logf() in our viMC code. The speedup of this strategy is 1.8x.

Sort l_as before simulation:

If we directly simulate a batch of photons with l_a calculated by a RND, the lengths of l_as are significant different in adjacent threads. Generally, the thread which calculated shorter l_a stops tracking earlier. But it waits for the other threads in the same warp of threads for synchronization. Hence, we explored a method by sorting the l_as ascending to shorten the asynchronous time. And the strategy offers us 1.6x speedup.

Redefine l_a without RNG:

We calculate l_a with RND by Eq.(*3-62*) and we do it in our C code. But generation of RNDs cost huge computing source. In CUDA-C, we find that we can calculate the l_a at each thread based on the tracking and total numbers without RND as Eq.(*4-3*), n_{tr} is the current tracking number and N is the total tracked photons. This strategy offers 1.2x speedup.

$$l_a = -\ln(\frac{n_{tr}}{N}) \Big/ \mu_a \tag{4-3}$$

Remove the specular reflection at the incident surface:

In our simulation, the incident surface is smooth, the photon is reflected specular. Then, we could remove this step in our simulation. And it makes our code 1.4x speedup.

Optimized the photon launch logic:

Recently, we optimized the photon launch logic in our simulation. The previous one is launching a batch of photons as one per thread, after the tracking finished, then another batch. This logic introduced asynchronization during threads in each batch, even we sorted the l_as. Now, we launch the photons in each thread one by one, and close the thread when the tracking number n_{tr} equals the total photon number N. The speedup is 1.4x.

4.4 Validation by van de Hulst’s table

Van de Hulst’s table define the response to a parallel beam of radiance L_{in} at the incident angles of (θ_0, φ_0) as a bidirectional transmission function T_b and a bidirectional reflection function R_b for infinite homogeneous slab sample with parallel plane surface. Where $0\leq\theta\leq\pi$ is the angle between the z axis and the scale line formed from origin and a given point P and $0\leq \varphi\leq 2\pi$ is the angle between the positive x axis and the scale line from the origin to the point P projected onto the x-y plane, which are adopted from the spherical coordinated system.

At exit angle (θ, φ), the outgoing bidirectional transmission light are calculated as

$$L_t(\mu,\varphi) = \int_{2\pi} T_b(\mu,\varphi;\mu_0,\varphi_0) L_{in}(\mu_0,\varphi_0)\frac{\varphi_0}{\pi} d\Omega_0 = \int_0^1 T_b(\mu,\mu_0) L_{in}(\mu_0) 2\mu_0 d\mu_0 \qquad (4\text{-}4)$$

for the bidirectional transmission light and

$$L_r(\mu,\varphi) = \int_{2\pi} R_b(\mu,\varphi;\mu_0,\varphi_0) L_{in}(\mu_0,\varphi_0)\frac{\varphi_0}{\pi} d\Omega_0 = \int_0^1 R_b(\mu,\mu_0) L_{in}(\mu_0) 2\mu_0 d\mu_0 \qquad (4\text{-}5)$$

for the bidirectional reflected light, where $\mu=|\cos\theta|$, $\mu0=|\cos\theta0|$ and $d\Omega=d\mu0d\varphi0$. The function R_b and T_b defined in Eq. (*4-4*) and Eq. (*4-5*) are used in our validation of parallel viMC program with the homogeneous slab sample.

For validation purpose, in our viMC simulation, we employed a configuration of a finite slab sample, parameters show in Table 4-5, with the photons of incident beam uniformly distributed at the phantom surface with a direction of (θ_0, 0). Then choose the centering half size surface as the field of view (FOV) to couple the infinite condition in van de Hulst’ table. We calculate the angle-resolved reflectance $R_b(\theta_i, \theta_0)$ over the FOV, $\varphi \in [0, 2\pi]$, and $\theta_i \in [(i-1)\, \Delta\theta, i\, \Delta\theta]$, with $\Delta\theta= \pi/(2M)$ and i=1,2, 3, …, M. Then multiplied by $\pi/(\Delta\Omega\cos\theta)$, where $\Delta\Omega=2\pi\Delta\theta\sin\theta$ is an element of the solid angle, $\theta=(i-0.5)\, \Delta\theta$ for each θ_i. The results can be compared directly to the bidirectional reflection function in van de Hulst's table. The same procedures are also used for comparison of the bidirectional transmission function T_b. Here, T_b do not include the direct transmission photons, which has the exit angle equals incident angle.

Table 4-5 iMC simulation parameters validation by van de Hulst's table, units (mm & degree).

Sample Length	Sample Width	Sample Height	Photon number (N_0)
400	400	100	$5x10^7$
Voxel length (Δx) (mm)	Voxel width (Δy) (mm)	Voxel height (Δz) (mm)	Incident angle (θ_0) (degree)
0.1	0.1	0.001	60/0

We validated viMC CUDA program by comparison of the R_b and T_b calculated using the sample describe above with M=60 and those optical parameters in the Table 35 and Table 37 from van de Hulst's table [144]. We set the total tracking photon number $N=5x10^7$ which is large enough to decrease the statistical fluctuation introduced by MC method. The comparison results and related optical parameters are show in Figure 4-17, the symbols are the data from Tables 35 and 37 in Ref [144], lines are values obtained by viMC code and the incident beam angle of the left image is 0 degree, and the right is 60 degrees.

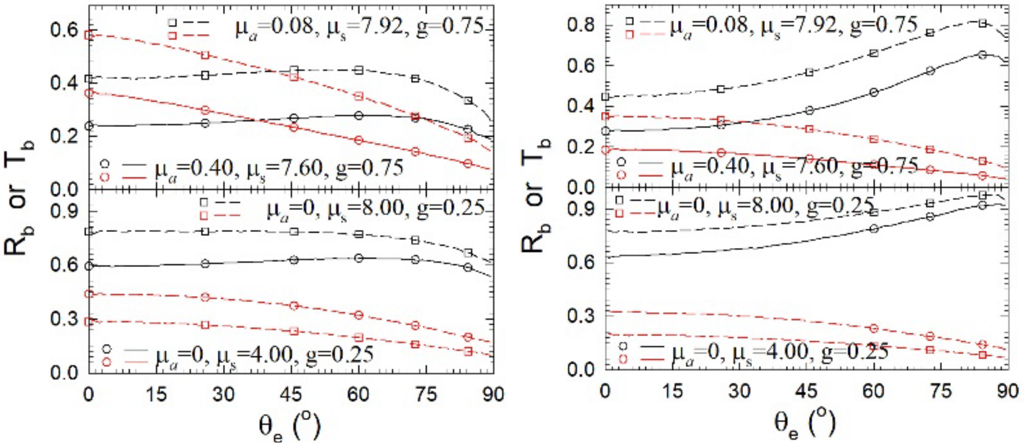

Figure 4-17 The bidirectional reflection (black) and transmission (red) functions vs the exit angle for a homogeneous slab phantom of n=1.008 with N= 5x107 for RT parameters marked. The lines are values obtained by the viMC CUDA code and symbols are those of Tables 35 and 37 in [144]. The incident beam angle of the left image is 0 degree, and the right is 60 degrees.

4.5 Modeling of iPPG process

4.5.1 Imaging by reflected light intensity with varying artery radius

To explore the influence on diffuse reflected light signal distribution by the presence of blood artery of different vessel sizes, we set the depth center axis of a radial artery at 2.5mm under the skin surface of the phantom with the radius ranging from 0.6 to 1.1mm of 0.1mm in step size. The phantom consists of two parts, dermis and whole blood, the optical parameters of dermis and whole blood are linted in Table 4-3 and the voxel number along each coordinate axis denoted as N_x, N_y, N_z is set respectively at 400, 400 and 200 with the voxel size set as 0.1mm. We first normalized the surface density reflected photons by the maximum density number to an 8-bit gray image with pixel number varied 400x400 to 100x100 as shown in Figure 4-18. We also save the maximum and minimum numbers of surface density for each simulated image. The total number of tracked photons for each iMC simulation was set to $N=5\times10^7$, and simulation time was 45s with a computer of CPU by Intel Core i7-10700F and GPU board of GeForce RTX 2060.

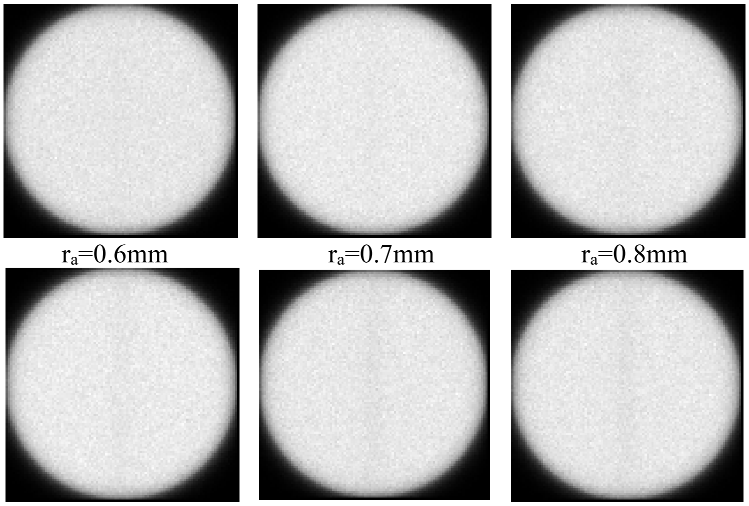

r_a=0.6mm r_a=0.7mm r_a=0.8mm

r_a=0.9mm r_a=1.0mm r_a=1.1mm

Figure 4-18 Reflection images in different artery radius with depth of artery 2.5mm. The voxel number is 400x400x200 with 0.1mm voxel size and $N=5\times10^7$. The optical parameters are listed in Table 4-3.

The reflection images in Figure 4-18 show increasing contrast in pixels on top of the artery as the artery radius increases. Further, the maximum photon density in each image with radius increasing from 0.6 to 1.1mm are given by 1640, 1615, 1630, 1610, 1630, 1613 respectively, and the minimum photon density remains 0 for each image. An area of 13x13 pixels in the center of the reflection image as ROI and Figure 4-19 present the photon density averaged over the ROI, which decreases for increasing artery radius value.

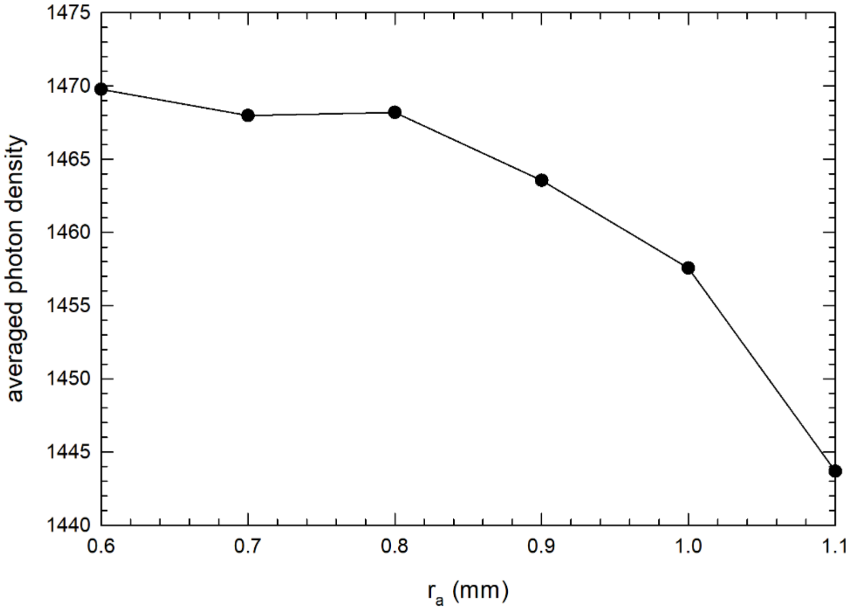

Figure 4-19 The average photon density in the central ROI of 13x13 pixel area of the 6 reflection images presented in Figure 4-18.

4.5.2 Simulations of iPPG signals by the coupled model of iMC and blood fluidic dynamics

To compare the simulation results with measured iPPG data, we configure the skin phantom as a cubic of three layers of epidermis, dermis and subcutis with radial artery embedded in the dermis and subcutis. The tissue parameters including optical and geometry parameters, have been reported by other researchers [47, 50, 51, 87, 145-151]. The parameters used in our study are presented in Table 4-6 with N_x, N_y, N_z set at 800, 800 and 800 and the voxel size at 0.01mm.

The physical sizes of the phantom correspond to 1.6x1.6x0.8 cm and the total voxel number is 2.048×10^7. The illumination light is considered as three light beams of cylindrical shape and top-hat profile with incident angle $\theta=45^\circ$, $\varphi=0^\circ$, 120°, 240° respectively with total tracking photon number $N=5 \times 10^8$. The simulation time of each reflection image is about 760 s on a new computer with CPU of Intel(R) Core (TM) i9-10859K and a GPU card of Nvidia GeForce RTX 3090. We performed simulations of 50 reflection images of 1600x1600 pixel and at different times during a cardiac cycle with values of artery radius shown in Figure 4-10. For each reflection image, we chose the central region of 400x400 pixel as the ROI on top of the embedded artery to obtain the average photon density or pixel intensity as the reflected light signal that can be measure with our iPPG system.

Table 4-6 Tissue parameters with units of mm or mm^{-1} (T=thickness, D=diameter, z_c=depth from surface).

tissue	μ_a ^{a} (mm^{-1})	μ_s ^{a} (mm^{-1})	μ_s' ^{a,b} (mm^{-1})	g ^{a}	n ^{a}	T (mm)	D (mm)	z_c (mm)
epidermis	0.03 [145], 0.12 [146]		2.17 [145], 3.52 [146]	0.6^d [146]	1.417 [147]	0.1[47]		
dermis	0.16 [50]	9.0 [50]		0.88 [50]	1.387 [147]	1.0 [47]		
subcutis	0.009 [148], 0.11 [149]		1.12 [148], 1.08 [149]	0.9^d	1.30^d	6.9		
Blood c	0.49 [51]	74.2 [51]		0.9832 [51]	1.39 [51]			
radial artery							2.0 ~4.0 [150]	3.0 [47]
artery wall	0.08 [87]	23.0 [87]		0.9 [87]	1.4 [87]	0.17 [151]		

^{a} λ=850nm; ^{b} $\mu_s' = \mu_s(1-g)$; ^{c} $SO^2 > 98\%$; ^{d} based on the water content and the value of the adjacent layer; If there are more than one value, we use the newest one as our input parameters.

The result in Figure 4-19 shows that, the photon density or pixel values of a reflection image appears sensitive to the artery radius value that is almost doubled from 0.6 to 1.1. But during cardiac cycles, the radius variation of artery radius is only about 10% according to our blood flow simulation results presented in Figure 4-10 B. Thus, the related changes of pixel intensity in a reflection image should be small compared to the inherent statistical fluctuations in MC simulations. For 13 minutes or longer to complete a single reflection image, it is time consuming if we reduce the fluctuations by increasing the total number of tracked photons in order to determine the small changes of pixel intensity. An efficient method for simulating the reflection iamge has been devised to reduce the effect of statistical fluctuation in an MC simulation by processing the calculated images using a bandpass filter processing which is similar as we did in processing the measured iPPG data as described in Chapter 5. With this method, we obtained comparable result on the relation between reflection image pixel intensity variation and changes in artery radius in a cardiac cycle. In Figure 4-20, we plot and compare the results of artery radius with the pixel intensity of calculated reflection image and the filtered intensity denoted as simulated iPPG. The blue colored data are the simulated radial artery radius by the 1D blood flow model during a cardiac cycle and the deep green colored data are the averaged reflection image intensity calculated by the iMC model while and the red colored data present the effect of filtering. It is clear from the Figure 4-20, the pressure waveform which is the same as the radius profile agrees well with that of the filtered reflection image intensity.

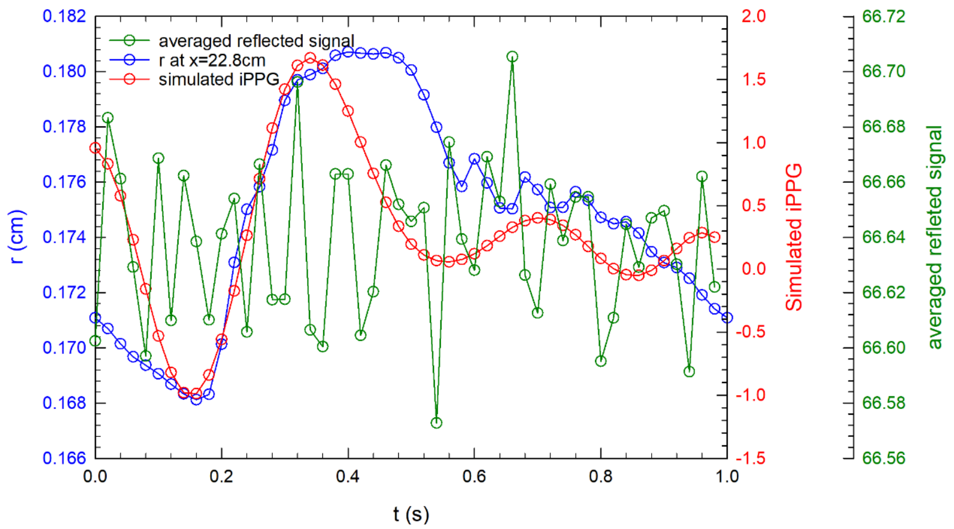

Figure 4-20 Radial artery radius and simulation result of reflection image in normal artery conditions with tracked photon number N=5x10^8. The blue colored data are the simulated radial artery radius by the 1D blood flow model during a cardiac cycle and the deep green colored data are the averaged reflection image intensity calculated by the

iMC model while and the red colored data present the effect of filtering of deep green data.In order to test the robust of this iMC simulation, we used another set of radial artery results by simulation of a ‘soft’ artery with wall parameters listed in Table 4-7. The parameters of geometry, mechanical and initial conditions of the human common carotid artery are taken from [137], and the artery wall thickness is estimated from [151]. The results of ‘soft’ artery are shown in Figure 4-21 and the definition of symbols is the same as Figure 4-20. In this case, the agreement between the simulation iPPG signal and pressure waveform becomes more skewed due to the presence of multiple peaks in the time domain which reduces the effectiveness of bandpass filtering. There are two strategies to improve the accuracy of simulation in future research. First, we will introduce elastic deformation of skin tissue with artery pulsation. Second, we can improve the computation speed by optimizing CUDA algorithms to track more photons without significantly increasing simulation time, and thus reduce the MC fluctuations. As shown in Figure 4-22, if the tracked photon number is reduced to N=5x10^7 with all other parameters kept the same as the case in Figure 4-20. The stronger fluctuations introduced more noise, thus errors in the filtered reflection image intensity.

Table 4-7 Hemodynamic properties of radial carotid artery in ‘soft’ wall conditions (CGS UNIT & SI Unit).

Property	Value
Length, L	30.089 cm
Radius at diastolic pressure, r_d	0.138 cm
Wall thickness, h	0.0138 cm
Young’s modulus, E	2.25e+6 dyne/cm^2
Mean flow rate, $\overline{Q_{in}}$	2.2 ml/s
Systolic pressure, P_s	1.67e+5 dyne/cm^2
Diastolic pressure, P_d	1.0e+5 dyne/cm^2
Windkessel resistance, R_1	11539 (dyne/cm^2) s cm^{-3}
Windkessel resistance, R_2	46155 (dyne/cm^2) s cm^{-3}
Windkessel compliance, C	4.909e-6 cm^{-3} (dyne/cm^2)$^{-1}$
Blood density, ρ	1040 kgm^{-3}
Blood viscosity, μ	4 mPa

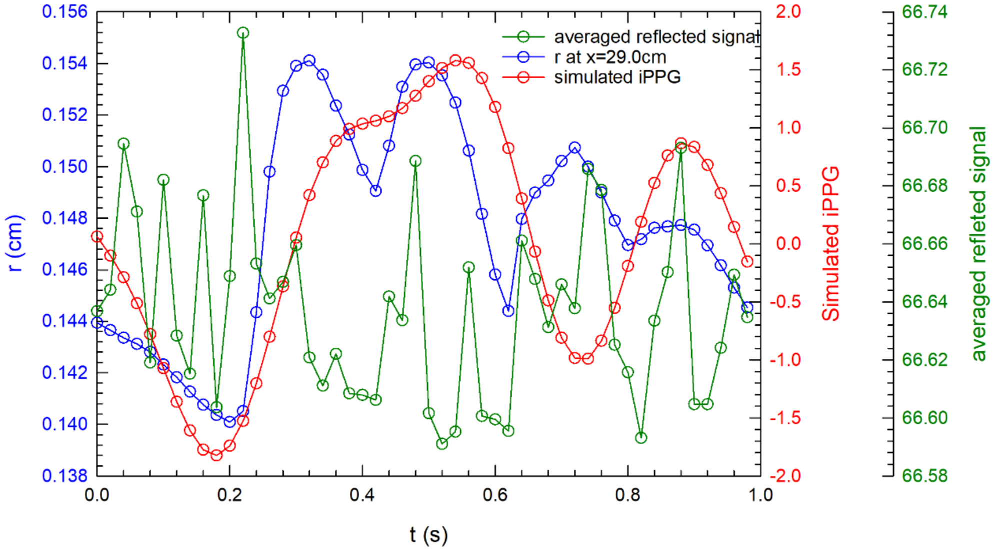

Figure 4-21 Radial artery radius and simulation result of reflection image in lower arterial stiffness conditions with tracked photon number N=5x10^{8}. The blue colored data are the simulated radial artery radius by the 1D blood flow model during a cardiac cycle and the deep green colored data are the averaged reflection image intensity calculated by the iMC model while and the red colored data present the effect of filtering of deep green data.

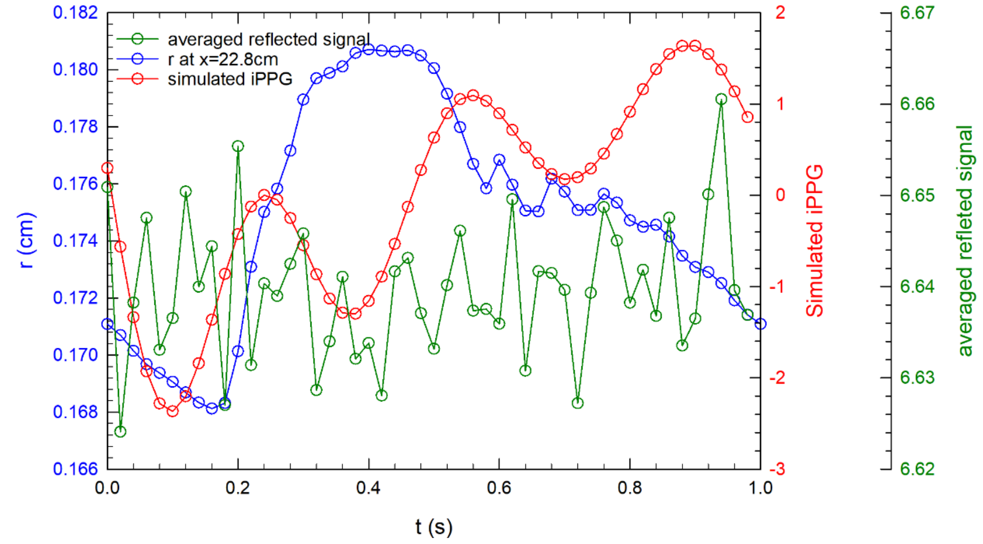

Figure 4-22 Radial artery radius and simulation result of reflection image in normal artery conditions with less tracked photon number N=5x10^{7}. The blue colored data are the simulated radial artery radius by the 1D blood flow model during a cardiac cycle and the deep green colored data are the averaged reflection image intensity calculated by the iMC model while and the red colored data present the effect of filtering of deep green data.

CHAPTER 5 EXPERIMENTAL RESULTS

In order to acquire *in vivo* iPPG data in a time sequence from hand palm, we developed a system for imaging diffusely reflected light from tissues with multiple LED illumination sources of 12 wavelength bands and cameras of frame rate up to 250 Hz. In this chapter, we present the procedures of iPPG data acquisition with the in-house developed system and related image analysis including the pulse wave index determination, the pressure waveforms comparison in multiple locations and the determination of pulse wave velocity.

5.1 Development of iPPG system

For this study, a multispectral cross-polarized imaging system has been developed for *in vivo* acquisition of time-sequenced iPPG data stacks. The system as shown in Figure 5-1 consists of three main units of illumination, imaging, and system control for image acquisition at frame rate up to 250 Hz with sequential LED illumination in 12 wavelength bands. The illumination unit contains 18 sets of LED arrays with bandwidth of 36 nm on average and peak wavelength λ_p ranging from 445 to 940 nm and polarizers. Each set includes 3 to 6 micro lensed LED arrays and the parameters of LEDs are given in Table 5-1. The arrays of each LED set are distributed evenly at three locations on an aluminum ring in a horizontal plane parallel to the target surface, and the camera sensor detect the distribution of light diffusely reflected from the illuminated target of palm. The inner diameter of the LED ring is 17.1cm and the outer diameter is 22.2cm. The DC current for each LED set is supplied a power supply and a current source circuit controlled by a potentiometer. An example of the circuit for LED array of 730nm band is shown in Figure 5-2. The vertical distance from the illumination unit to the target plane is 23cm given by h1 in Figure 5-1 as the default value which can be adjusted as needed.

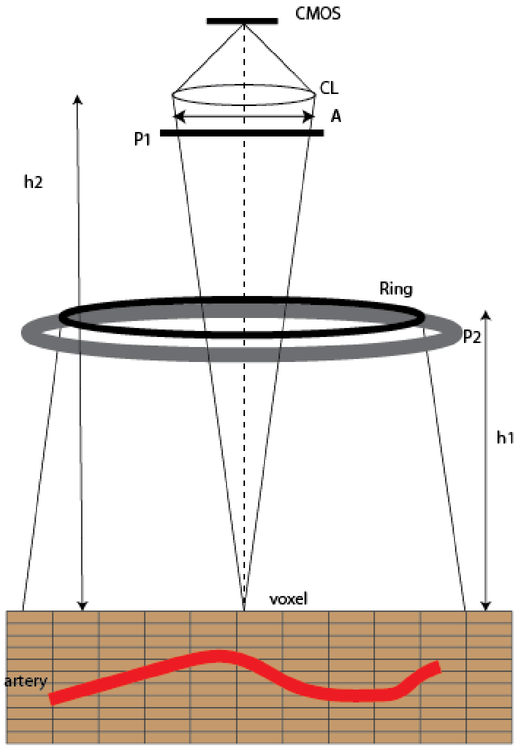

Figure 5-1 A schematic of reflectance imaging and phantom: CL: camera lens; A: lens aperture; P1: polarizer mounted on the lens; Ring: aluminum ring with LED sets; P2: polarizer sheet mounted on the illumination; h1: illumination-target distance; h2: lens-target distance.

Table 5-1 Parameters of LEDs in our study.

LED model	λ_p (nm)	$\Delta\lambda$ (nm)	Power (mw)	Current(mA)	Full angle (o)
GD CSSRM2.14-ARAT-24-1	444-457	18	1400	700	120
L1CU-CYN1000000000	504	27	200	350	140
LZ1-00G102-0000	520-530		300	1000	100
LXML-PX02-0000	566-570	110	250	350	125
LCY CLBP-KZLY-5F5G-8E8G	590	40	270	350	125
GR CS8PM1.23-JUKQ-1	634	16	520	350	80
GH CSSRM2.24-VLVN-1-1	650-666	25	1035	700	120
GF CSSPM1.24-1T3T-1-0	730	30	560	350	120
VSMY98145DS	810-820	35	1500	1000	90
SFH 4718A	850-860	30	665	1000	90
VSMF2893RGX01	870-910	40	40	100	50
SFH 4727AS A01	940-950	30	1200	1000	50

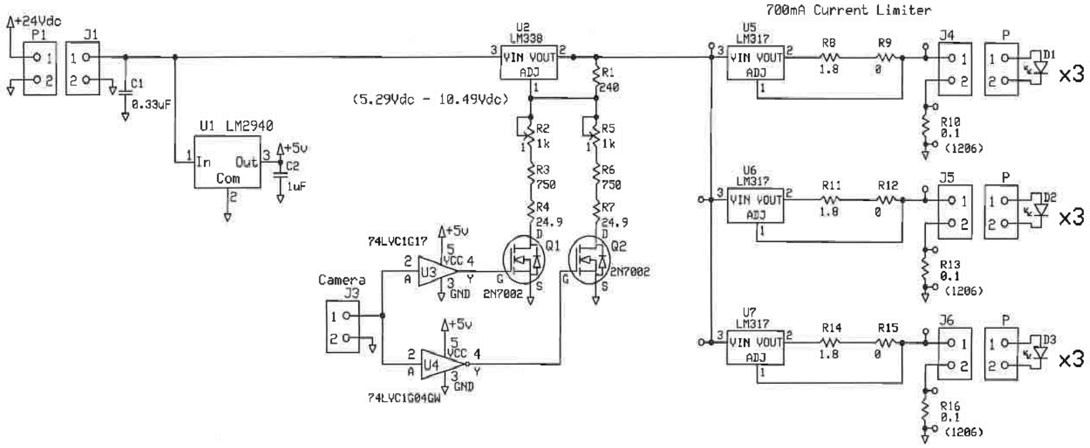

Figure 5-2 A schematic of LED power supply circuit for 730nm LEDs.

The imaging unit includes a high speed 10-GE dual-sensor CMOS camera (JAI Ltd, FS-1600D-10GE.), a camera lens and a polarizer. The CMOS camera incorporates a prism to direct visible light of wavelengths between 400 and 670 nm onto one sensor and NIR light between 740 and 1000 nm onto the other sensor, which were employed for acquisition of iPPG data at 11 wavelengths. For imaging at λ_p =710nm, a CCD camera (Lumenera Corp, Lt365RM.) was used with 640x480 pixels per image at F=109 Hz. Both cameras were set to acquire 8-bit image stacks to ensure high frame rate and the same camera lens of f=8.5 mm in focal length (#58000, Edmund Optics Inc.) was used. To reduce the effect of light backscattered from superficial skin tissue layers, linear polarizing films were placed on LED arrays and camera in cross-polarized configuration. The distance from the camera lens to the target (is h2 in Figure 5-1) is fixed at 48 cm to obtain 25cm x13cm field of view with the pixel numbers of image 1024x532. The parameters of imaging unit setting list in Table 5-2.

Table 5-2 Parameters of the imaging system.

Parameters	Pixel numbers	Pixel depth	off-set coordinates (x, y)	Frame rate, F	Frame numbers, M	Distance from object to lens	Field of view	LED optical power	Exposure time, τ	Gain
settings	1024x532	8-bit	(216, 278)	250	2500	48cm	25x13cm	Depends on λ	Depends on λ	Depends on λ

The system control unit has been developed based on the eBUS SDK (Pleora Technologies Inc.) provided by the camera vendor within the Microsoft Foundation Classes (MFC) framework with the user interface shown in Figure 5-3. It contains a part of parameter setting including image resolution, image off-set along width and height for ROI processing, frame rate, exposure time for two sensors, and electronic gain for output current signals of the two sensors or together. The software has an intensity control function by calculating the maximum intensity per frame and display in time as ‘Pixle_max’ control box in the user interface to prevent pixel saturation in image acquisition. The preview window displays the acquired images from four channels of R, G, B for the visible sensor and NIR for the NIR sensor. Before capturing images, one can use the preview windows to focus the object plane on the target plane. The exposure time τ and gain of camera were adjusted individually to achieve high pixel values below saturation. To maximize the frame rate, only one channel is selected for saving monochromatic image stack through the channel selection control box labeled ‘SaveChannel’. Each image stack captures a total of M images and is transmitted to a host computer by an ethernet or USB 3.0 cable and saved in tiff format. Since the CMOS camera cannot sense the wavelength band around 700nm, another CCD camera was used to acquired iPPG stacks with illumination of 730nm in wavelength band.

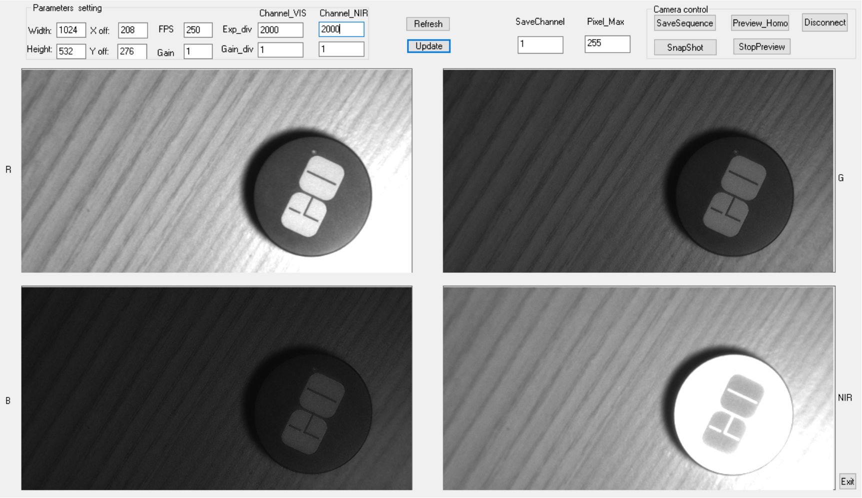

Parameters setting

					Channel_VIS	Channel_NIR
Width: 1024	X off: 208	FPS	250	Exp_div	2000	2000
Height: 532	Y off: 276	Gain	1	Gain_div	1	1

SaveChannel: 1
Pixel_Max: 255

Figure 5-3 User interface of the in-house developed camera control software.

5.2 Acquisition and ICA processing of *in vivo* iPPG stack at 12 wavelength bands

We have performed multiple imaging acquisitions with the iPPG system on the left hands of two healthy volunteers including the author of this dissertation who have no history of cardiovascular diseases and hypertension. At each of the 12 illumination wavelength bands, an iPPG stack was acquired at a frame rate of F = 250 Hz with total number of images given by M = 2500 so that the acquisition time $t = i/F$ with $i \in [1, M]$ for each image of 1024x532 pixels.

Each imaging session took 10s to complete with the room light off. Each volunteer needed only to keep his left-hand stationary for imaging the palm side under normal breathing condition and stack processing required no image alignment. The volunteer wore a pulse oximeter on a finger of right-hand during imaging for simultaneous recording of heartbeat rate as ground truth to validate f_h determined from the acquired iPPG stack and blood oxygenation to ensure healthy status. For all iPPG measurements, the blood oxygenation values of both volunteers were found to be within a normal range of 96% to 98%.

After segmentation, all pixels in the hand region were pooled together to determine the averaged and mean-centered normalized intensity $I_{na}(t; \lambda_p)$ followed by calculation of the heartbeat rate f_h as shown in Figure 5-4 A and Figure 5-4 B from $i_{na}(f, \lambda_p)$ as the Fourier transform of $\mathbf{I_{na}}$. The rate f_h was validated against the value measured by the pulse oximeter and the acquired stack was discarded if the two values of f_h differ by more than 10%, which occurred rarely and was due to hand motion.

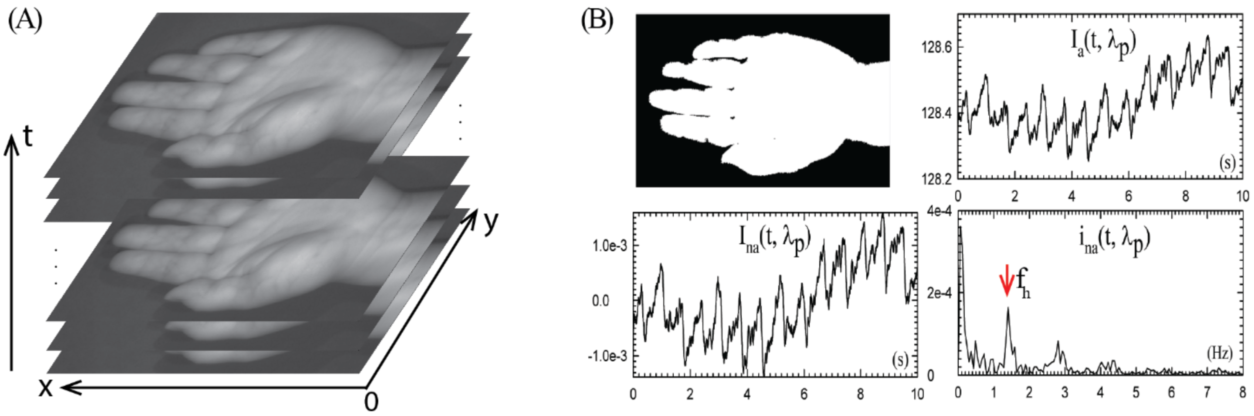

Figure 5-4 (A) An iPPG image stack. (B) An example of segmented image, time plots of averaged pixel intensity $I_a(t, \lambda_p)$ over hand region, normalized intensity $I_{na}(t, \lambda_p)$ and its Fourier transform $i_{na}(f, \lambda_p)$ with heartbeat rate f_h marked.

The pICA algorithm was then applied with the scheme of single-pixel POI to each pixel in the hand region to obtain corresponding the cardiac component $S_c(x, y; t; \lambda p)$ by the work-flow shown in Figure 5-5 A. The PPG signal $S_{cf}(x, y; t; \lambda p)$ was obtained by the finite impulse response (FIR) filtering of $S_c(x, y; t; \lambda_p)$. We further developed two schemes of localized pixel averaging to obtain the 3-time vectors as the input signals. In the first scheme, a POI in the hand region is selected to be the first input vector $I_{n1}(x, y; \lambda_p)$ and the two other vectors are formed by the averaged intensities of pixels neighboring the POI. The vector $\mathbf{I}_{n2}$ was obtained as intensity averaged over 24 first nearest-neighbor pixels (FNPs) in the two rings surrounding POI whereas $\mathbf{I}_{n3}$ as that over 24 second nearest-neighbor pixels (SNPs) in the third ring surrounding the POI as shown in Figure 5-5 B. For comparison, we have also performed pICA on iPPG stacks with $\mathbf{I}_{n2}$ and $\mathbf{I}_{n3}$ given by intensities averaged over non-local pixels in the two regions of half-hand which was found to yield significantly reduced image contrast in synthesized maps of the PPG signals against palmar artery anatomy. The definitions of single-pixel POI, FNPs and SNPs as input signals to pICA is termed as the PFS scheme in this study, which is used for determination of spatial distributions of PPG signals related to PPW.

The second scheme of localized pixel averaging is to increase pixel numbers for further improvement of SNR in the cardiac component produced by pICA. The first-time vector I_{n1} is defined as the averaged intensity of 81 pixels over a square zone of 9x9 pixels centered on a selected POI while I_{n2} is over 40 pixels as the fifth nearest-neighbors (fNPs) and I_{n3} over 48 pixels as the sixth nearest-neighbors (sNPs). The definitions of input signals with zone-averaged POI are termed as the Pfs scheme and used in analysis of blood pulse waveforms.

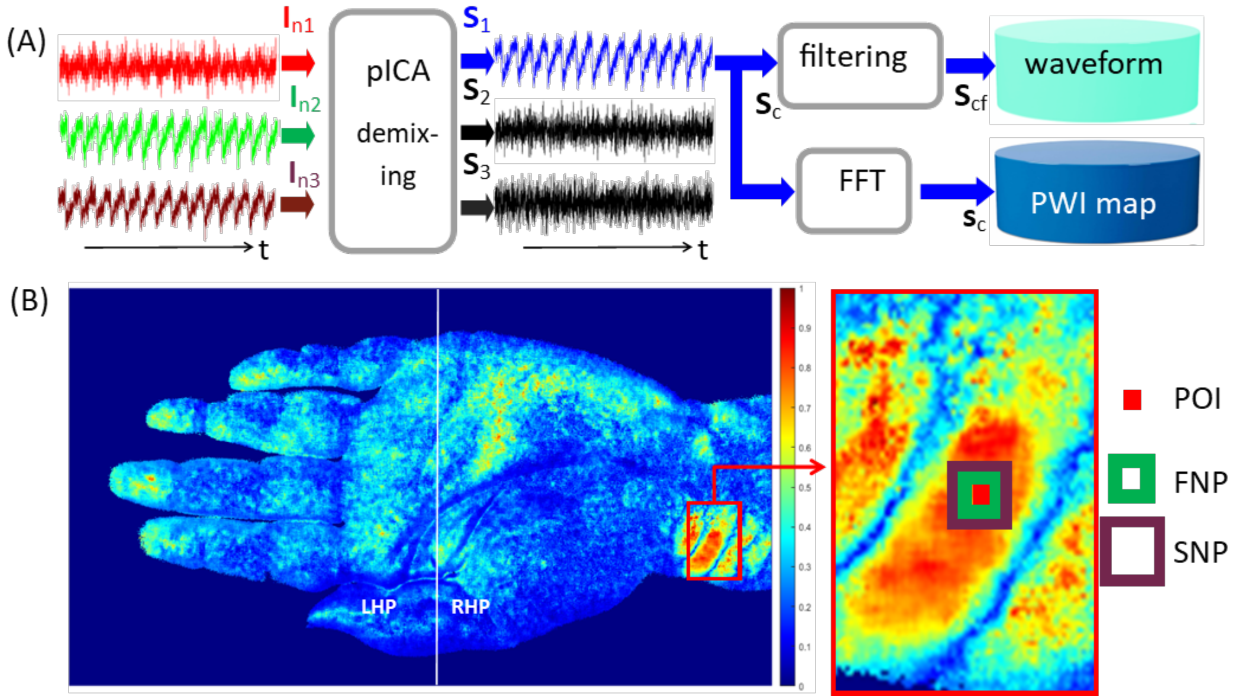

Figure 5-5 (A) Workflow for extracting PPG waveform and PWI map. (B) A false-color PWI map (left) of volunteer #1 with $\lambda_p = 850$ nm to illustrate two choices of I_{n2} and I_{n3} as input signals for PFS scheme of single-pixel POI: with FNP and SNP in magnified view (right) and with LHP and RHP in half-hand regions separated by white line (left).

In additional to the validation of f_h determined with an iPPG stack by the heartbeat rate measured with pulse oximeter, we further performed simultaneous measurement of the electrocardiogram (ECG) data with iPPG imaging at $\lambda_p = 850$ nm for this study. An ECG detector was built with a dedicated ECG signal conditioning chip (AD8232, Analog Devices, Inc.) to sample signals from three electrodes placed on chest of each volunteer at a rate of 8 kHz.

The description of the circuit and code of ECG technology is provided in Appendix C. The ECG signals are plotted together with $\mathbf{S_{cf}}$ as PINK lines in the right columns in Figure 5-6 to demonstrate unambiguously the synchronization between the cardiac component $\mathbf{S_c}$ or PPG signal $\mathbf{S_{cf}}$ and the ECG signal. Except the cardiac component S_c, there are another two uncertainty sources we assumed. We had tested the 2 or 3 sources scenarios; the results are almost the same. So, we chose 3 as an efficiently number. In Figure 5-6 we compared two definitions of the time vectors of I_{n2} and I_{n3} as input signals to pICA in addition to I_{n1} for POI and corresponding output ICs of $S_1(=S_c)$, S_2 and S_3 and filtered ICs of $S_{1f}(=S_{cf})$, S_{2f} and S_{3f} in time domain with λp = 850 nm.

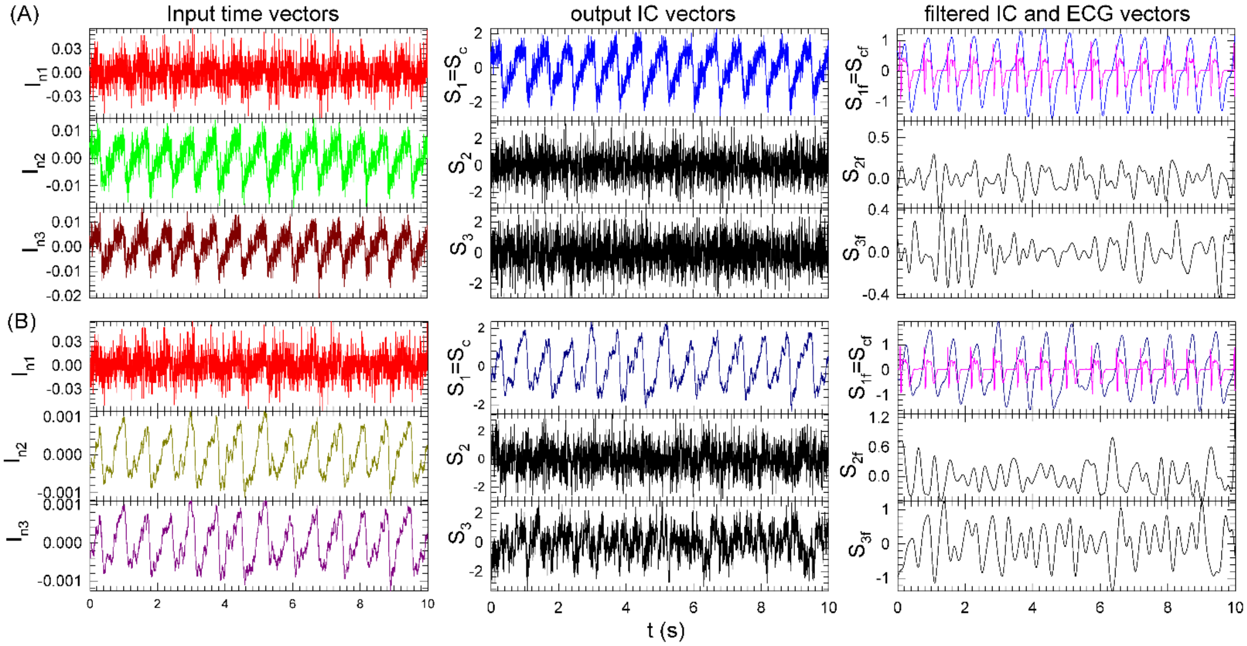

Figure 5-6 Comparison of two definitions of the time vectors of I_{n2} and I_{n3} as input signals to pICA in addition to I_{n1} for POI and corresponding output ICs of $S_1(=S_c)$, S_2 and S_3 and filtered ICs of $S_{1f}(=S_{cf})$, S_{2f} and S_{3f} in time domain with λ_p = 850 nm. (A) I_{n2} and I_{n3} are given by the average pixel intensity of FNP and SNP. (B) I_{n2} and I_{n3} are given by those of LHP and RHP. The PINK lines in the right columns represent the simultaneously acquired ECG signals.

5.3 Determination of pulse wave index to quantify spatial distribution of PPG signals

After pICA calculations, the first IC time vector $\mathbf{S}_1$ is initially set as the cardiac component since it has the largest eigenvalue or strongest temporal correlations among the three ICs. A test is carried out by Fourier transforming $\mathbf{S}_1$ into frequency domain as $\mathbf{s}_1$ to determine a maximum peak frequency f_m within the band Δf_{hb}. The vector $S_1(x, y; \lambda_p)$ is designated as $S_c(x, y; \lambda_p)$ if f_m differs from f_h by less than 10% of f_h. Failure of the test leads to re-assigning and frequency testing of $\mathbf{S}_2$ or $\mathbf{S}_3$ as $\mathbf{S}_c$. If none of ICs passes the test then the vector $\mathbf{S}_k$ with f_m closest to f_h is designated as $\mathbf{S}_c$, which occurs for pixels away from artery. The component $S_c(x, y; \lambda_p)$ is filtered into $S_{cf}(x, y; \lambda_p)$ by a zero-phase filter based on the FIR algorithm to remove frequency components outside the band Δf_{hb}. The FIR filter is chosen for its ability to produce no phase-shift between $\mathbf{S}_c$ and $\mathbf{S}_{cf}$, which enables comparison of time delays in $S_{cf}(x, y; \lambda_p)$ as the PPG signal related to PPW among multiple locations [152].

The PPG signal of $S_{cf}(x, y; t; \lambda_p)$ is used to quantify phase delay and other parameters of PPW at (x, y) as the POI. We further define a pulse wave index (PWI) $r_{cf}(x, y; \lambda_p)$ as the ratio of frequency component sums between the PPG signals in a narrow band centered at f_m and the noise background in a wide band to indicate the pulse signal strength, which can be written as

$$r_{cf}(x,y;\lambda_p) = \frac{\sum_{j=-N}^{N} \mathrm{s}_{\mathrm{cf}}(x,y;f_m + j\Delta f;\lambda_p)}{\sum_{j=-W}^{W} s_{cf}(x,y;f_m + j\Delta f;\lambda_p) - \sum_{j=-N}^{N} \mathrm{s}_{\mathrm{cf}}(x,y;f_m + j\Delta f;\lambda_p)}, \tag{5-1}$$

where $s_{cf}(x, y; f; \lambda_p)$ is the Fourier transform of $S_{cf}(x, y; t; \lambda_p)$, $\Delta f = F/M$ is the frequency stepsize with F as the frame rate of camera and M as total number of images in a stack, 2N and 2W = 12N is respectively the total number of frequency components in the narrow and wide band. For results resented in this report, we set N=3. The PWI value quantifies the strength of the PPG signal related to PPW relative to the background noise and thus can serve as the SNR of $\mathbf{S_{cf}}$. The spatial distribution of $r_{cf}(x, y; \lambda_p)$ is employed here to synthesize PWI map with the same resolution as the iPPG data with the PFS scheme for the input vectors of pICA. We also extend the use of PWI as SNR for the input signal of POI to pICA to evaluate the SNR gain defined as

$$g_{SNR} = \frac{SNR_S}{SNR_I} = \frac{r_{cf}(x, y; \lambda_p)}{r_I(x, y; \lambda_p)}, \tag{5-2}$$

where $SNR_I = r_I(x, y; \lambda_p)$ is given by the same definition of PWI in (*5-1*) except that $s_{cf}(x, y; f; \lambda_p)$ is substituted by $i_{n1}(x, y; f; \lambda_p)$ as the Fourier transform of $I_{n1}(x, y; t; \lambda_p)$ for either scheme of the first time vector of input signals to pICA.

To improved image contrast of the synthesized PWI maps by $r_{cf}(x, y; \lambda_p)$, we have compared two approaches of forming the two reference input signals of $\mathbf{I_{n2}}$ and $\mathbf{I_{n3}}$ in additional to $\mathbf{I_{n1}}$ by a single-pixel POI in the PFS scheme. Other than using FNP and SNP, we selected the averaged intensity over left half-hand pixels (LHP) and right half-hand pixels (RHP) as $\mathbf{I_{n2}}$ and $\mathbf{I_{n3}}$ that are non-local to POI. Figure 5-5 B illustrates the two choices of $\mathbf{I_{n2}}$ and $\mathbf{I_{n3}}$ on a PWI map. The input and output time vectors for the two approaches are compared in Figure 5-6, which shows that the second choice reduces image contrast in a PWI map. The contrast reduction is due to the dominance of $S_{cf}(x, y; t; \lambda_p)$ by the much smoother input vectors of the LHP and RHP with pixel numbers much larger than those of FNP and SNP vectors. The following results were obtained with the input vectors to pICA given by the time vectors of POI, FNP and SNP in the PFS scheme.

Twelve monochromatic iPPG stacks have been acquired sequentially from the two volunteers with the peak wavelength λ_p of LED illumination ranging from 445 to 940 nm in a cross-polarization configuration. While cross-polarization between LED illumination and iPPG imaging provides moderate improvement in image contrast of PWI maps, it requires large LED irradiance to ensure sufficiently SNRs of the acquired data. The micro lenses used in this study make large diverging angles, 50° to 120°, for the LED beams to achieve nearly uniform illumination on target at the expense of considerably reduced irradiance. The reduction was particularly severe at the two bands of λ_p = 890 and 940 nm because of low transmission of the polarizing films. Consequently, the PWI maps presented in Figure 5-7 are based on cross-polarized iPPG stacks acquired at all wavelengths except the above two bands as labeled. The iPPG stack for the PWI map in band of 730 nm is acquired by the CCD camera, others are the CMOS camera.

(A)

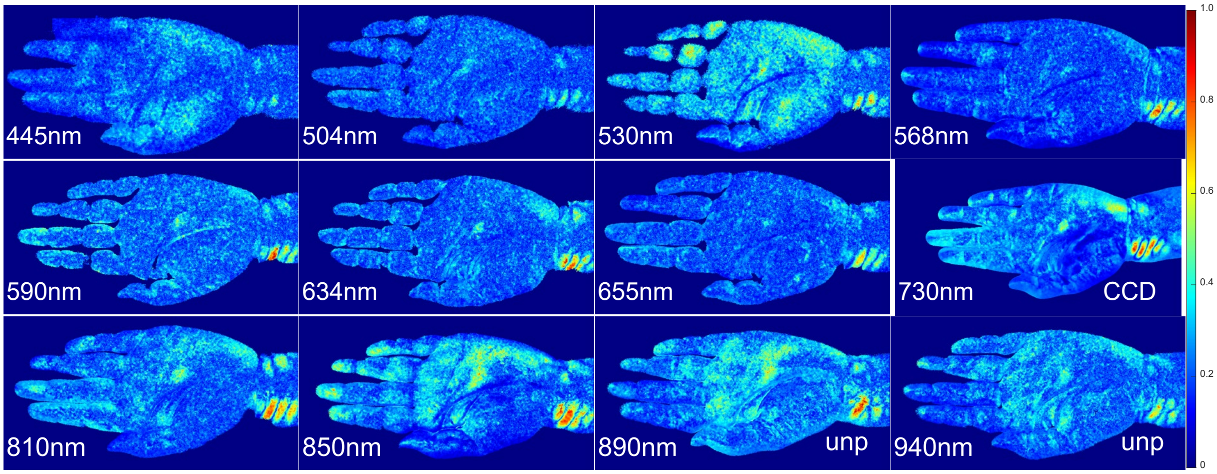

(B)

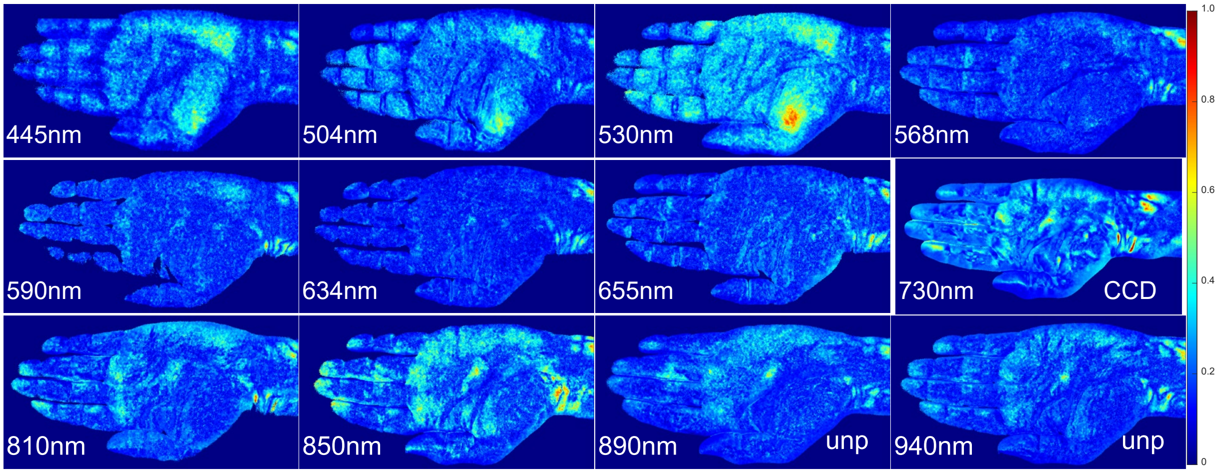

Figure 5-7 The palmar maps of normalized PWI values for each volunteer as marked on color bars and peak wavelength λp on bottom of each map: (A) volunteer #1 and (B) volunteer #2. The iPPG imaging was performed in cross-polarized configuration except two bands of λp=890 and 940nm with unpolarized illumination and imaging and 730nm with a CCD camera as marked.

In Figure 5-7, we present the PWI maps with values of $r_{cf}(x, y; \lambda_p)$ normalized over all bands for each of the two volunteer to compare the effect of wavelength on the PWI value and image contrast. Considerable similarity can be observed between distributions of pixels with high PWI values between the two bands of $\lambda_p = 810$ and 850 nm and against artery anatomy such as palmar arch, radial and ulnar artery [153]. Compared to the near-infrared (NIR) group of $\lambda_p \geq 810$ nm, the visible group of $\lambda_p \leq 700$ nm present significantly smaller image contrasts and number of pixels with high PWI values. The maps of $\lambda_p = 530$ nm exhibit the largest number of pixels with high PWI values in the visible groups for both volunteers. Still, distributions of these pixels show less similarity to artery anatomy in comparison to those of $\lambda_p = 810$ and 850 nm in the NIR group, and instead appear more related to the capillaries by the much-reduced PPW amplitudes and diffused pixel clusters. Previous studies have demonstrated weak dependence of absorption coefficient μ_a on wavelength for bloodless skin dermis surrounding the blood vessels but significant drop in scattering coefficient μ_s for increasing wavelength from 400 to 1000 nm [50]. Hence, the difference in image contrast of PWI maps between visible and NIR groups may be attributed to the increased penetration depth of NIR light to sense palmar artery and be backscattered into air.

5.4 Comparison of waveforms in multiple location of hand artery at different wavelengths

With the PWI maps shown in above, one can identify wavelength bands for high image contrasts and select POI sites of strong PWI values to compare PPG waveforms related to PPW.

To enhance SNRs, we applied the Pfs scheme with zone-averaged POI for waveform calculations. Figure 5-8 compares the waveform data extracted by the two schemes at 4 POI sites in the wrist region of volunteer #1 with strong PPG signals in two bands of λ_p = 530 and 850 nm. The gain of SNR, $g_{SNR} = r_{cf}/r_{n1}$, can be obtained with (*5-2*) and was found to increase from 3.93 by the PFS scheme of single-pixel POIs to 4.31 by the Pfs scheme. It is clear that the Pfs scheme allows SNR improvement with modest decrease of spatial resolution and was adopted for determination of waveforms discussed below.

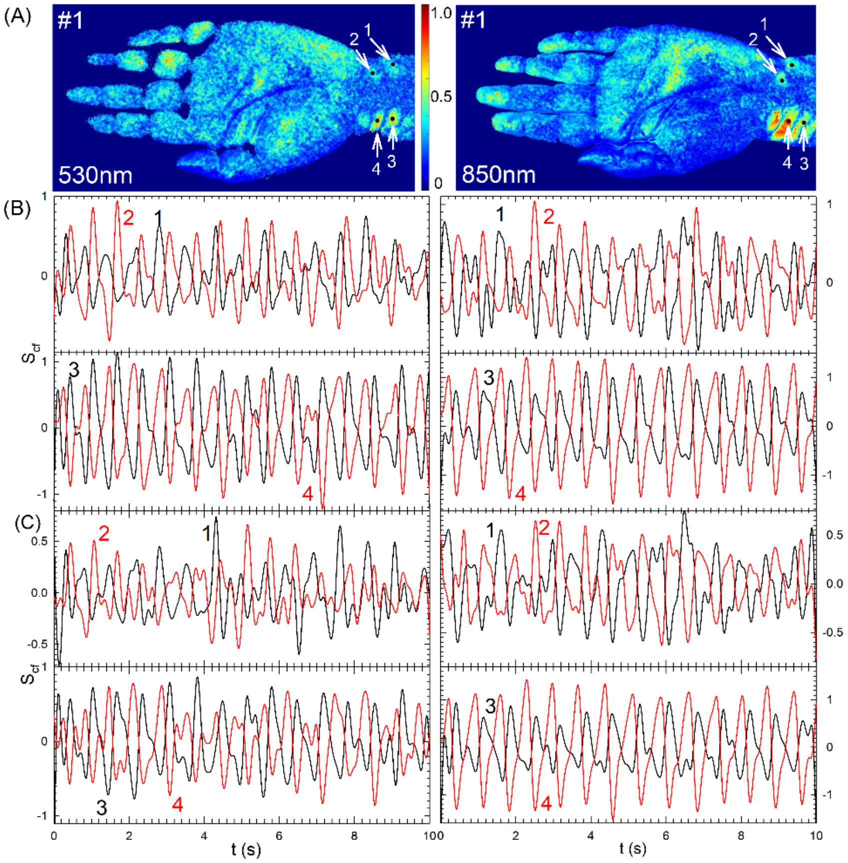

Figure 5-8 The PPW waveforms at multiple locations of volunteer #1 in two wavelength bands of λp=530nm (left column) and 850nm (right column): (A) maps of PWI values normalized by the same color bar and pixel sites marked by black dots and numbers; (B) waveforms with Pfs scheme of zone-averaged POIs ; (C) waveforms with PFS scheme of single-pixel POIs.

In addition, we show in Figure 5-9 the PWI maps of the two volunteers to demonstrate that the PPG waveforms can be extracted by the Pfs scheme of zone-averaged POIs even in the case of relatively weak PPG signals with $\lambda_p = 445$ nm. Twelve sites were selected from each volunteer's map along a path based on the anatomy of palmar arch, radial and ulnar artery. Despite the relatively large noise, the waveforms show clearly cardiac cycles driving PPW which are evidently distinguishable between the two volunteers and useful for health monitoring, biometric identification and diagnosis of diseases at this and other wavelengths. For example, the waveforms of volunteer #1 present higher values of $r_{cf}(x, y; \lambda_p)$ at the sites of 11 and 12 near the radial artery of the wrist than those of 1 and 2 near the ulnar artery side. The relation reverses for the volunteer #2 which can also be seen in the PWI maps obtained at other visible wavelengths between the two volunteers.

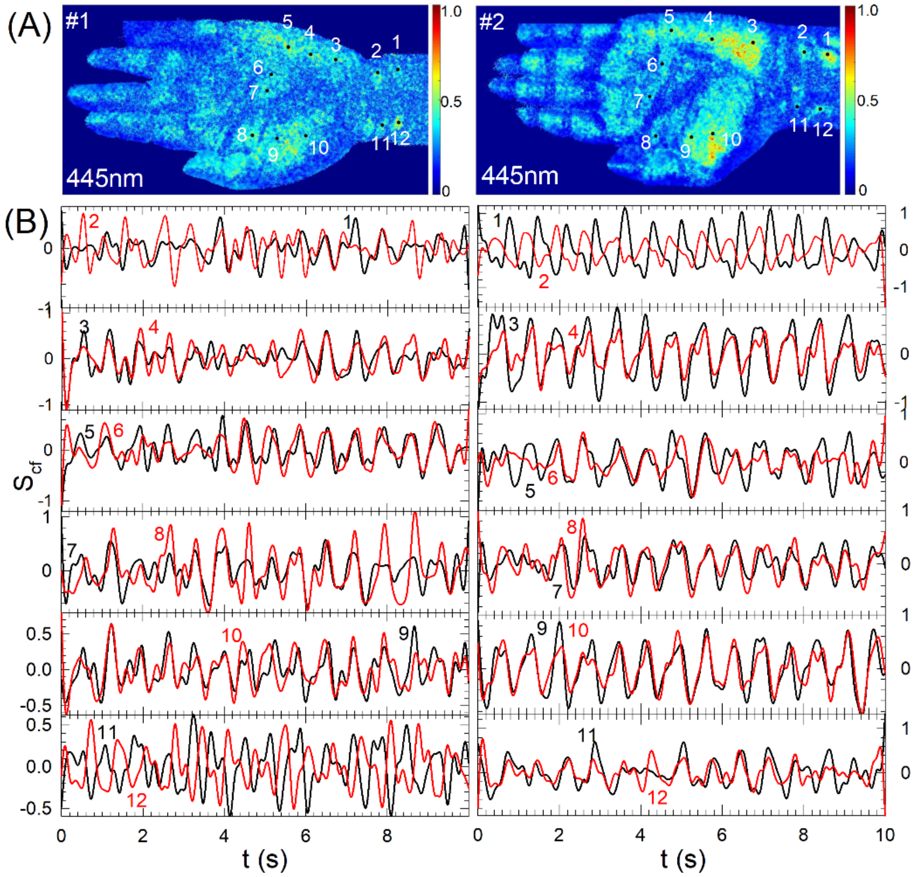

Figure 5-9 The PPG waveforms of volunteers #1 (left column) and #2 (right column) of λp=445nm at 12 POI sites: (A) PWI maps with sites marked by black dots and site numbers; (B) waveforms with Pfs scheme of zone-averaged POIs.

Comparing the PPG waveforms in Figure 5-8 and Figure 5-9, one can clearly see different phase relations for certain POI sites in the wrist from other hand regions, and these relations are similar for the waveforms in all three bands shown here and other bands (not shown) as well. For POI sites outside the wrist region from 3 to 10 in Figure 5-9, the PPG waveforms show nearly in-phase oscillations or little phase shifts within a cardiac cycle. In contrary, certain POI sites in the wrist region exhibit out-of-phase (OOP) relations in their peak-foot positions of the waveforms which can be observed in both figures. The interesting relation observed in this study has also been reported by others as well [129]. To understand the phase relations between the measured PPG waveform and that of PPW in palmar artery, we shall compare the waveforms of neighboring POI sites in 3 hand regions of strong PPW signals.

5.5 Determination of pulse wave velocity

The light measured by an iPPG camera is backscattered by artery containing tissues as a result of light absorption and scattering. Consequently, the extracted PPG signals in the form of $S_{cf}(x, y; t; \lambda_p)$ are affected by two types of processes. The first type includes the time-varying ones such as morphologic variations of artery and surrounding tissue layers due to the pulsatile PPW in artery. The second type consists of those related to the band of light wavelengths that determine the optical parameters of blood and tissues and thus the volume of tissues including artery interrogated by light. The two types of processes are obviously intertwined to alter the spatiotemporal distributions of extracted PPG signals in different wavelength bands. We also note that previous *in vivo* measurements indicated speeds of PPW propagation in human artery on the scales of 1 to 10 m/s [154]. One thus expects very small delay time among the waveforms extracted at different POI sites in a hand.

Guided by PWI map, we selected 12 or 13 POI sites near palmar artery of large r_{cf} values to analyze the phase relations of PPG waveforms in 3 regions of wrist, mid-palm and fingertip from the iPPG stack of volunteer #1 acquired at $\lambda_p = 850$ nm. Figure 5-10 A presents the waveforms, and the sites are marked by black dots and numbered on PWI map (top-right of Figure 5-10 A) and in waveforms. The red arrow in the last cardiogram (bottom-right of Figure 5-10 A) indicates a "foot" position of the waveforms before the systolic peak for calculation of time delay between sites in different region groups on inverted vertical axis. One can clearly see that the 4 sites near the radial artery show the OOP relations between the pair of sites 1 and 3 versus sites 2 and 4. In contrast, all sites in each of the mid-palm and finger regions exhibit overlapping or in-phase waveforms. It is clear that the OOP relations are not due to phase shifts of PPW which is supported by observations of in-phase PPG waveforms among POI sites outside the wrist region in other wavelength bands. Figure 5-10 B presents the waveforms and one can find that the 5 sites across the radial artery show the OOP relations is only along the radial artery at the wrist region.

For artery blood with red blood cells of nearly 100% oxyhemoglobins, the absorption coefficient μ_a oscillates across 3 orders of magnitude between 400 and 1000 nm in wavelength with maximum at the short end and minimum around 700 nm [51]. In comparison, the scattering coefficient μ_s of bloodless skin tissues and blood vary slowly while the anisotropy factor g increase from 0.4 to 0.8 for bloodless tissues and from around 0.7 to above 0.9 for wavelength increasing from 400 to 1000 nm [50, 51]. The differences in the values of these parameters of between artery blood and surrounding tissue and in their wavelength, dependences influence the volume of artery vessels probed by and image contrast of PWI maps. But these differences should not lead to OOP relations in PPG waveforms, which agree with our results shown in above three figures. For visible bands, the large μ_a values of blood limit the volume of interrogated artery vessels but the backscattering light for iPPG imaging may be enhanced by the small values of g for the surrounding tissues. Consequently, pixels of strong PPW signals can be observed in PWI maps in both groups of visible and NIR bands but the latter contains those of high image contrasts (see Figure 5-7) as the result of deeper penetration of light.

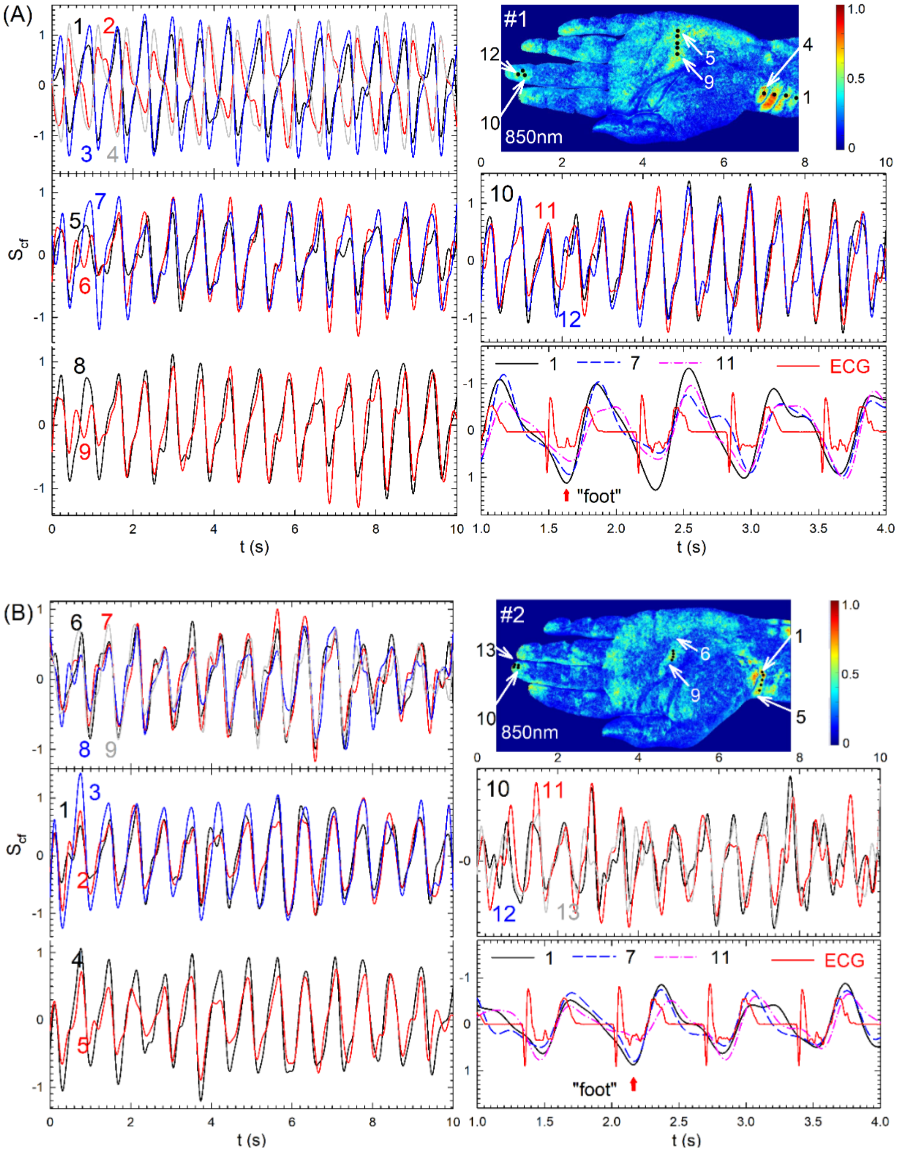

Figure 5-10 The PPG waveforms (A) from volunteer #1 at 12 POI sites and (B) from volunteer #2 at 13 POI sites, grouped in three regions of wrist (top-left), mid-palm (bottom-left) and fingertip (middle-right) at λp=850nm. The sites are marked by black dots and numbered on PWI map (top-right) and in waveforms. The red arrow in the last cardiogram (bottom-right) indicates a "foot" position of the waveforms before the systolic peak for calculation of time delay between sites in different region groups on inverted vertical axis.

The OOP relations of PPG waveforms among neighboring POI sites in the wrist region exist in wavelength bands from 445 to 850 nm as shown in above three figures. The phenomenon thus has little to do with the variation in volume of interrogated artery vessels as discussed above. Rather, one would expect the morphologic changes in tissues containing artery tree by the pulsatile blood pressure waves. It is very reasonable to consider the possibility of skin surface vibration in the wrist region as the cause of OOP relations in the wrist region since either radial or ulnar artery is of large sizes and superficial. In fact, a careful observer can actually see by naked eyes the surface vibration in wrist region which is also the sites for palpation of PPW. For other regions of the hand, the surfaces vibration appears negligible due to either large depth of artery vessels like subpapillary and cutaneous plexus from the surface in the case of mid-palm or small volume changes of arterioles in the case of fingertip.

Based on these observations, we selected the site 1 in the wrist region having the same peak-foot phase relation with sites in the other two regions and plot their PPG waveforms in the bottom-right diagram of Figure 5-10 A on an expanded time scale. These data are displayed on an inverted vertical axis to show the waveforms similar to the “conventional” presentation of PPW waveforms by electric and optical signals [155]. The peaks of the $S_{cf}(x, y; t; \lambda_p)$ curves on the inverted vertical scale are deemed as the result of peak systolic blood pressure followed by the dicrotic notch and diastolic peaks appearing in the diagram as shoulders. The simultaneously recorded ECG signal is included in the same plot of Figure 5-10 A and B that can serve as the clock pulse train for comparison of the time delays among POI sites in three regions.

Table 5-3 Distances, PTT and PWV between two hand regions[a].

Volunteer	Wrist to Mid-Palm			Wrist to Fingertip			Mid-palm to Fingertip		
	d (mm)	$\Delta t_{a,m}\pm\Delta t_{a,s}$ (ms)	v (m/s)	d (mm)	$\Delta t_{a,m}\pm\Delta t_{a,s}$ (ms)	v (m/s)	d (mm)	$\Delta t_{a,m}\pm\Delta t_{a,s}$ (ms)	v (m/s)
#1	93.4	13.3 ± 14	7.0	204	28.2 ± 17	7.2	124	14.9 ± 20	8
#2	95.6	8.09 ± 37	9.4	200	17.0 ± 26.9	11.8	127.8	8.9 ± 44.3	14.3

[a] PWV is defined as $v=d/\Delta t_{a,m}$ between two selected regions with $\Delta t_{a,m}$ as mean value of PTT.

Each waveform has 14 peaks or "feet" in different cardiac cycles on the inverted S_{cf} axis as shown in Figure 5-10. To obtain the mean and standard deviation values of foot-foot time delays on the inverted axis, we determined $t_a(w; z)$ as the time of each foot w averaged over selected POI sites in a region z. The sites include 1 and 3 in the wrist region and all sites in the mid-palm or fingertip region as shown in the PWI map in Figure 5-10 A and all the 13 sites in Figure 5-10 B. Then we define PTT as the time delay given by $\Delta t_a(z, z'; w) = t_a(z; w) - t_a(z'; w)$ between two regions of z and z' in the direction of wrist to fingertip. Table 5-3 presents the measured values for straight-line distance d, mean and standard deviation values of PTT and estimated values of PWV between two regions. For all of the 14 feet in each waveform shown in Figure 5-10, the mean values of PTT between wrist and mid-palm and between mid-palm and fingertip are positive and thus agree with the expected direction of PPW propagation in palmar artery. The standard deviation values of PPT, however, are comparable to the mean values which indicates large fluctuations in accurate timing of the feet in PPW waveforms. The fluctuations can be reduced by improvement of time resolution from 4 ms in this study to smaller values with faster camera and adoption of improved peak searching algorithms. Finally, we note that PWV estimated from the data of PPG waveforms in Figure 5-10 are in the same range as those in human coronary artery measured invasively by intra artery line with piezoelectric transducers [154].

CHAPTER 6 DISCUSSION AND SUMMARY

6.1 Discussion

The iPPG method provides a non-contact approach to acquire vital sign data for health monitoring which has the advantages of high spatial-temporal resolution, rapid data acquisition, safety of radiation free and cost-effectiveness. It has attracted intense efforts of research and development for the potentials of wide applications in both clinical and nonclinical scenarios. The quantitative analysis of and extraction of effective biomarker from the iPPG data, however, require optimization of imaging configuration, data processing and accurate modeling of blood flow and light-tissue interaction. The research performed through this dissertation project combines an 1D blood flow model of radial artery and an iMC model for analysis of the *in vivo* iPPG data acquired from hands of two volunteers. To validate the 1D blood flow model, we have simulated the common artery with the parameters given in Table 4-1, and present the temporal profile or waveforms of blood pressure, blood flow velocity, artery cross-section area at the inlet or outlet during 8 cardiac cycles as shown in Figure 4-2. We have also obtained these waveforms in one cardiac cycle with different values of artery length L and Young's modulus E. These simulation results prepared a ground to quantitatively correlate the waveforms of different characteristic parameters of blood flow and pressure waves with the mechanical and morphological parameters used in the fluidic dynamic model. For example, the waveform of blood pressure at the outlet of radial artery under different boundaries conditions in Figure 4-11 show that the temporal variation of blood pressure depend sensitively on the Windkessel parameters quantifying the reflection of pressure waves by the mechanical properties of down-stream artery. The entire pressure profile increases the same time with R_t increased, and the pressure difference given by P_s-P_d decreases with increased C or the decreased ratio of R_1/R_2. It is also interesting to note that the pressure at the dicrotic notch has a peak for $E=9x10^6$ dyne/cm^2 as the elastic modulus of the artery wall, which can be seen in Figure 4-12. Very importantly, we have developed an effective method to estimate PWV by calculating the time difference of P_d between the locations at middle point and outlet of radial artery after employment of a filter in the frequency domain on the simulated data. This allows us to determine that PWV is approximately linear relative to the Young's modulus of artery wall as shown in Figure 4-13.

In addition to the modeling of fluid dynamic model of blood flow, we have developed a voxel-based iMC code to model the light-tissue interaction by incorporation of blood vessels into a multilayer skin tissue phantom, which enables quantitative analysis of iPPG data in terms of artery parameters based on the blood flow model. To speed up iMC simulations, we applied high performance computation method by parallel execution of the iMC code on a GPU board. The results in Figure 4-17 shows that the validation results of iMC simulation against the widely accepted results of RT theory by van de Hulst. The result in Figure 4-19 shows that, the pixel values of a reflection image appear sensitive to the artery radius value that is almost doubled. But during cardiac cycles, the radius variation of artery radius is only about 10% according to our blood flow simulation results presented. To compare the simulation results with measured iPPG data, we configure the skin phantom as a cubic of three layers of epidermis, dermis and subcutis with radial artery embedded in the dermis and subcutis. Two groups of the radius of radial artery simulated by blood flow model under the 'soft' and normal wall conditions are introduced to the iMC simulations. As shown in Figure 4-20, the filtered reflection image intensity under the normal artery case which calculated by a bandpass filter processing the same as that applied in our experimental study, agrees well with the radius profile thus agrees well with the pressure waveform because of the linear wall elastic conditions. But for the ‘soft’ artery case shown in Figure 4-21, the agreement between the simulation iPPG signal and pressure waveform becomes more skewed due to the presence of multiple peaks in the time domain which reduces the effectiveness of bandpass filtering.

Multiple software components of image acquisition and numerical simulation have been developed through this dissertation research to improve an experimental system to study the iPPG technology by rapidly acquiring, processing and simulating the reflected image data from subjects illuminated by multi-wavelength band LED sets. The frame rate of image acquisition and saving is from 100 image pair per second to 250 image pairs per second by applying a multi-threading mechanism and image channel selected in the camera control software built in MFC framework. The algorithm of vital signs extraction of iPPG stack is investigate by a Matlab code. The source code of blood flow model is written in Python, the sound card ECG code is written in C#. and iMC code in CUDA.

The potential of iPPG to determine the spatiotemporal distributions of PPW attracts active efforts to translate the device into a cost-effective tool for measurement of vital sign data and blood vessel conditions. But the complex light-tissue interaction underlying iPPG signals requires innovative algorithms to extract the weak PPG signals with high spatiotemporal resolutions and quantify their relations to PPW in artery with optimized wavelength choice. The time plot of the average pixel intensity of hand in Figure 5-5 A shows clearly that the PPG signal related to PPW is smaller than the mean pixel intensity by three orders of magnitude. Through this study we have developed a novel and robust algorithm of pICA to retrieve spatially resolved PPG signals from monochromatic iPPG stacks with significantly improved SNRs. Quantitative PWI maps by r_{cf} in 12 wavelength bands enabled analysis of PPG waveforms by S_{cf} at multiple

POI sites for examination of artery tree and cardiac activities. The *in vivo* data acquired from two volunteers suggest that the new method outperforms existing ones for monitoring superficial artery in both qualitative visualization and quantitative evaluation. More importantly, the relatively short imaging time of 10 s for an iPPG stack makes it very tolerable to measure vital sign data quickly and accurately from a subject without tissue contact in non-clinical settings.

The phase relations of PPG waveforms are difficult to interpret since they are influenced by both PPW in artery and tissue morphology modulated by PPW. PPW perturbs not only the morphology of the tissue-artery boundary but also the orientation of the skin surface in regions with large and superficial artery. By accurate determination of S_{cf} at multiple POI site in hand, as shown from Figure 5-8 to Figure 5-10 in different wavelength bands, we have qualitatively proved that the strong surface vibration by PPW in the wrist region is likely the cause for the OOP relations in PPG waveforms of certain POI sites. These results are critical for making the skin vibration as the cause of phase variation of PPG waveforms among neighboring POI sites as shown in Figure 5-10. Only with this insight, it became possible to identify the same PPG peaks or “feet” among POI sites in different hand regions per cardiac cycle to correctly determine the mean PPT and estimate PWV as given in Table 5-3. With a camera of higher frame rate, the fluctuations in timing the feet of PPG waveforms can be reduced and spatial resolution of PWV can be improved significantly. These improvements combined with the pICA algorithm introduced here may enable the application of iPPG to extract biomarkers for quantifying wall stiffness and other conditions of superficial artery in additional to acquisition of vital sign data.

6.2 Summary

In summary, we have built an 1D artery model to simulate the blood flow during cardiac cycles. With considered boundary conditions, we obtained the blood pressure profile, the radius of artery wall, and thus calculated PWV. The results show that the PWV is linear relationship with E in the linear elastic wall condition. In future, a 3D model of blood flow will be built to obtain more sensitive results.

A voxelated iMC model has been introduced to quantitative analysis of the iPPG technique. The results of simulation iPPG waveform agrees well with the artery radius and pressure profile in a cardiac cycle. In the following study, we will introduce elastic deformation of skin tissue with artery pulsation to improve the accuracy of simulation and improve the computation speed by optimizing CUDA algorithms to track more photons to reduce the MC fluctuations.

We have shown a platform method of iPPG to retrieve PPG signals related to PPW in superficial artery tree with multispectral capacity from an image stack acquired within 10 s. With a novel and robust pICA algorithm, SNRs of the cardiac signals can be increased by a factor of 4 to achieve high spatiotemporal resolutions, which allows analysis of PPW propagation among multiple sites by PPG waveforms, calculation of PPT and estimation of PWV. With the coming age of rapid camera improvement and artificial intelligence, we expect that the new improvement for the presented method based on quantitative tissue optics modeling will enable non-contact and fast acquisition of iPPG data followed by retrieval of effective PPW related biomarkers to assess cardiovascular conditions for quality and cost-effective healthcare.

REFERENCES

1. Hertzman, A.B., *The blood supply of various skin areas as estimated by the photoelectric plethysmograph.* American Journal of Physiology-Legacy Content, 1938. **124**(2): p. 328-340.

2. Loukogeorgakis, S., et al., *Validation of a device to measure arterial pulse wave velocity by a photoplethysmographic method.* Physiological measurement, 2002. **23**(3): p. 581.

3. Yoon, Y., J.H. Cho, and G. Yoon, *Non-constrained blood pressure monitoring using ECG and PPG for personal healthcare.* Journal of medical systems, 2009. **33**(4): p. 261-266.

4. Mouradian, V., A. Poghosyan, and L. Hovhannisyan. *Continuous wearable health monitoring using novel PPG optical sensor and device*. in *2014 IEEE 10th International Conference on Wireless and Mobile Computing, Networking and Communications (WiMob)*. 2014. IEEE.

5. Vandecasteele, K., et al., *Automated epileptic seizure detection based on wearable ECG and PPG in a hospital environment.* Sensors, 2017. **17**(10): p. 2338.

6. Liu, W., et al., *Reliability analysis of an integrated device of ECG, PPG and pressure pulse wave for cardiovascular disease.* Microelectronics Reliability, 2018. **87**: p. 183-187.

7. Mendelson, Y. and B.D. Ochs, *Noninvasive pulse oximetry utilizing skin reflectance photoplethysmography.* IEEE Transactions on Biomedical Engineering, 1988. **35**(10): p. 798-805.

8. Kamal, A., et al., *Skin photoplethysmography—a review.* Computer methods and programs in biomedicine, 1989. **28**(4): p. 257-269.

9. Al-Naji, A., et al., *Monitoring of cardiorespiratory signal: Principles of remote measurements and review of methods.* IEEE Access, 2017. **5**: p. 15776-15790.

10. Virani, S.S., et al., *Heart disease and stroke statistics—2020 update: a report from the American Heart Association.* Circulation, 2020. **141**(9): p. e139-e596.

11. Carter, A.M., et al., *Association of the platelet PlA polymorphism of glycoprotein IIb/IIIa and the fibrinogen Bβ 448 polymorphism with myocardial infarction and extent of coronary artery disease.* Circulation, 1997. **96**(5): p. 1424-1431.

12. Krushkal, J., et al., *Genome-wide linkage analyses of systolic blood pressure using highly discordant siblings.* Circulation, 1999. **99**(11): p. 1407-1410.

13. Bray, M.S., et al., *Positional genomic analysis identifies the β2-adrenergic receptor gene as a susceptibility locus for human hypertension.* Circulation, 2000. **101**(25): p. 2877-2882.

14. Met, R., et al., *Diagnostic performance of computed tomography angiography in peripheral arterial disease: a systematic review and meta-analysis.* Jama, 2009. **301**(4): p. 415-424.

15. Thomsen, H. and S. Morcos, *Contrast media and the kidney: European Society of Urogenital Radiology (ESUR) guidelines.* The British journal of radiology, 2003. **76**(908): p. 513-518.

16. Brenner, D.J. and E.J. Hall, *Computed tomography—an increasing source of radiation exposure.* New England journal of medicine, 2007. **357**(22): p. 2277-2284.

17. Baum, R.A., et al., *Multicenter trial to evaluate vascular magnetic resonance angiography of the lower extremity.* Jama, 1995. **274**(11): p. 875-880.

18. Meissner, O.A., et al., *Critical limb ischemia: hybrid MR angiography compared with DSA.* Radiology, 2005. **235**(1): p. 308-318.

19. Cronenwett, J.L. and K.W. Johnston, *Rutherford's vascular surgery e-book.* 2014: Elsevier Health Sciences.

20. Petrović, V.L., et al., *High-accuracy real-time monitoring of heart rate variability using 24 GHz continuous-wave Doppler radar.* IEEE Access, 2019. **7**: p. 74721-74733.

21. Currie, P.J., et al., *Continuous wave Doppler determination of right ventricular pressure: a simultaneous Doppler-catheterization study in 127 patients.* Journal of the American College of Cardiology, 1985. **6**(4): p. 750-756.

22. Harris, R.A., et al., *Ultrasound assessment of flow-mediated dilation.* Hypertension, 2010. **55**(5): p. 1075-1085.

23. Axtell, A.L., F.A. Gomari, and J.P. Cooke, *Assessing endothelial vasodilator function with the Endo-PAT 2000.* Journal of visualized experiments: JoVE, 2010(44).

24. Rosfors, S., et al., *Duplex ultrasound in patients with suspected aorto-iliac occlusive disease.* European journal of vascular surgery, 1993. **7**(5): p. 513-517.

25. Garcia, R. and N. Labropoulos, *Duplex ultrasound for the diagnosis of acute and chronic venous diseases.* Surgical Clinics, 2018. **98**(2): p. 201-218.

26. Chin, J.A., E.C. Wang, and M.R. Kibbe, *Evaluation of hyperspectral technology for assessing the presence and severity of peripheral artery disease.* Journal of vascular surgery, 2011. **54**(6): p. 1679-1688.

27. Lai, M., et al. *Evaluation of a non-contact Photo-Plethysmographic Imaging (iPPG) system for peripheral arterial disease assessment*. in *Medical Imaging 2021: Biomedical Applications in Molecular, Structural, and Functional Imaging*. 2021. International Society for Optics and Photonics.

28. London, G., et al., *Volume-dependent parameters in essential hypertension.* Kidney international, 1977. **11**(3): p. 204-208.

29. Caro, C.G., et al., *The mechanics of the circulation*. 2012: Cambridge University Press.

30. Vlachopoulos, C., M. O'Rourke, and W.W. Nichols, *McDonald's blood flow in arteries: theoretical, experimental and clinical principles*. 2011: CRC press.

31. Safar, M.E., B.I. Levy, and H. Struijker-Boudier, *Current perspectives on arterial stiffness and pulse pressure in hypertension and cardiovascular diseases.* Circulation, 2003. **107**(22): p. 2864-2869.

32. Blacher, J., et al., *Pulse pressure not mean pressure determines cardiovascular risk in older hypertensive patients.* Archives of internal medicine, 2000. **160**(8): p. 1085-1089.

33. Benetos, A., et al., *Arterial alterations with aging and high blood pressure. A noninvasive study of carotid and femoral arteries.* Arteriosclerosis and thrombosis: a journal of vascular biology, 1993. **13**(1): p. 90-97.

34. Safar, M.E., X. Girerd, and S. Laurent, *Structural changes of large conduit arteries in hypertension.* Journal of hypertension, 1996. **14**(5): p. 545-555.

35. Collaboration, R.V.f.A.S., *Determinants of pulse wave velocity in healthy people and in the presence of cardiovascular risk factors:'establishing normal and reference values'.* European heart journal, 2010. **31**(19): p. 2338-2350.

36. Hertzman, A.B. and J.B. Dillon, *Applications of photoelectric plethysmography in peripheral vascular disease.* American Heart Journal, 1940. **20**(6): p. 750-761.

37. Allen, J., *Photoplethysmography and its application in clinical physiological measurement.* Physiological measurement, 2007. **28**(3): p. R1.

38. Asada, H.H., et al., *Mobile monitoring with wearable photoplethysmographic biosensors.* IEEE engineering in medicine and biology magazine, 2003. **22**(3): p. 28-40.

39. Tamura, T., et al., *Wearable photoplethysmographic sensors—past and present.* Electronics, 2014. **3**(2): p. 282-302.

40. Shi, P., et al. *Development of a remote photoplethysmographic technique for human biometrics*. in *Design and Quality for Biomedical Technologies II*. 2009. International Society for Optics and Photonics.

41. Cennini, G., et al., *Heart rate monitoring via remote photoplethysmography with motion artifacts reduction.* Optics express, 2010. **18**(5): p. 4867-4875.

42. Shao, D., et al., *Noncontact monitoring of blood oxygen saturation using camera and dual-wavelength imaging system.* IEEE Transactions on Biomedical Engineering, 2015. **63**(6): p. 1091-1098.

43. Kumar, M., A. Veeraraghavan, and A. Sabharwal, *DistancePPG: Robust non-contact vital signs monitoring using a camera.* Biomedical optics express, 2015. **6**(5): p. 1565-1588.

44. Davila, M.I., G.F. Lewis, and S.W. Porges, *The Physiocam: a novel non-contact sensor to Measure heart rate Variability in clinical and Field applications.* Frontiers in public health, 2017. **5**: p. 300.

45. Patil, O.R., et al. *A non-contact PPG biometric system based on deep neural network*. in *2018 IEEE 9th International Conference on Biometrics Theory, Applications and Systems (BTAS)*. 2018. IEEE.

46. Zhan, Q., W. Wang, and G. de Haan, *Analysis of CNN-based remote-PPG to understand limitations and sensitivities.* Biomedical optics express, 2020. **11**(3): p. 1268-1283.

47. Ovalle, W.K. and P.C. Nahirney, *Netter's Essential Histology E-Book: With Correlated Histopathology*. 2020: Elsevier Health Sciences.

48. Prahl, S.A., M.J. van Gemert, and A.J. Welch, *Determining the optical properties of turbid media by using the adding–doubling method.* Applied optics, 1993. **32**(4): p. 559-568.

49. Wang, G., M. Atef, and Y. Lian, *Towards a continuous non-invasive cuffless blood pressure monitoring system using PPG: Systems and circuits review.* IEEE Circuits and systems magazine, 2018. **18**(3): p. 6-26.

50. Ma, X., et al., *Bulk optical parameters of porcine skin dermis at eight wavelengths from 325 to 1557 nm.* Optics letters, 2005. **30**(4): p. 412-414.

51. Bosschaart, N., et al., *A literature review and novel theoretical approach on the optical properties of whole blood.* Lasers in medical science, 2014. **29**(2): p. 453-479.

52. Van Kampen, E. and W.G. Zijlstra, *Determination of hemoglobin and its derivatives.* Advances in clinical chemistry, 1966. **8**: p. 141-187.

53. Maeda, Y., et al. *Comparison of reflected green light and infrared photoplethysmography*. in *2008 30th Annual International Conference of the IEEE Engineering in Medicine and Biology Society*. 2008. IEEE.

54. Lee, J., et al. *Comparison between red, green and blue light reflection photoplethysmography for heart rate monitoring during motion*. in *2013 35th annual international conference of the IEEE engineering in medicine and biology society (EMBC)*. 2013. IEEE.

55. Shvartsman, L.D. and I. Fine, *Optical transmission of blood: effect of erythrocyte aggregation.* IEEE transactions on biomedical engineering, 2003. **50**(8): p. 1026-1033.

56. Blazek, V., W. Rutten, and O. Such, *A method for space-resolved, non-contacting and functional visualization of dermal perfusion (germ.).* German patent, 1996(P196): p. 38.

57. Wu, T., V. Blazek, and H.J. Schmitt. *Photoplethysmography imaging: a new noninvasive and noncontact method for mapping of the dermal perfusion changes*. in *Optical Techniques and Instrumentation for the Measurement of Blood Composition, Structure, and Dynamics*. 2000. International Society for Optics and Photonics.

58. Sun, Y. and N. Thakor, *Photoplethysmography revisited: from contact to noncontact, from point to imaging.* IEEE transactions on biomedical engineering, 2015. **63**(3): p. 463-477.

59. Sokout, M., S. Heidary, and B. Beigzadeh, *Heart Rate Measurement with Imaging Photoplethysmography Signals Using Smart Phone.* Modares Mechanical Engineering, 2019. **19**(7): p. 1751-1757.

60. Khanam, F.-T.-Z., A. Al-Naji, and J. Chahl, *Remote monitoring of vital signs in diverse non-clinical and clinical scenarios using computer vision systems: A review.* Applied Sciences, 2019. **9**(20): p. 4474.

61. Viola, P. and M. Jones. *Rapid object detection using a boosted cascade of simple features*. in *Proceedings of the 2001 IEEE computer society conference on computer vision and pattern recognition. CVPR 2001*. 2001. Ieee.

62. Feng, L., et al., *Motion-resistant remote imaging photoplethysmography based on the optical properties of skin.* IEEE Transactions on Circuits and Systems for Video Technology, 2014. **25**(5): p. 879-891.

63. Wang, W., S. Stuijk, and G. De Haan, *Exploiting spatial redundancy of image sensor for motion robust rPPG.* IEEE transactions on Biomedical Engineering, 2014. **62**(2): p. 415-425.

64. Poh, M.-Z., D.J. McDuff, and R.W. Picard, *Non-contact, automated cardiac pulse measurements using video imaging and blind source separation.* Optics express, 2010. **18**(10): p. 10762-10774.

65. Lewandowska, M., et al. *Measuring pulse rate with a webcam—a non-contact method for evaluating cardiac activity*. in *2011 federated conference on computer science and information systems (FedCSIS)*. 2011. IEEE.

66. Hsu, Y., Y.-L. Lin, and W. Hsu. *Learning-based heart rate detection from remote photoplethysmography features*. in *2014 IEEE International Conference on Acoustics, Speech and Signal Processing (ICASSP)*. 2014. IEEE.

67. McDuff, D., S. Gontarek, and R.W. Picard, *Remote detection of photoplethysmographic systolic and diastolic peaks using a digital camera.* IEEE Transactions on Biomedical Engineering, 2014. **61**(12): p. 2948-2954.

68. Kamshilin, A.A., et al., *Photoplethysmographic imaging of high spatial resolution.* Biomedical optics express, 2011. **2**(4): p. 996-1006.

69. Kamshilin, A.A., et al., *Variability of microcirculation detected by blood pulsation imaging.* PloS one, 2013. **8**(2): p. e57117.

70. Kamshilin, A.A., et al., *A new look at the essence of the imaging photoplethysmography.* Scientific reports, 2015. **5**(1): p. 1-9.

71. Anchan, R., *Estimating pulse wave velocity using mobile phone sensors.* 2011.

72. Shao, D., et al., *Noncontact monitoring breathing pattern, exhalation flow rate and pulse transit time.* IEEE Transactions on Biomedical Engineering, 2014. **61**(11): p. 2760-2767.

73. Huang, S.-C., et al., *A new image blood pressure sensor based on PPG, RRT, BPTT, and harmonic balancing.* IEEE sensors Journal, 2014. **14**(10): p. 3685-3692.

74. Wang, W., S. Stuijk, and G. de Haan, *Living-skin classification via remote-PPG.* IEEE Transactions on biomedical engineering, 2017. **64**(12): p. 2781-2792.

75. Nowara, E.M., A. Sabharwal, and A. Veeraraghavan. *Ppgsecure: Biometric presentation attack detection using photopletysmograms*. in *2017 12th IEEE International Conference on Automatic Face & Gesture Recognition (FG 2017)*. 2017. IEEE.

76. Lakshminarayana, N.N., et al. *A discriminative spatio-temporal mapping of face for liveness detection*. in *2017 IEEE International Conference on Identity, Security and Behavior Analysis (ISBA)*. 2017. IEEE.

77. Thatcher, J.E., et al., *Multispectral and photoplethysmography optical imaging techniques identify important tissue characteristics in an animal model of tangential burn excision.* Journal of Burn Care & Research, 2016. **37**(1): p. 38-52.

78. Kuo, J., et al., *Evaluation of a video-based measure of driver heart rate.* Journal of safety research, 2015. **54**: p. 55. e29-59.

79. Lee, H., J. Lee, and M. Shin, *Using wearable ECG/PPG sensors for driver drowsiness detection based on distinguishable pattern of recurrence plots.* Electronics, 2019. **8**(2): p. 192.

80. Villarroel, M., et al., *Continuous non-contact vital sign monitoring in neonatal intensive care unit.* Healthcare technology letters, 2014. **1**(3): p. 87-91.

81. Rubins, U., A. Miscuks, and M. Lange, *Simple and convenient remote photoplethysmography system for monitoring regional anesthesia effectiveness*, in *EMBEC & NBC 2017*. 2017, Springer. p. 378-381.

82. Chowdhury, M.R., et al., *Deep learning via ECG and PPG signals for prediction of depth of anesthesia.* Biomedical Signal Processing and Control, 2021. **68**: p. 102663.

83. Giannakakis, G., et al., *Stress and anxiety detection using facial cues from videos.* Biomedical Signal Processing and Control, 2017. **31**: p. 89-101.

84. Spicher, N., et al., *Heart rate monitoring in ultra-high-field MRI using frequency information obtained from video signals of the human skin compared to electrocardiography and pulse oximetry.* Current directions in biomedical engineering, 2015. **1**(1): p. 69-72.

85. Murgo, J.P., et al., *Aortic input impedance in normal man: relationship to pressure wave forms.* Circulation, 1980. **62**(1): p. 105-116.

86. Zamir, M. and R. Budwig, *Physics of pulsatile flow.* Appl. Mech. Rev., 2002. **55**(2): p. B35-B35.

87. Boonya-Ananta, T., et al., *Synthetic photoplethysmography (PPG) of the radial artery through parallelized Monte Carlo and its correlation to body mass index (BMI).* Scientific Reports, 2021. **11**(1): p. 1-11.

88. Reinhart, W.H., N.Z. Piety, and S.S. Shevkoplyas, *Influence of red blood cell aggregation on perfusion of an artificial microvascular network.* Microcirculation, 2017. **24**(5): p. e12317.

89. Barnard, A., et al., *A theory of fluid flow in compliant tubes.* Biophysical journal, 1966. **6**(6): p. 717-724.

90. Hughes, T.J. and J. Lubliner, *On the one-dimensional theory of blood flow in the larger vessels.* Mathematical Biosciences, 1973. **18**(1-2): p. 161-170.

91. Alastruey, J., K.H. Parker, and S.J. Sherwin. *Arterial pulse wave haemodynamics*. in *11th International Conference on Pressure Surges*. 2012. Virtual PiE Led t/a BHR Group.

92. Zhang, J., P.C. Johnson, and A.S. Popel, *Red blood cell aggregation and dissociation in shear flows simulated by lattice Boltzmann method.* Journal of biomechanics, 2008. **41**(1): p. 47-55.

93. White, F.M. and J. Majdalani, *Viscous fluid flow*. Vol. 3. 2006: McGraw-Hill New York.

94. Peiró, J. and A. Veneziani, *Reduced models of the cardiovascular system*, in *Cardiovascular mathematics*. 2009, Springer. p. 347-394.

95. Westerhof, N., et al., *Analog studies of the human systemic arterial tree.* Journal of biomechanics, 1969. **2**(2): p. 121-143.

96. Nobile, F. and C. Vergara, *An effective fluid-structure interaction formulation for vascular dynamics by generalized Robin conditions.* SIAM Journal on Scientific Computing, 2008. **30**(2): p. 731-763.

97. Fernández, M.A., et al., *The derivation of the equations for fluids and structure*, in *Cardiovascular mathematics*. 2009, Springer. p. 77-121.

98. Willemet, M. and J. Alastruey, *Arterial pressure and flow wave analysis using time-domain 1-D hemodynamics.* Annals of biomedical engineering, 2015. **43**(1): p. 190-206.

99. Mynard, J.P. and J.J. Smolich, *One-dimensional haemodynamic modeling and wave dynamics in the entire adult circulation.* Annals of biomedical engineering, 2015. **43**(6): p. 1443-1460.

100. Mynard, J. and P. Nithiarasu, *A 1D arterial blood flow model incorporating ventricular pressure, aortic valve and regional coronary flow using the locally conservative Galerkin (LCG) method.* Communications in numerical methods in engineering, 2008. **24**(5): p. 367-417.

101. Mynard, J., et al., *A numerical model of neonatal pulmonary atresia with intact ventricular septum and RV-dependent coronary flow.* International Journal for Numerical Methods in Biomedical Engineering, 2010. **26**(7): p. 843-861.

102. Xiao, N., J. Alastruey, and C. Alberto Figueroa, *A systematic comparison between 1-D and 3-D hemodynamics in compliant arterial models.* International journal for numerical methods in biomedical engineering, 2014. **30**(2): p. 204-231.

103. Liu, Y., et al., *Optical markers in duodenal mucosa predict the presence of pancreatic cancer.* Clinical Cancer Research, 2007. **13**(15): p. 4392-4399.

104. Ishimaru, A., *Wave propagation and scattering in random media*. Vol. 2. 1978: Academic press New York.

105. Mishchenko, M.I., L.D. Travis, and A.A. Lacis, *Multiple scattering of light by particles: radiative transfer and coherent backscattering*. 2006: Cambridge University Press.

106. Tseng, S.H. and B. Huang, *Comparing Monte Carlo simulation and pseudospectral time-domain numerical solutions of Maxwell's equations of light scattering by a macroscopic random medium.* Applied Physics Letters, 2007. **91**(5): p. 051114.

107. Voit, F., J. Schäfer, and A. Kienle, *Light scattering by multiple spheres: comparison between Maxwell theory and radiative-transfer-theory calculations.* Optics letters, 2009. **34**(17): p. 2593-2595.

108. Voit, F., et al., *Multiple scattering of polarized light: comparison of Maxwell theory and radiative transfer theory.* Journal of biomedical optics, 2012. **17**(4): p. 045003.

109. Schäfer, J. and A. Kienle, *Scattering of light by multiple dielectric cylinders: comparison of radiative transfer and Maxwell theory.* Optics letters, 2008. **33**(20): p. 2413-2415.

110. Van de Hulst, H.C., *Multiple light scattering: tables, formulas, and applications*. 2012: Elsevier.

111. Jacques, S.L., C. Alter, and S.A. Prahl, *Angular dependence of HeNe laser light scattering by human dermis.* Lasers Life Sci, 1987. **1**(4): p. 309-333.

112. Born, M. and E. Wolf, *Principles of optics: electromagnetic theory of propagation, interference and diffraction of light*. 2013: Elsevier.

113. Ding, H., et al., *Determination of refractive indices of porcine skin tissues and intralipid at eight wavelengths between 325 and 1557 nm.* JOSA A, 2005. **22**(6): p. 1151-1157.

114. Chen, C., et al., *A primary method for determination of optical parameters of turbid samples and application to intralipid between 550 and 1630nm.* Optics Express, 2006. **14**(16): p. 7420-7435.

115. Qin, J. and R. Lu, *Hyperspectral diffuse reflectance imaging for rapid, noncontact measurement of the optical properties of turbid materials.* Applied optics, 2006. **45**(32): p. 8366-8373.

116. Tian, P., et al., *Quantitative characterization of turbidity by radiative transfer based reflectance imaging.* Biomedical optics express, 2018. **9**(5): p. 2081-2094.

117. Chen, X., et al., *Fast method for inverse determination of optical parameters from two measured signals.* Optics letters, 2013. **38**(12): p. 2095-2097.

118. Aernouts, B., et al., *Supercontinuum laser based optical characterization of Intralipid® phantoms in the 500-2250 nm range.* Optics express, 2013. **21**(26): p. 32450-32467.

119. Liang, X., et al., *Spectrophotometric determination of turbid optical parameters without using an integrating sphere.* Applied Optics, 2016. **55**(8): p. 2079-2085.

120. Wang, L., S.L. Jacques, and L. Zheng, *MCML—Monte Carlo modeling of light transport in multi-layered tissues.* Computer methods and programs in biomedicine, 1995. **47**(2): p. 131-146.

121. Tian, P., et al., *Spectral determination of μa, μs and g from single and multiple scattering signals with one optically thick sample.* Journal of Quantitative Spectroscopy and Radiative Transfer, 2020. **245**: p. 106868.

122. Amanatides, J. and A. Woo. *A fast voxel traversal algorithm for ray tracing*. in *Eurographics*. 1987.

123. Wieringa, F.P., F. Mastik, and A.F. van der Steen, *Contactless multiple wavelength photoplethysmographic imaging: A first step toward "SpO 2 camera" technology.* Annals of biomedical engineering, 2005. **33**(8): p. 1034-1041.

124. Verkruysse, W., L.O. Svaasand, and J.S. Nelson, *Remote plethysmographic imaging using ambient light.* Optics express, 2008. **16**(26): p. 21434-21445.

125. De Haan, G. and V. Jeanne, *Robust pulse rate from chrominance-based rPPG.* IEEE Transactions on Biomedical Engineering, 2013. **60**(10): p. 2878-2886.

126. Mannapperuma, K., et al., *Performance limits of ICA-based heart rate identification techniques in imaging photoplethysmography.* Physiological measurement, 2014. **36**(1): p. 67.

127. Amelard, R., D.A. Clausi, and A. Wong, *Spatial probabilistic pulsatility model for enhancing photoplethysmographic imaging systems.* Journal of biomedical optics, 2016. **21**(11): p. 116010.

128. Marcinkevics, Z., et al., *Imaging photoplethysmography for clinical assessment of cutaneous microcirculation at two different depths.* Journal of biomedical optics, 2016. **21**(3): p. 035005.

129. Moço, A.V., S. Stuijk, and G. de Haan, *Skin inhomogeneity as a source of error in remote PPG-imaging.* Biomedical optics express, 2016. **7**(11): p. 4718-4733.

130. Wang, W., A.C. den Brinker, and G. De Haan, *Discriminative signatures for remote-PPG.* IEEE Transactions on Biomedical Engineering, 2019. **67**(5): p. 1462-1473.

131. Goudarzi, R.H., S.S. Mousavi, and M. Charmi. *Using imaging Photoplethysmography (iPPG) Signal for Blood Pressure Estimation*. in *2020 International Conference on Machine Vision and Image Processing (MVIP)*. 2020. IEEE.

132. Djeldjli, D., et al., *Remote estimation of pulse wave features related to arterial stiffness and blood pressure using a camera.* Biomedical Signal Processing and Control, 2021. **64**: p. 102242.

133. Cardoso, J.-F., *Blind signal separation: statistical principles.* Proceedings of the IEEE, 1998. **86**(10): p. 2009-2025.

134. Rutledge, D.N. and D.J.-R. Bouveresse, *Independent components analysis with the JADE algorithm.* TrAC Trends in Analytical Chemistry, 2013. **50**: p. 22-32.

135. Updegrove, A., et al., *SimVascular: an open source pipeline for cardiovascular simulation.* Annals of biomedical engineering, 2017. **45**(3): p. 525-541.

136. Panel, M., *ROM Simulation Tool.*

137. Boileau, E., et al., *A benchmark study of numerical schemes for one -dimensional arterial blood flow modelling.* International journal for numerical methods in biomedical engineering, 2015. **31**(10): p. e02732.

138. Reymond, P., et al., *Validation of a one-dimensional model of the systemic arterial tree.* American Journal of Physiology-Heart and Circulatory Physiology, 2009. **297**(1): p. H208-H222.

139. Safar, M.E., *Arterial stiffness as a risk factor for clinical hypertension.* Nature Reviews Cardiology, 2018. **15**(2): p. 97-105.

140. Periyasamy, V. and M. Pramanik, *Advances in Monte Carlo simulation for light propagation in tissue.* IEEE reviews in biomedical engineering, 2017. **10**: p. 122-135.

141. Avolio, A.P., et al., *Arterial flow, pulse pressure and pulse wave velocity in men and women at various ages.* Sex-Specific Analysis of Cardiovascular Function, 2018: p. 153-168.

142. Guide, D., *CUDA C++ Programming Guide.* NVIDIA, April, 2021.

143. Ren, N., et al., *GPU-based Monte Carlo simulation for light propagation in complex heterogeneous tissues.* Optics express, 2010. **18**(7): p. 6811-6823.

144. Van de Hulst, H.C., *Multiple light scattering: tables, formulas, and applications*. Vol. Vol. 1 & 2. 1980: Academic Press, New York, 1980.

145. Marchesini, R., et al., *Optical properties of in vitro epidermis and their possible relationship with optical properties of in vivo skin.* Journal of Photochemistry and Photobiology B: Biology, 1992. **16**(2): p. 127-140.

146. Salomatina, E.V., et al., *Optical properties of normal and cancerous human skin in the visible and near-infrared spectral range.* Journal of biomedical optics, 2006. **11**(6): p. 064026.

147. Ding, H., et al., *Refractive indices of human skin tissues at eight wavelengths and estimated dispersion relations between 300 and 1600 nm.* Physics in Medicine & Biology, 2006. **51**(6): p. 1479.

148. Simpson, C.R., et al., *Near-infrared optical properties of ex vivo human skin and subcutaneous tissues measured using the Monte Carlo inversion technique.* Physics in Medicine & Biology, 1998. **43**(9): p. 2465.

149. Bashkatov, A., et al., *Optical properties of human skin, subcutaneous and mucous tissues in the wavelength range from 400 to 2000 nm.* Journal of Physics D: Applied Physics, 2005. **38**(15): p. 2543.

150. Lorbeer, R., et al., *Reference values of vessel diameters, stenosis prevalence, and arterial variations of the lower limb arteries in a male population sample using contrast-enhanced MR angiography.* PloS one, 2018. **13**(6): p. e0197559.

151. Kim, Y.O., et al., *The impact of intima-media thickness of radial artery on early failure of radiocephalic arteriovenous fistula in hemodialysis patients.* Journal of Korean medical science, 2006. **21**(2): p. 284-289.

152. Van Alste, J.A. and T. Schilder, *Removal of base-line wander and power-line interference from the ECG by an efficient FIR filter with a reduced number of taps.* IEEE transactions on biomedical engineering, 1985(12): p. 1052-1060.

153. Brzezinski, M., T. Luisetti, and M.J. London, *Radial artery cannulation: a comprehensive review of recent anatomic and physiologic investigations.* Anesthesia & Analgesia, 2009. **109**(6): p. 1763-1781.

154. Davies, J.E., et al., *Use of simultaneous pressure and velocity measurements to estimate arterial wave speed at a single site in humans.* American Journal of Physiology-Heart and Circulatory Physiology, 2006. **290**(2): p. H878-H885.

155. Elgendi, M., *On the analysis of fingertip photoplethysmogram signals.* Current cardiology reviews, 2012. **8**(1): p. 14-25.

APPENDIX A ICA-JADE ALGORITHM SUMMARY

Description of ICA

Given a set of K observed signal vectors of $X = (x_1, ..., x_n)^T$ and a set of K source signal vectors of $S = (s_1, ..., s_n)^T$, each of them having n elements, the algorithm of independent component analysis (ICA) is to find a matrix B as a separating matrix to map linearly between the two sets of vectors by $S = BX$, to transform observed vectors of $\mathbf{X}_k$ into source signals $\mathbf{S}_k$' as statistically independent as possible. The key issues of ICA are the definition of criteria to measure independence among the output or source vectors and the efficient iterating algorithm to find a separating matrix B that satisfies the criteria. The ability of an ICA algorithm to perform satisfactory separation of mixed signals is based on two assumptions. We also note below the three features of the input signals from mixed sources.

Two assumptions are given by

1. The signal sources are statistically independent of each other.
2. Each signal source has a non-Gaussian distribution.

Three features of input signals can be expressed as

1. Independence: Even though the source signals are assumed to be statistically independent; however, the signals from mixture of sources are not required to be so. This is because the signals of mixed sources share the same set of signal sources.
2. Normality: According to the Central Limit Theorem, the distribution of a sum of independent random variables with finite variance tends to approach towards a Gaussian distribution.

3. Complexity: The temporal complexity of any signal mixture is greater than that of its simplest constituent source signal.

Description of JADE

Joint Approximate Diagonalization of Eigenmatrices algorithm (JADE) is an ICA method based on the statistic?? of diagonalization of an order 4 cumulant tensor. Such a cumulant is a four-dimensional array whose entries are given by a linear combination of order 4 cross cumulants of four zero-mean random variables as

$$Cum(x_i, x_j, x_k, x_l) = E\{x_i x_j x_k x_l\} - E\{x_i x_j\}E\{x_k x_l\} - E\{x_i x_k\}E\{x_j x_l\} - E\{x_i x_l\}E\{x_j x_k\} \quad \text{(A-1)}$$

where i, j, k, l=1…n, and E{…} is the expected value of random variable data if the variables are not zero-mean ones.

The sequence of calculations for our MATLAB code of the JADE algorithm can summarized as follows

1. Mean centering

```
[n,T]   = size(X);
X   = X - mean(X')' * ones(1,T);
```

2. Whitening

```
[U,D]     = eig((X*X')/T) ;
[Ds,k]    = sort(diag(D)) ;
PCs       = n:-1:n-m+1    ;
B         = U(:,k(PCs))'    ;
scales    = sqrt(Ds(PCs)) ;
B         = diag(1./scales)*B  ;
X         = B*X;
```

3. Form staistics

```
X = X';
dimsymm     = (m*(m+1))/2;
nbcm        = dimsymm  ;
CM      = zeros(m,m*nbcm);
R       = eye(m);
Qij         = zeros(m);
Xim     = zeros(m,1);
Xijm        = zeros(m,1);
Uns     = ones(1,m);
Range     = 1:m ;
```

```
for im = 1:m
  Xim = X(:,im) ;
  Xijm= Xim.*Xim ;
  Qij           = ((Xijm(:,Uns).*X)' * X)/T - R - 2 * R(:,im)*R(:,im)' ;
  CM(:,Range)   = Qij ;
  Range         = Range  + m ;
  for jm = 1:im-1
    Xijm        = Xim.*X(:,jm) ;
    Qij         = sqrt(2) *(((Xijm(:,Uns).*X)' * X)/T - R(:,im)*R(:,jm)' -
R(:,jm)*R(:,im)') ;
    CM(:,Range) = Qij ;
    Range       = Range  + m ;
  end ;
end;
```

4. Optimize and orthogonal contrast

```
V   = eye(m) ;
Diag    = zeros(m,1) ;
On      = 0 ;
Range   = 1:m ;
for im = 1:nbcm,
  Diag  = diag(CM(:,Range)) ;
  On    = On + sum(Diag.*Diag) ;
  Range = Range + m ;
end
Off = sum(sum(CM.*CM)) - On ;

seuil   = 1.0e-6 / sqrt(T) ;
encore  = 1;
sweep   = 0;
updates = 0;
upds    = 0;
g   = zeros(2,nbcm);
gg  = zeros(2,2);
G   = zeros(2,2);
c   = 0 ;
s   = 0 ;
ton = 0 ;
toff    = 0 ;
theta   = 0 ;
Gain    = 0 ;

while encore, encore=0;

  sweep = sweep+1;
  upds  = 0 ;
  Vkeep = V ;

  for p=1:m-1,
    for q=p+1:m,

      Ip = p:m:m*nbcm ;
      Iq = q:m:m*nbcm ;


      g     = [ CM(p,Ip)-CM(q,Iq) ; CM(p,Iq)+CM(q,Ip) ];
      gg    = g*g';
      ton   = gg(1,1)-gg(2,2);
      toff  = gg(1,2)+gg(2,1);
      theta = 0.5*atan2( toff , ton+sqrt(ton*ton+toff*toff) );
      Gain  = (sqrt(ton*ton+toff*toff) - ton) / 4 ;


      if abs(theta) > seuil,
    encore  = 1 ;
```

```
    upds    = upds    + 1;
    c   = cos(theta);
    s   = sin(theta);
    G   = [ c -s ; s c ] ;

    pair        = [p;q] ;
    V(:,pair)   = V(:,pair)*G ;
    CM(pair,:)  = G' * CM(pair,:) ;
    CM(:,[Ip Iq])   = [ c*CM(:,Ip)+s*CM(:,Iq) -s*CM(:,Ip)+c*CM(:,Iq) ] ;


    On   = On  + Gain;
    Off  = Off - Gain;

      end
    end
  end
  updates = updates + upds ;
end
```

5. separate

```
B   = V'*B ;
A           = pinv(B) ;
[Ds,keys]   = sort(sum(A.*A)) ;
B           = B(keys,:)        ;
B           = B(m:-1:1,:)      ;
b   = B(:,1) ;
signs   = sign(sign(b)+0.1) ;
B   = diag(signs)*B ;
```

APPENDIX B PROTOCOL OF SIMVASCULAR

SimVascular is an open-source software package that can be used to perform blood flow simulation and analysis. The link of the source code is at: https://github.com/SimVascular/SimVascular. It could be used to create the blood vessel geometry, boundary conditions (BCs) and initial conditions for a 1D model of blood flow. The model for the flow of blood as a Newtonian and incompressible fluid in a deforming and elastic 1D artery is used in our study to numerically solve three flow equations under suitable initial and boundary conditions. The three equations are mass conservation equation, linear momentum equation and material relation as presented in Chapter 3.

The user interface of the 1D blood flow model shown in Figure B-1including the structure of the artery networks, the parameters control panel for flow dynamic parameters and simulation parameters. The protocol are lists below.

1. The geometry of the 1D artery networks can be calculated by the centerlines derived from the surface of a 3D geometric model. The geometry of centerlines is used to define nodes, branching points, inlet and out of artery networks. Once the geometry is set, we can directly define the parameter of each node. For each node in the artery network, the element size is used here to discretize an artery segment for modeling.
2. After structure is established, the basic parameters of blood density and viscosity need to be set.
3. Next set the inlet/outlet BCs. The type of inlet BC type is prescribed as velocity and analytic shape of flow or flow rates during a cardiac cycle and total period. The inlet flow rates are provided by an input parameter file with time and flow value columns.

4. The type of outlet BCs is given by an RCR Windekessel model. The outlet initial pressure is set to the distal pressure which affects the speed for a simulation to reach stabilized condition.
5. The material property for artery wall needs to be set to linear.
6. Also set the solver parameters including time step size, number of time steps, number of timesteps between saving data.
7. Create a 1D solver input file and run the 1D solver.

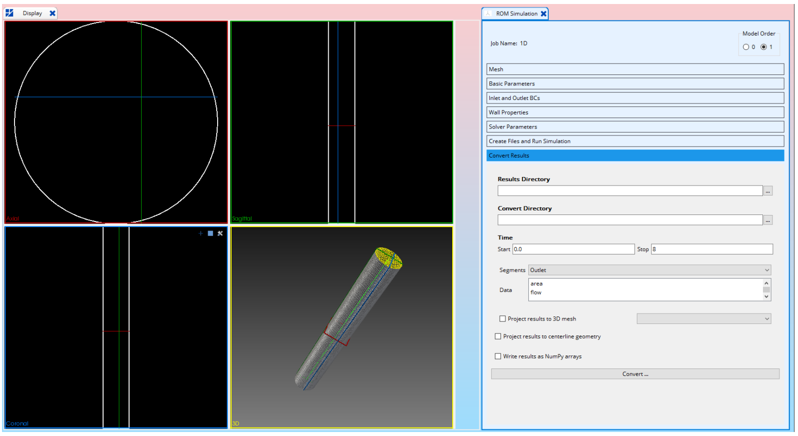

Job Name: 1D

Model Order ○ 0 ● 1

Time

Start 0.0 Stop 8

Segments Outlet

Data area flow

☐ Project results to 3D mesh

☐ Project results to centerline geometry

☐ Write results as NumPy arrays

Figure B-1 User interface for the single artery mode.

APPENDIX C THE CIRCUIT AND CODE OF THE SOUND CARD ECG

We have developed an ECG detection device to obtain the waveform data with a sound card to acquire the ECG signals from an amplifier circuit board. The ECG data acquisition software read the output signals from the board via the microphone input of a computer. The amplifier circuit was built with a dedicated ECG signal conditioning chip (AD8232, Analog Devices, Inc.) to sample signals at a rate of 8 kHz from three ECG electrodes placing on chest of subject. Then the detected signals are transmitted to computer. The software is an open-source code built in C# with the link at https://github.com/swharden/SoundCardECG/tree/7e0f610ec824002428c3f1f8b135ea85ea3cf885#hardware-notes.

The control software has three modules including signal acquisition, processing, and display. To acquire and save the ECG signal, we added a data saving module. The hardware is shown in Figure C-1. The signal processing consists of a low pass filter with the threshold 500 Hz . The digitized data acquired from the sound card are in the form of 16-bit binary numbers and each data at a sampling time with values bigger than 3500 is considered as an ECG signal. The electrodes configuration is illustrated in Figure C-2, the electrode in black is placed on upper-right location of the chest, the one in blue on upper-left of chest and red one on right side of abdomen. Figure C-3 presents a sample of the ECG signals from the volunteer #1 acquired by this program.

Figure C-1 The AD chip and electrodes.

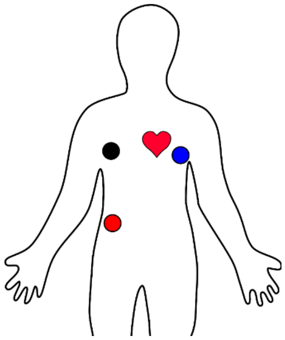

Figure C-2 The configuration of ECG electrodes.

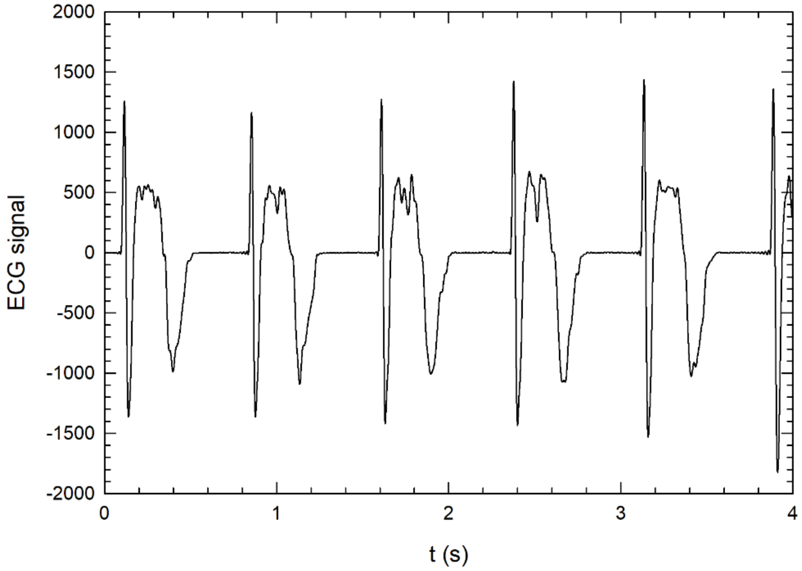

Figure C-3 Waveform of ECG signal acquired from the volunteer #1.